

JPTM

Journal of Pathology
and Translational Medicine

January 2019
Vol. 53 / No.1
jpatholtm.org
pISSN: 2383-7837
eISSN: 2383-7845



*Artificial Intelligence
in Pathology*

Aims & Scope

The *Journal of Pathology and Translational Medicine* is an open venue for the rapid publication of major achievements in various fields of pathology, cytopathology, and biomedical and translational research. The Journal aims to share new insights into the molecular and cellular mechanisms of human diseases and to report major advances in both experimental and clinical medicine, with a particular emphasis on translational research. The investigations of human cells and tissues using high-dimensional biology techniques such as genomics and proteomics will be given a high priority. Articles on stem cell biology are also welcome. The categories of manuscript include original articles, review and perspective articles, case studies, brief case reports, and letters to the editor.

Subscription Information

To subscribe to this journal, please contact the Korean Society of Pathologists/the Korean Society for Cytopathology. Full text PDF files are also available at the official website (<http://jpathol.tml.org>). *Journal of Pathology and Translational Medicine* is indexed by Emerging Sources Citation Index (ESCI), PubMed, PubMed Central, Scopus, KoreaMed, KoMCI, WPRIM, Directory of Open Access Journals (DOAJ), and CrossRef. Circulation number per issue is 700.

Editors-in-Chief

Jung, Chan Kwon, MD (*The Catholic University of Korea, Korea*) <https://orcid.org/0000-0001-6843-3708>

Park, So Yeon, MD (*Seoul National University, Korea*) <https://orcid.org/0000-0002-0299-7268>

Senior Editors

Hong, Soon Won, MD (*Yonsei University, Korea*) <https://orcid.org/0000-0002-0324-2414>

Kim, Chong Jai, MD (*University of Ulsan, Korea*) <http://orcid.org/0000-0002-2844-9446>

Associate Editors

Shin, Eunah, MD (*CHA University, Korea*) <http://orcid.org/0000-0001-5961-3563>

Kim, Haeryoung, MD (*Seoul National University, Korea*) <http://orcid.org/0000-0002-4205-9081>

Editorial Board

Ali, Syed Z. (*Johns Hopkins Hospital, U.S.A.*)

Avila-Casado, Maria del Carmen (*University of Toronto, Toronto General Hospital UHN, Canada*)

Bae, Young Kyung (*Yeungnam University, Korea*)

Bongiovanni, Massimo (*Centre Hospitalier Universitaire Vaudois, Switzerland*)

Cho, Kyung-Ja (*University of Ulsan, Korea*)

Choi, Yeong-Jin (*The Catholic University of Korea, Korea*)

Choi, Yoo Duk (*Chonnam National University, Korea*)

Chong, Yo Sep (*The Catholic University of Korea, Korea*)

Chung, Jin-Haeng (*Seoul National University, Korea*)

Gong, Gyungyub (*University of Ulsan, Korea*)

Fadda, Guido (*Catholic University of the Sacred Heart, Italy*)

Grignon, David J. (*Indiana University, U.S.A.*)

Ha, Seung Yeon (*Gachon University, Korea*)

Han, Jee Young (*Inha University, Korea*)

Jang, Se Jin (*University of Ulsan, Korea*)

Jeong, Jin Sook (*Dong-A University, Korea*)

Jun, Sun-Young (*The Catholic University of Korea, Korea*)

Kang, Gyeong Hoon (*Seoul National University, Korea*)

Katoh, Ryohei (*University of Yamaguchi, Japan*)

Kerr, Keith M. (*Aberdeen University Medical School, U.K.*)

Kim, Aeree (*Korea University, Korea*)

Kim, Jang-Hee (*Ajou University, Korea*)

Kim, Jung Ho (*Seoul National University, Korea*)

Kim, Kyoung Mee (*Sungkyunkwan University, Korea*)

Kim, Kyu Rae (*University of Ulsan, Korea*)

Kim, Se Hoon (*Yonsei University, Korea*)

Kim, Woo Ho (*Seoul National University, Korea*)

Kim, Youn Wha (*Kyung Hee University, Korea*)

Ko, Young Hye (*Sungkyunkwan University, Korea*)

Koo, Ja Seung (*Yonsei University, Korea*)

Lee, C. Soon (*University of Western Sydney, Australia*)

Lee, Hye Seung (*Seoul National University, Korea*)

Lee, Kyung Han (*Sungkyunkwan University, Korea*)

Lee, Sug Hyung (*The Catholic University of Korea, Korea*)

Lkhagvadorj, Sayamaa (*Mongolian National University of Medical Sciences, Mongolia*)

Moon, Woo Sung (*Chonbuk University, Korea*)

Ngo, Quoc Dat (*Ho Chi Minh University of Medicine and Pharmacy, VietNam*)

Paik, Jin Ho (*Seoul National University, Korea*)

Park, Young Nyun (*Yonsei University, Korea*)

Ro, Jae Y. (*Cornell University, The Methodist Hospital, U.S.A.*)

Romero, Roberto (*National Institute of Child Health and Human Development, U.S.A.*)

Schmitt, Fernando (*IPATIMUP [Institute of Molecular Pathology and Immunology of the University of Porto], Portugal*)

Shahid, Pervez (*Aga Khan University, Pakistan*)

Sim, Hyo Sup (*Yonsei University, Korea*)

Song, Joon Seon (*University of Ulsan, Korea*)

Sung, Chang Ohk (*University of Ulsan, Korea*)

Tan, Puay Hoon (*National University of Singapore, Singapore*)

Than, Nandor Gabor (*Semmelweis University, Hungary*)

Tse, Gary M. (*Prince of Wales Hospital, Hongkong*)

Vielh, Philippe (*International Academy of Cytology Gustave Roussy Cancer Campus Grand Paris, France*)

Wildman, Derek (*University of Illinois, U.S.A.*)

Yatabe, Yasushi (*Aichi Cancer Center, Japan*)

Yoon, Bo Hyun (*Seoul National University, Korea*)

Yoon, Sun Och (*Yonsei University, Korea*)

Statistics Editors

Kim, Dong Wook (*National Health Insurance Service Ilsan Hospital, Korea*)

Lee, Hye Sun (*Yonsei University, Korea*)

Manuscript Editor

Chang, Soo-Hee (*InfoLumi Co., Korea*)

Contact the Korean Society of Pathologists/the Korean Society for Cytopathology

Publishers: Lee, Kyo Young, MD, Hong, Soon Won, MD

Editors-in-Chief: Jung, Chan Kwon, MD, Park, So Yeon, MD

Published by the Korean Society of Pathologists/the Korean Society for Cytopathology

Editorial Office

Room 1209 Gwanghwamun Officia, 92 Saemunan-ro, Jongno-gu, Seoul 03186, Korea

Tel: +82-2-795-3094 Fax: +82-2-790-6635 E-mail: office@jpathol.tml.org

#1508 Renaissancetower, 14 Mallijae-ro, Mapo-gu, Seoul 04195, Korea

Tel: +82-2-593-6943 Fax: +82-2-593-6944 E-mail: office@jpathol.tml.org

Printed by iMiS Company Co., Ltd. (JMC)

Jungang Bldg. 18-8 Wonhyo-ro 89-gil, Yongsan-gu, Seoul 04314, Korea

Tel: +82-2-717-5511 Fax: +82-2-717-5515 E-mail: ml@smileml.com

Manuscript Editing by InfoLumi Co.

210-202, 421 Pangyo-ro, Bundang-gu, Seongnam 13522, Korea

Tel: +82-70-8839-8800 E-mail: infolumi.chang@gmail.com

Front cover image: Expression of S100A8 and S100A9 in non-small cell carcinoma of the lung (Fig. 1). p15.

© Copyright 2019 by the Korean Society of Pathologists/the Korean Society for Cytopathology

© Journal of Pathology and Translational Medicine is an Open Access journal under the terms of the Creative Commons Attribution Non-Commercial License (<https://creativecommons.org/licenses/by-nc/4.0>).

© This paper meets the requirements of KS X ISO 9706, ISO 9706-1994 and ANSI/NISO Z.39.48-1992 (Permanence of Paper).

This journal was supported by the Korean Federation of Science and Technology Societies Grant funded by the Korean Government.

CONTENTS

REVIEW

- 1 **Artificial Intelligence in Pathology**
Hye Yoon Chang, Chan Kwon Jung, Junwoo Isaac Woo, Sanghun Lee, Joonyoung Cho, Sun Woo Kim, Tae-Yeong Kwak

ORIGINAL ARTICLES

- 13 **Prognostic Role of S100A8 and S100A9 Protein Expressions in Non-small Cell Carcinoma of the Lung**
Hyun Min Koh, Hye Jung An, Gyung Hyuck Ko, Jeong Hee Lee, Jong Sil Lee, Dong Chul Kim, Jung Wook Yang, Min Hye Kim, Sung Hwan Kim, Kyung Nyeo Jeon, Gyeong-Won Lee, Se Min Jang, Dae Hyun Song
- 23 **PLAG1, SOX10, and Myb Expression in Benign and Malignant Salivary Gland Neoplasms**
Ji Hyun Lee, Hye Ju Kang, Chong Woo Yoo, Weon Seo Park, Junsun Ryu, Yuh-Seog Jung, Sung Weon Choi, Joo Yong Park, Nayoung Han
- 31 **Uterine Malignant Mixed Müllerian Tumors Following Treatment with Selective Estrogen Receptor Modulators in Patients with Breast Cancer: A Report of 13 Cases and Their Clinicopathologic Characteristics**
Byung-Kwan Jeong, Chang Ohk Sung, Kyu-Rae Kim
- 40 **Prognostic Impact of *Fusobacterium nucleatum* Depends on Combined Tumor Location and Microsatellite Instability Status in Stage II/III Colorectal Cancers Treated with Adjuvant Chemotherapy**
Hyeon Jeong Oh, Jung Ho Kim, Jeong Mo Bae, Hyun Jung Kim, Nam-Yun Cho, Gyeong Hoon Kang
- 50 **Quilty Lesions in the Endomyocardial Biopsies after Heart Transplantation**
Haeyon Cho, Jin-Oh Choi, Eun-Seok Jeon, Jung-Sun Kim

CASE REPORTS

- 57 **Primary Peripheral Gamma Delta T-Cell Lymphoma of the Central Nervous System: Report of a Case Involving the Intramedullary Spinal Cord and Presenting with Myelopathy**
Jeemin Yim, Seung Geun Song, Sehui Kim, Jae Won Choi, Kyu-Chong Lee, Jeong Mo Bae, Yoon Kyung Jeon

62 TFE3-Expressing Perivascular Epithelioid Cell Tumor of the Breast

Hyunjin Kim, Jimin Kim, Se Kyung Lee, Eun Yoon Cho, Soo Youn Cho

66 Rare Manifestations of Churg-Strauss Syndrome with Mediastinal and Hilar Lymphadenopathies: Report of an Autopsy Case

Woo Cheal Cho, Bharat Ramlal, Mary Fiel-Gan, Xianyuan Song

70 Cytopathologic Features of Secretory Carcinoma of Salivary Gland: Report of Two Cases

Young Ah Kim, Jae Won Joung, Sun-Jae Lee, Hoon-Kyu Oh, Chang Ho Cho, Woo Jung Sung

Instructions for Authors for *Journal of Pathology and Translational Medicine* are available at <http://jpatholm.org/authors/authors.php>

Artificial Intelligence in Pathology

Hye Yoon Chang · Chan Kwon Jung¹
Junwoo Isaac Woo · Sanghun Lee
Joonyoung Cho · Sun Woo Kim
Tae-Yeong Kwak

Deep Bio Inc., Seoul; ¹Department of Hospital Pathology, College of Medicine, The Catholic University of Korea, Seoul, Korea

Received: December 13, 2018
Accepted: December 16, 2018

Corresponding Author

Tae-Yeong Kwak, PhD
Deep Bio Inc., 1201 Hanwha Bizmetro, 242
Digital-ro, Guro-gu, Seoul 08394, Korea
Tel: +82-70-7703-4746
Fax: +82-2-2621-2223
E-mail: tykwak@deepbio.co.kr

As in other domains, artificial intelligence is becoming increasingly important in medicine. In particular, deep learning-based pattern recognition methods can advance the field of pathology by incorporating clinical, radiologic, and genomic data to accurately diagnose diseases and predict patient prognoses. In this review, we present an overview of artificial intelligence, the brief history of artificial intelligence in the medical domain, recent advances in artificial intelligence applied to pathology, and future prospects of pathology driven by artificial intelligence.

Key Words: Artificial intelligence; Deep learning; Pathology; Image analysis

Artificial intelligence (AI) denotes the intelligence presented by some artificial entities including computers and robots. While AI has only recently received such a large amount of attention, the idea of mechanical thinking can be found in the earliest myths and literature.¹ In the modern era, efforts to model the logical thinking process have continued, and a conceptual machine that is capable of performing arbitrary logical computations was proposed by Turing in 1950.² He believed that the ultimate form of AI would be indistinguishable from humans, and proposed the Turing test as an evaluation method for the intelligence level of machines; this test later faced a number of refutations, including the Chinese room argument in 1980.³ In early 2000, Russell and Norvig⁴ suggested the concept of an intelligent agent that can automatically plan and perform a series of actions to achieve a goal as a new form of AI, and recently this has been the major focus of AI research.

Several approaches have been taken in the history of AI research.^{1,4,5} The first is the human brain simulation approach, in which the human brain is modeled as a network of artificial neurons that receive input signals, process them, and transmit new signals to succeeding neurons. The perceptron is one simple form of such an artificial neural network for recognizing patterns. Symbolic AI is another one that uses symbols and relations to

represent human knowledge and uses logical rules to deduce new knowledge to solve intellectual problems. Expert systems are the major product of such an approach, and they have received considerable attention from the industry. Another notable form of artificial neural network is the soft computing approach, including fuzzy logic systems and evolutionary algorithms. This approach has worked well for problems where a sub-optimal, approximate solution is sufficient. The last approach is the statistical learning approach, which relies on statistical data analysis to gather inherent rules that are implicitly represented in raw data. In spite of its lack of explainability, the statistical learning approach is currently the dominant AI research methodology, backed by the success of deep learning.

Deep learning (DL) is a subfield of machine learning (ML) that is based on neural networks comprising several nested layers of neurons. ML, which can be regarded as an alias of statistical learning, is a method of creating a task-specific statistical model from a given dataset. It has been used successfully in several data mining and pattern recognition tasks, including loan default prediction and spam mail filtering.^{6,7} Typical ML tasks require domain-specific feature modeling to extract effective information from raw data with the knowledge of domain experts, followed by statistical modeling and learning steps. Linear and logistic

regression models, tree-based decision models, and support vector machines (SVM) are famous statistical models that are frequently involved in ML tasks. The major difference between DL and ML is that DL can be done in an end-to-end manner without the feature modeling steps, which tend to be tedious. In DL, appropriate feature models can also be learned from data into the form of convolution filters or multi-dimensional embedding vectors.

The success history of DL begins in the field of visual object recognition. In the ImageNet large-scale visual recognition challenge (ILSVRC) 2012, Krizhevsky *et al.*⁸ demonstrated the excellent performance of their convolutional neural network (CNN), which outperformed the traditional computer vision-based approaches. In 2015, Google DeepMind published a paper about an AI that could learn a human-level control of several Atari 2600 games by trial and error,⁹ which inspired the AI research community with the idea of deep reinforcement learning. It was somewhat shocking when AlphaGo beat the professional Go player Lee Sedol by 4–1 in 2016 because the game of Go had been regarded as too complex to be well played by the computer for a long time. Moreover, AlphaGo Zero showed that it could beat the AlphaGo 2016 with a >90% win rate without any prior human knowledge about the game of Go.¹⁰ Speech recognition is another major field of AI research. While several good features and methods had been devised to transform speech signals into text, Baidu Research presented Deep Speech, which showed that an end-to-end DL method could work very well in the speech recognition domain, obtaining a 16.0% word error rate, as compared to an 18.4% error rate for the previous state of the art technology.¹¹ Automatic translation of text between different languages is one of the most difficult natural language processing tasks, where attention-based recurrent neural network (RNN) models have been successfully applied to get bilingual evaluation understudy (BLEU) scores of 25.9 and 26.3, respectively, in English-to-German translation.^{12,13} The more complex task of visual question answering (VisualQA), where textual questions are answered based on a given image or video, has been pursued since its proposal in 2015.¹⁴ A recent study showed promising results, with accuracy near 62%, as compared to a human’s accuracy of 83%.¹⁵

CNN and RNN are the two most famous DL models for pattern recognition tasks, the former for images and the latter for sequential data like audio and text. Typical CNNs are composed of several convolutional layers followed by a few fully connected layers and a task-specific output layer.¹⁶ High-performance CNN models have more complicated structures that incorporate much more convolutional, pooling, and normalization

layers; skip connections and residual connections; branching and merging, etc. An example of modern CNN architecture is shown in Fig. 1. The GoogLeNet is one such model that won the ILSVRC 2014 with a top-5 error rate of 6.67%.¹⁷ RNNs have a special ability to maintain their hidden state in their recurrent layers, which can be regarded as a summary of all their previous input elements. A typical recurrent layer is depicted in Fig. 2, where the input sequence is processed element-wise along with the current hidden state, updating the hidden state and pro-

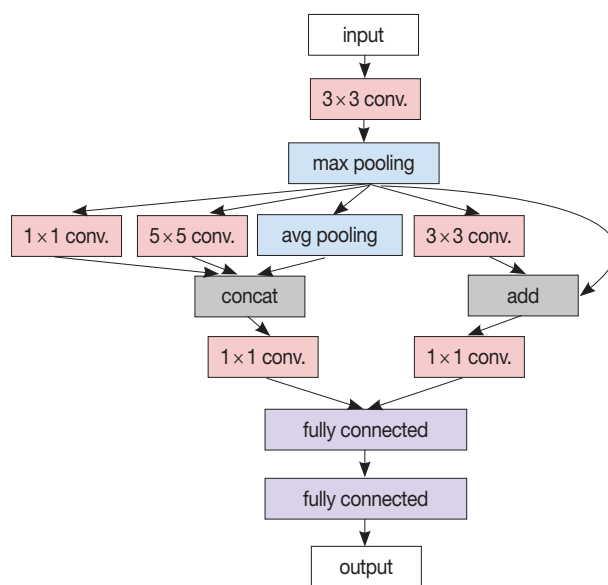


Fig. 1. A simplified modern convolutional neural network (CNN) architecture example. In contrast to the classic CNN comprising only a cascade of convolution layers and pooling layers followed by a few fully connected layers, this example has various other concepts like branching from the max pooling layer to several (1 × 1, 3 × 3, 5 × 5) convolution layers as well as the average pooling layer, merging by concatenation from two (1 × 1, 5 × 5) convolution layers and the average pooling layer, and residual addition of max pooling layer output to the output of its succeeding (3 × 3) convolution layer.

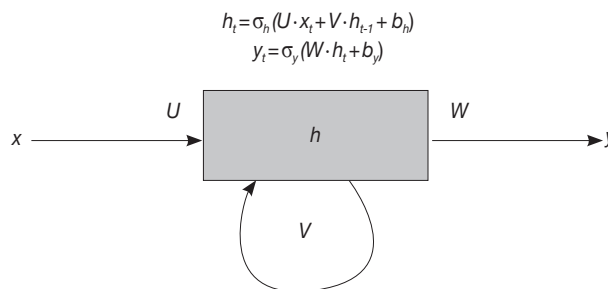


Fig. 2. A typical recurrent layer example. In receiving a new input x_t at time t , hidden state h_t is updated based on x_t and the previous state h_{t-1} first, then output y_t is generated based on h_t . At training time, parameters like U , V , W , b_h , and b_y are trained to accurately generate y_t for every time t .

ducing the output for the current input element.¹⁸ Long short-term memory (LSTM)¹⁹ units are a kind of recurrent neuron that has additional learnable gates to prevent itself from losing important information on the input element that was given much earlier; LSTM units are a major component in modern RNN architectures.

The list of important terms and abbreviations appearing in this paper is given in Table 1.

HISTORY OF ARTIFICIAL INTELLIGENCE IN MEDICINE

Since the earliest stage of modern AI research, substantial efforts have been made in the medical domain. A script-based chatbot named ELIZA was proposed in 1966.²⁰ ELIZA's most famous script, DOCTOR, could interact with humans as a Rogerian psychotherapist. A biomedical expert system, MYCIN, presented in 1977, could analyze infectious symptoms to derive causal bacteria and drug treatment recommendations.²¹ Later, in 1992, the probabilistic reasoning-equipped PATHFINDER expert system was developed for hematopathology diagnosis, to deal with uncertain biomedical knowledge efficiently.^{22,23}

Before the era of DL, several ML methods have been used widely in the medical domain. Moreover, the invention of digital medical imaging such as digital X-ray imaging, computed tomography and magnetic resonance imaging enabled computerized image analysis, where AI achieved another success in the medical domain. In 1994, Vyborny and Giger²⁴ reviewed the efforts to use ML algorithms featuring computer vision in several mammography analysis tasks, including microcalcification detection, breast mass detection and differentiation of benign from malignant lesions. They demonstrated the efficacy of computer-aided detection (CAD) by comparing the performance of radiologists with

CAD to that of radiologists only. Later, in 2001, Kononenko²⁵ overviewed the typical ML methods such as decision trees, Bayesian classifiers, neural networks, and k nearest neighbor (k-NN) search, then reviewed their use in medical diagnosis and proposed evaluation criteria including performance, transparency, explainability and data resiliency. In 2003, however, Baker *et al.*²⁶ pointed out that the performance of commercial CAD systems was still below the expectation (max case sensitivity 49%) in detecting architectural distortion of breast mammography.

After the success of deep CNN in image classification, a wide range of attempts were made to apply DL to medicine. A notable success was the work of Gulshan *et al.*²⁷ in 2016, where retinal fundus images were analyzed by a CNN-based DL model to detect diabetic retinopathy lesions, achieving an area under the receiver operating characteristic curve (AUC) of 0.991, sensitivity of 97.5% and specificity of 93.4% in the high sensitivity setting, measured on the EyePACS-1 data set. In 2017, Litjens *et al.*²⁸ reviewed major DL methods suitable for medical image analysis and summarized more than 300 contributions in the neuro, retinal, pulmonary, breast, cardiac, abdominal, and musculoskeletal areas as well as in the digital pathology domain; contributions were well categorized according to their inherent type of image analysis: classification, detection, segmentation, registration, etc. Kohli *et al.*²⁹ presented another review on the application of ML to radiology research and practice, where transfer learning and data augmentation were emphasized as a viable solution to data-limited situations. Shaikhina and Khovanova³⁰ proposed another solution for a similar situation; their proposed solution incorporates multiple runs and the surrogate data test, which exploits statistical tools to guide the trained ML model having better model parameters and not being overfitted to a small training data set.

Genomics and molecular biology have been strongly connected

Table 1. List of terms and abbreviations appearing in this paper

Term	Abbreviation	Explanation
Artificial intelligence	AI	Intelligence represented by artificial things
Machine learning	ML	Data-driven statistical learning approach to AI
Deep learning	DL	Deep neural network based ML
Convolutional neural network	CNN	Neural network suitable for data with locality, e.g. image
Recurrent neural network	RNN	Neural network suitable for data with order dependency, e.g. sentence
Long short-term memory	LSTM	Recurrent neuron suitable for learning long-term dependency
Support vector machine	SVM	ML method that separates with regard to the trained hyperplane
k-nearest neighbor (search)	k-NN	ML method that classifies based on the classes of k similar training data
Conditional random field	CRF	ML method suitable for data with spatial/temporal dependency
Markov decision process	MDP	Modeling framework for a series of decisions and resulting outcomes
Multiple instance learning	MIL	ML approach suitable for labeled sets (whole slides) of unlabeled instances (lesions)
Region-of-interest	ROI	Image region containing things of predefined interest, e.g. nuclei, stroma, etc.
Area under receiver operating characteristic curve	AUC	Performance measure based on the area under the receiver operating characteristic curve, varying from 0.5 (lowest) to 1.0 (highest)

to the medical domain since genome sequencing became real. Next-generation sequencing (NGS) technology allows a whole genome sequence to be translated into text composed of ATCG, so that necessary computational analysis can be done for disease diagnosis and therapeutic decision making. In 2016, Angermueller *et al.*³¹ reviewed DL methods and their application to genomic and biological problems such as molecular trait prediction, mutation effect prediction, and cellular image analysis. They thoroughly reviewed the whole process used to apply DL to their problems, from data acquisition and preparation to overfit avoidance and hyperparameter optimization. Torkamani *et al.*³² presented a review of high-definition medicine, which is applied to personalized healthcare by using several kinds of big data, including DNA sequences, physiological and environmental monitoring data, behavioral tracking data and advanced imaging data. Surely, DL techniques can help in analyzing those big data datasets in parallel, to provide exact diagnosis and personalized treatment. Another review was done in 2018 by Wainberg *et al.*³³ on the use of DL in various biomedical domains, including quantitative structure-activity relationship modeling for drug discovery and identification of pathogenic variants in genome sequences. They re-emphasized the importance of the performance, transparency, model interpretability and explainability of DL methods, in earning the trust of stakeholders gaining adoption. Besides these reviews, there exist two notable contributions for genetic variants. Xiong *et al.*³⁴ presented a computational model for gene splicing, which can predict the ratio of transcripts with the central exon spliced in, within the whole set of transcripts spliced from any given sequence containing an exon triplet. Recently an award-winning deep CNN-based variant caller named DeepVariant was announced,³⁵ which is able to call genetic variation in aligned NGS read data by learning on images created upon the read pileups around putative variant sites.

Another type of medical data to be analyzed is electronic health records (EHR). Rajkomar *et al.*³⁶ recently published their work building a DL model that predicts multiple medical events, including in-hospital mortality, unplanned readmission, and prolonged length of stay, entirely from raw EHR records based on the Fast Healthcare Interoperability Resources format. Their model could accurately predict mortality events, with an AUC of 0.90 at patients' admission, and even with an AUC of 0.87 at 24 hours before admission to the hospital. EHR data can be used in the prediction of other types of events, e.g., outcome of a patient biopsy, which could be predicted with AUC 0.69 in the work of Fernandes *et al.*³⁷

Besides the analytical diagnostic tasks, AI has been tried in

other areas, for example, an intelligent assistant named Secretary-Mimicking Artificial Intelligence that helps in the execution of a pathology workflow was presented by Ye.³⁸ Treatment decision is another important factor in patient healthcare, from both prognostic and financial perspectives. Markov decision analysis is an effective tool in such situations, which was used to solve the cardiological decision problem in the work presented by Beck *et al.*³⁹ Schaefer *et al.*⁴⁰ reviewed the medical treatment modeling using the Markov decision process, which is a modeling tool that fits well in the optimization of sequential decision making and is strongly related to reinforcement learning.⁴¹

ARTIFICIAL INTELLIGENCE APPLICATION IN PATHOLOGY

Microscopic morphology remains the gold standard in diagnostic pathology, but the main limitation to morphologic diagnosis is diagnostic variability in bearing error among pathologists. The Gleason grading system is one of the most important prognostic factors in prostate cancer. However, significant interobserver variability has been reported when pathologists have used the Gleason grading system.^{42,43} In order to get a consistent and possibly more accurate diagnosis, it is natural to introduce algorithmic intelligence in the pathology domain, at least in the morphological analysis of tissues and cells. With the help of digital pathology equipment varying from microscopic cameras to whole slide imaging scanners, morphology-based automated pathologic diagnosis has become a reality. In this review, we focus on morphology-based pathology: diagnosis and prognosis based on the qualitative and quantitative assessment of pathology images. Typical digital image analysis tasks in diagnostic pathology involve segmentation, detection, and classification, as well as quantification and grading.⁴⁴ We briefly introduce typical techniques used for AI in digital pathology and a few notable research studies per disease. The list of studies reviewed in this paper is given in Table 2.

TYPICAL TECHNIQUES

Digital pathology images used in AI are mostly scanned from H&E stained slides. Pathology specimens undergo multiple processes, including formalin fixation, grossing, paraffin embedding, tissue sectioning, and staining. Each step of the process and the different devices and software used with the digital imaging scanners can affect aspects of the quality of the digital images, such as color, brightness, contrast, and scale. For the best results,

Table 2. List of research works in applications of artificial intelligence to image analysis based pathology

Author (year)	Disease	Data	Task	Model	Augmentation	Performance
Garud <i>et al.</i> (2017) ⁴⁶	Breast cancer	FNA cytology/175 (images)	Decision Benign/cancer	GNN	None	Image level decision acc. 89.7%
Li and Ping (2018) ⁴⁷	Lymph node metastasis	CAMELYON16/400 (WSIs)	Decision Yes/no	GNN + CRF	Color jitter, rotation, etc.	Patch level decision acc. 93.8%
Rannen Triki <i>et al.</i> (2018) ⁴⁸	Breast cancer	Frozen section OCT1/4,921 (frames)	Decision Benign/cancer	GNN	None	Patch level decision acc. 94.96%
Ehteshami Bejnordi <i>et al.</i> (2018) ⁴⁹	Breast cancer	BREAST Stamp/2,387 (WSIs)	Decision Benign/cancer	GNN + GNN	None	WSI level decision AUC 0.962
Lijens <i>et al.</i> (2016) ⁵⁰	Lymph node metastasis	Lymph node specimen/271 (samples)	Decision Yes/no	GNN	None	Sample level decision AUC 0.90
Cireřan <i>et al.</i> (2013) ⁵¹	Breast cancer	MITOS/300 mitosis in 50 images	Mitosis detection	GNN	Rotation, flip, etc.	Detection F1-score 0.782
Teramoto <i>et al.</i> (2017) ⁵²	Lung cancer	FNA cytology/298 (images)	Classification Adeno-Squamous cell Small cell	GNN	Rotation, flip, etc.	Overall classification acc. 71.1%
Yu <i>et al.</i> (2016) ⁵³	Lung cancer	TCGA-LUAD/1,074 TCGA-LUSC/1,111 Stanford TMA/294 (samples)	Decision Benign/cancer Survival analysis	SVM	None	Patch level decision AUC 0.85
Coudray <i>et al.</i> (2018) ⁵⁴	Lung cancer	TCGA lung cancer/1,635 (samples)	Classification Adeno-Squamous cell Benign Multi-task decision Gene mutation	GNN	None	Overall classification AUC 0.97 STK11 mutation decision AUC 0.85
Campanella <i>et al.</i> (2018) ⁵⁵	Prostate cancer	Needle biopsy/12,160 (samples)	Decision Benign/cancer	GNN (ML)	None	Sample level decision AUC 0.979
Anvanti <i>et al.</i> (2018) ⁵⁶	Prostate cancer	TMA/886 (samples)	Classification Gleason score	GNN+scoring rule	Rotation, flip, color jitter	Model-pathologist Cohen's kappa 0.71
Zhou <i>et al.</i> (2017) ⁵⁷	Prostate cancer	TCGA-PRAD/368 (cases)	Decision 3+4/4+3	GNN	None	Sample level decision acc. 75%
Nagpal <i>et al.</i> (2018) ⁵⁸	Prostate cancer	TCGA-PRAD+ others/train 1,226, test 331 (slides)	Classification Gleason group Survival analysis	GNN + k-NN	None	Overall classification acc. 70% C-index 0.697
Lijens <i>et al.</i> (2016) ⁵⁰	Prostate cancer	Needle biopsy / 225 (WSIs)	Decision Benign/cancer	GNN	None	Slide level decision AUC 0.99
Ertosun and Rubin (2015) ⁵⁹	Brain cancer	TCGA-GBM & LGG (unknown size)	Classification GBM LGG grade 2 LGG grade 3	GNN + GNN	Color transform to H&E	GBM/LGG decision acc. 96% LGG grade decision acc. 71%
Mobadersany <i>et al.</i> (2018) ⁶⁰	Brain cancer	TCGA-GBM & LGG/1,061 (samples)	Survival analysis	GNN	Rotation, normalization	C-index 0.754
Wu <i>et al.</i> (2018) ⁶¹	Ovarian cancer	Biopsy/7,392 (images)	Classification Subtypes	GNN	Rotation, image enhancement	Overall classification acc. 78.2%
Zhang <i>et al.</i> (2017) ⁶²	Cervix cancer	HEMLBC/1,978 Herlev/917 (images)	Decision Benign/cancer	GNN	Rotation, translation, etc.	Image level decision AUC 0.99
Xu <i>et al.</i> (2017) ⁶³	Sickle cell disease	Red-blood cell/7,206 (patches)	Classification Cell types	GNN	Rotation, flip, translation, etc.	Cell level classification acc. 87.5%
Meier <i>et al.</i> (2018) ⁶⁴	Gastric cancer	TMA/469 (samples) CD8/Ki67 IHC	Survival analysis	GNN	None	Stratification by risk successful (p < .01)
Xie <i>et al.</i> (2016) ⁶⁵	-	Synthetic fluorescence microscopy cell/ 200 (images)	Cell counting	GNN	None	Mean absolute error < 2%
Tuominen <i>et al.</i> (2010) ⁶⁶	-	IHC stained breast cancer slides/100	Cell counting	Comp. vision	None	Correlation coefficient 0.98

GNN, convolutional neural network; ML, multiple instance learning; SVM, support vector machine; AUC, area under receiver operating characteristic curve; k-NN, k-nearest neighbor; WSI, whole slide image; CRF, Conditional random field; TCGA, The Cancer Genome Atlas; TMA, tissue microarray; IHC, immunohistochemistry; GBM, glioblastoma multiforme; LGG, lower grade glioma.

it is strongly recommended to alleviate the effect of these variations before using the images in automated analysis work.⁴⁵ Normalization is one of the techniques used to reduce such variations. Simple linear range normalization based on the equation $[v_{\text{new}} = (v_{\text{old}} - a) / f_{\text{scale}} + b]$ is generally used for the pixel values in grayscale images, or for each channel of color images.^{47,60} Scale normalization has not been reported in related works, as they all have used a single image acquisition device, e.g., a certain microscopic camera or digital slide scanner. When multiple image acquisition devices are used, scale normalization is of concern, since images acquired from different devices can have different pixel sizes, even at the same magnification level.

Detecting the region-of-interest (ROI) has been done by combining several computer vision operations, such as color space conversion, image blurring, sharpening, edge detection, morphological transformation, pixel value quantization, clustering, and thresholding.⁶⁷ Color space conversion is often done before pixel clustering or quantization, to separate chromatic information and intensity information.⁵³ Another type of color space conversion targets direct separation of color channels for hematoxylin (H), eosin (E) and diaminobenzidine from stained tissue images to effectively obtain nuclei area.^{37,59,66,68} Thresholding based on a certain fixed value leads to low-quality results when there are variations in luminance in the input images. Adaptive thresholding methods like hysteresis thresholding and Otsu's method can generate better thresholding results.^{47,53,59,69} Recently, pixel-wise or patch-wise classifiers based on CNN have been used widely in ROI detection,^{44,49-51,54-56,58,65} where a deep CNN is trained to classify the type of target pixel or patch centered on the larger input image patch in a sliding window manner. Semantic segmentation CNN is another recent trend for this task,^{65,70,71} which can detect multiple ROIs in a given image without sliding window operation, resulting in much faster speed.

In the development of a CNN-based automated image analysis, data-limited situations are common in the medical domain, because it is very costly and time-consuming to build a large amount of annotated, high-quality data.⁴⁵ As previously mentioned, transfer learning and data augmentation should be incorporated to get a better result. In transfer learning, convolutional layer parameters of a CNN, pre-trained with a well-known dataset like ImageNet, are imported into the target CNN as layer initialization, while later layers like fully connected layers or deconvolutional layers are initialized randomly.^{62,70,71} Additional training steps can update all of the layer parameters, including the imported ones, or only the parameters of the layers that were randomly initialized. With sufficient data, building a model without transfer

learning is reported to give better performance.⁵⁴

A common strategy of image data augmentation is, for the given image, applying various transformations that do not alter the essential characteristics; such transformations include rotation (90°, 180°, and 270°), flipping (horizontal/vertical), resizing, random amounts of translation, blurring, sharpening, adding jitters in color and/or luminance, contrasting histogram equalization, etc.^{47,51,52,56,60-63} Another type of augmentation relates to the patch generation strategy; applying large medical images directly to the CNN is impractical. From a large pathological image, with a size between 1024 × 1024 (camera) and > 10⁴ × 10⁴ (scanner) pixels, smaller patches with sizes between 32 × 32 and 512 × 512 pixels are retrieved for use in training and inference of CNNs. Instead of using the pre-generated set of image patches through the whole training process, resampling patches during each training epoch can introduce more variance in training data to reduce the chance of overfitting.⁶⁰

After the patch-level CNN is trained, another ML model is often developed for the whole image level decision. In this case, a patch-level decision is made for every single patch in the training images to generate heatmap-like output, from which several features are extracted via conventional image analysis methods. Then, collected feature values for the training images are fed into the target image level ML model. An example workflow for developing and using this two-stage pathology AI is depicted in Fig. 3.

EXAMPLES OF PATHOLOGY ARTIFICIAL INTELLIGENCE

CNN-based breast cancer diagnosis was tried with fine needle aspiration (FNA) cytology images,⁴⁶ optical coherence tomography (OCT) images,⁴⁸ and H&E stained tissue images,⁴⁹ each with varying numbers of data points and model structures. A total of 175 cytology images captured by a microscopic camera at 40× magnification level were manually split into 918 ROIs, 256 × 256 pixels in size, where each ROI had multiple cells.⁴⁶ A CNN was trained to determine the malignancy of a given ROI, and the cytological image was classified as malignant when > 30% of the ROIs in the image were malignant. The reported accuracy was 89.7%, which was far inferior to the 99.4% accuracy of a random forest classifier with 14 hand-crafted features. In order to attempt an automated intraoperative margin assessment, 4,921 frame images from the frozen section OCT were used, from which patches 64 × 64 pixels in size were extracted, resized to 32 × 32 pixels, and used for training and evaluation.⁴⁸ Patch-level CNN performance was

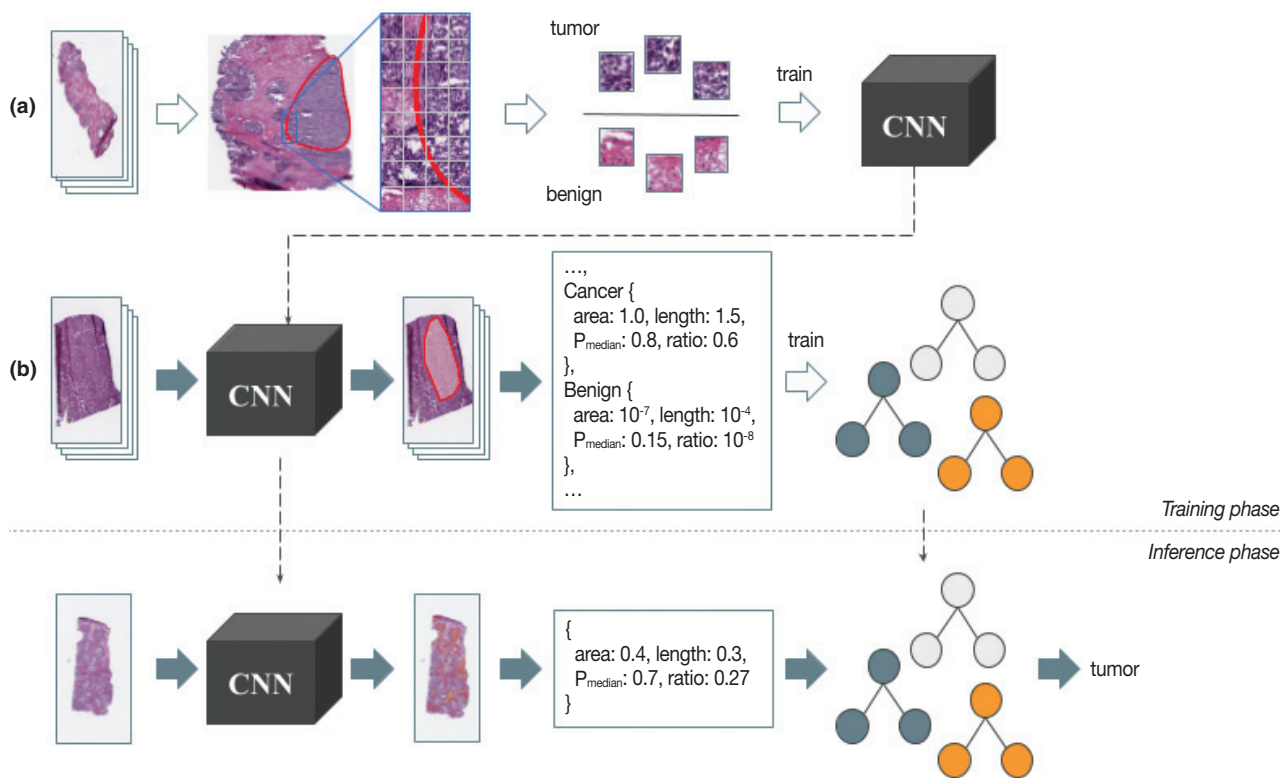


Fig. 3. An example workflow for two-stage pathology artificial intelligence. Training phase: from the collected pathology images, a proper amount of annotation data is constructed (a). Image patch sets of balanced size are used in the training of patch-level convolutional neural network (CNN). After the patch-level CNN is trained sufficiently, heatmaps are generated for another set of pathology images using that CNN, from where the features are extracted for the decision forest like image-level machine learning (ML) model training (b). Inference phase: patch-level CNN runs on every single patch in the input pathology to generate a heatmap (first stage). Features are then extracted as in the training phase, and fed into the image-level ML model to determine the image-level result (second stage).

measured, giving an accuracy of 95.0% and AUC of 0.984 in the best setting. In another study, 2,387 H&E stained breast biopsies were scanned at a magnification of $20\times$.⁴⁹ Multiple CNNs were used in this study: the first CNN classified each image pixel as fat, stroma, or epithelium; the second CNN predicted whether each stromal pixel was associated with a cancer; and the third CNN determined the whole-slide-level malignancy. The reported slide level AUC was 0.962. A notable result is that, while the CNNs were trained with stromal tissues in benign slides and invasive cancer slides only, the predicted cancer association probability of the stroma near the ductal carcinoma *in situ* (DCIS) lesion properly related to the severity of DCIS. CNN-based lymph node metastasis detection was also tried with a different model and dataset.^{47,50} Conditional random field was adopted on top of convolutional layers in order to regulate the metastasis prediction.⁴⁷ From the whole slide images (WSIs) in the CAMELYON16 dataset,⁷² benign and tumor image patches 768×768 pixels in size were sampled to train and validate the model, giving patch-level accuracy of 93.8% after incorporating data augmentation methods. In

another study, 271 WSIs scanned at a magnification of $20\times$ were used in developing a CNN-based model for detecting micro- or macro-metastasis-free slides.⁵⁰ Region-level annotations on training images were utilized. Slide-level metastasis detection was performed after metastasis probability map generation by patch-level CNN, incorporating probability thresholding (>0.3) and connected component analysis to remove small lesions (<0.02 mm diameter), resulting in a detection AUC of 0.90. Mitosis detection was tried with a CNN that decides whether the center of the given image is mitotic or not,⁵¹ trained and evaluated with 50 images from five biopsy slides containing about 300 mitoses total, adopting data augmentation techniques including patch rotation and flipping. In the evaluation, a mitosis probability map was created for the given image, and pixels with locally maximal probabilities were considered as mitotic, resulting in detection F1-score 0.782.

Automatic lung cancer subtype determination was tried with FNA cytology images and H&E stained WSIs.^{52,54} A total of 298 images from 76 cases acquired using a microscopic camera at

40× magnification level were utilized in developing a CNN receiving 256×256 pixel images as input; the dataset comprised 82 adenocarcinomas, 125 squamous cell carcinomas, and 91 small cell carcinomas.⁵² Data augmentation techniques like rotation, flipping, and Gaussian filtering were adopted to enhance the classification accuracy from 62.1% to 71.1%. A total of 1,635 WSIs from the The Cancer Genome Atlas (TCGA)⁷³ dataset were used in detection of lung cancer type with CNN.⁵⁴ Each input patch (512×512 pixels) was classified as adenocarcinoma, squamous cell carcinoma or benign, and then the averaged probability of non-benign patches was used in the slide-level decision, resulting in slide level classification AUC of 0.97, which is much superior to the previous SVM-based approach.⁵³ Moreover, by using the multi-task transfer learning approach, mutations of six genes including *KRAS*, *EGFR*, and *STK11* were independently able to be determined on the input WSI of lung adenocarcinoma patches. The mutation detection had an AUC of 0.86 for *STK11* and an AUC of 0.83 for *EGFR*.

Prostate cancer diagnosis has been one of the most active fields in adopting DL because of its large dependence on tissue morphology. Prostatic tissues from various sources have been used in malignancy and severity decisions.^{50,55-58} In one study, 225 prostate needle biopsy slides were scanned at 40× magnification, and malignant regions were annotated in developing a cancer detector.⁵⁰ A CNN-based patch-level cancer detection was performed for every overlapping patch in a slide to generate a probability map, and a cumulative probability histogram was created and analyzed in slide-level malignancy determination (AUC 0.99). In another study, 12,160 needle biopsy images were utilized in developing a CNN-based slide-level malignancy detector.⁵⁵ To train a patch-classifying CNN with no patch/region-level manual annotation, multiple instance learning was used; with a large number of WSIs (>8,000), the result was useful (AUC 0.98). A total of 886 tissue microarray (TMA) samples were used in a trial of automated Gleason scoring,⁵⁶ where 508 TMA images for training were manually segmented into combinations of benign, Gleason pattern 3, 4, and 5; 133 TMA images were used for tuning and 245 images were used for validation. The TMA level score was determined by the two most dominant patterns measured from the per-pattern probability maps generated by a trained patch-level CNN classifier. In grading the validation set, Cohen's kappa between two pathologists was 0.71, while those between the model and each of the two pathologists were 0.75 and 0.71. 342 cases from TCGA, teaching hospital and medical lab were utilized in training automated Gleason scoring system,⁵⁸ where CNN and k-NN classifier were

ensembled. A total of 912 slide images were annotated with the region level to be used in training CNN to generate a pattern map for a given slide image; 1,159 slides were used to train the k-NN classifier that determines the Gleason group for the given pattern map statistics. The reported grading accuracy measured on 331 slides was 0.70, while the average accuracy of 29 general pathologists was 0.61, which is superior to the previous TCGA-based result that showed 75% accuracy in discriminating Gleason score 3 + 4 and 4 + 3.⁵⁷

An automated determination of brain cancer severity was tried with TCGA brain cancer data.⁵⁹ A cascade of CNNs was used: an initial CNN trained with 22 WSIs for discriminating between glioblastoma (GBM) and low-grade glioma (LGG), and a secondary CNN trained with an additional 22 WSIs for discriminating between LGG grades 2 and 3. Each H&E-stained RGB color image was transformed into an H-stained channel and an E-stained channel, and only the H-stained channel was used for further analysis. The first CNN showed GBM/LGG discrimination accuracy of 96%, but the LGG grade discrimination was not so successful (71%). Survival analysis using CNN was also tried.⁶⁰ Again, 1,061 WSIs from TCGA dataset were used. For each training epoch, 256×256 pixel patches were sampled from manually identified, 1,024×1,024 pixel ROIs. At diagnosis, ROI-wise risk was determined as the median risk of nine patches sampled from the ROI, and the sample-level risk was determined as the second highest risk among ROI risks. The measured c-index of this kind of survival analysis was 0.75, which was elevated to 0.80 by modifying the CNN to receive the mutation information at its fully connected layer.

Ovarian cancer subtype classification based on CNN was tried.⁶¹ 7,392 images were generated by splitting and cropping the original images acquired by the microscopic camera at 40× magnification level. Rotation and image quality enhancement were used in the data augmentation phase, which enhanced the classification accuracy from 72.8% to 78.2%. Cervical cancer diagnosis on cytological images was also tried.⁶² Without cell-wise segmentation, nuclei-centered cell patches were sampled from the original cytology image, followed by augmentation operations like rotation and translation. Convolutional layer parameters that were trained by using ImageNet data were transferred to actual CNN. Herlev and HEMLBC datasets were used in evaluation, giving 98.3% and 98.6% accuracy, respectively, in five-fold cross-validation. Red blood cell (RBC) classification is crucial in sickle cell disease diagnosis. A CNN-based automatic RBC classification was tried,⁶³ where 7,206 cell patches were generated from 434 microscopic images and used for training and testing of

the classifier. Rotation and flipping were used to augment training data. Five-fold cross-validation showed an average accuracy of 89.3% in five-class coarse classification, and 87.5% in eight-class refined classification. A total of 469 TMA cores from the gastric cancer patients were used in a CNN-based survival analysis.⁶⁴ CD8 and Ki67 immunostained images were acquired and fed into separate patch-wise risk-predicting CNNs for each stain. From the differential analysis between the low-risk group and the high-risk group, it was claimed that the density of CD8 cells was largely related to the risk level.

FUTURE PROSPECTS

We have provided an overview of various medical applications of AI technology, especially in pathology. It is encouraging that the accuracy of automated morphological analyses has improved due to DL technology. The pathologic field in AI is expanding to disease severity assessment and prognosis prediction. Although most AI research in pathology is still focused on cancer detection and the grading of tumors, pathological diagnosis is not simply a morphological diagnosis, but is a complex process of evaluation and judgment of various types of clinical data that deal with various organs and diseases. A large amount of data, including genetic data, clinical data, and digital images, is needed to develop AI that covers the range of clinical situations. There are a number of public medical databases, including TCGA, and a number of studies have been done based on those databases. They provide a good starting point in researching and developing a medical AI, but it requires much more high-quality data; e.g., detailed annotations on a large number of pathology images, created and validated by several experienced pathologists, are necessary to develop a pathology-image-analyzing AI that is comparable to human pathologists.

There are difficulties in constructing such high-quality data in reality, largely due to the protection of privacy, proprietary techniques, and the lack of funding and pathologists to participate in the annotation process. To overcome this data insufficiency, as we have mentioned earlier, several techniques have been introduced, such as transfer learning and data augmentation. Still, these techniques are sub-optimal; transfer learning cannot guarantee the optimal convolutional filters specific for the task, and data augmentation cannot deal with the unseen data and patterns. The ultimate solution is to construct a large amount of thoroughly labeled and annotated medical data, through the cooperation of multiple hospitals and medical laboratories. To accelerate the construction of such a dataset, efficient tools for labeling and annotating

are required, which can be assisted by another type of AI.⁴⁵

Eventually, there will be a medical AI of the prognostic prediction model, combining clinical data, genetic data, and morphology. Also, a new grading system applicable to several tumors can be created by an AI model that has learned from the patient's prognosis combined with a number of variables including morphology, treatment modality, and tumor markers, etc. This will also help to overcome the poor reproducibility and the variety of current grading and staging results among pathologists, leading to much better clinical outcomes for patients.

ORCID

Hye Yoon Chang: <https://orcid.org/0000-0002-4274-4652>
 Chan Kwon Jung: <https://orcid.org/0000-0001-6843-3708>
 Junwoo Isaac Woo: <https://orcid.org/0000-0002-8754-8217>
 Sanghun Lee: <https://orcid.org/0000-0003-1758-9619>
 Joonyoung Cho: <https://orcid.org/0000-0001-5380-0149>
 Sun Woo Kim: <https://orcid.org/0000-0001-8563-0471>
 Tae-Yeong Kwak: <https://orcid.org/0000-0001-9171-7258>

Conflicts of Interest

The authors declare that they have no potential conflicts of interest.

Acknowledgments

This study was approved by the Institutional Review Board of The Catholic University of Korea Seoul St. Mary's Hospital with a waiver of informed consent (KC18SNDI0512).

REFERENCES

- McCorduck P. Machines who think: a personal inquiry into the history and prospects of artificial intelligence. Natick: A.K. Peters, 2004.
- Turing AM. I. Computing machinery and intelligence. *Mind* 1950; 59: 433-60.
- Searle JR. Minds, brains, and programs. *Behav Brain Sci* 1980; 3: 417-24.
- Russell SJ, Norvig P. Artificial intelligence: a modern approach. Upper Saddle River: Prentice Hall, 2003.
- Artificial intelligence [Internet]. Wikipedia, 2018 [cited 2018 Dec 9]. Available from: https://en.wikipedia.org/wiki/Artificial_intelligence.
- Mortensen TL, Watt DL, Leistriz FL. Loan default prediction using logistic regression and a loan pricing model. Report No. 119549

- [Internet]. Fargo: North Dakota State University, 1988 [cited 2018 Dec 7]. Available from: <https://ideas.repec.org/p/ags/nddmrs/119549.html>.
7. Graham P. Better Bayesian filtering [Internet]. PAUL GRAHAM, 2003 [cited 2018 Nov 22]. Available from: <http://www.paulgraham.com/better.html>.
 8. Krizhevsky A, Sutskever I, Hinton GE. ImageNet classification with deep convolutional neural networks. In: Pereira F, Burges CJ, Bottou L, Weinberger KQ, eds. *Advances in neural information processing systems 25*. Red Hook: Curran Associates, Inc., 2012; 1097-105.
 9. Mnih V, Kavukcuoglu K, Silver D, *et al.* Human-level control through deep reinforcement learning. *Nature* 2015; 518: 529-33.
 10. Silver D, Schrittwieser J, Simonyan K, *et al.* Mastering the game of Go without human knowledge. *Nature* 2017; 550: 354-9.
 11. Hannun A, Case C, Casper J, *et al.* Deep speech: scaling up end-to-end speech recognition [Internet]. Ithaca: arXiv, Cornell University, 2014 [cited 2018 Nov 22]. Available from: <http://arxiv.org/abs/1412.5567>.
 12. Luong MT, Pham H, Manning CD. Effective approaches to attention-based neural machine translation. In: *Proceedings of the 2015 Conference on Empirical Methods in Natural Language Processing, 2015 Sep 17-21, Lisbon, Portugal*. Stroudsburg: Association for Computational Linguistics, 2015; 1412-21.
 13. Wu Y, Schuster M, Chen Z, *et al.* Google's neural machine translation system: bridging the gap between human and machine translation [Internet]. Ithaca: arXiv, Cornell University, 2016 [cited 2018 Nov 22]. Available from: <http://arxiv.org/abs/1609.08144>.
 14. Antol S, Agrawal A, Lu J, *et al.* VQA: visual question answering. In: *Proceedings of the IEEE International Conference on Computer Vision, 2015 Dec 7-13, Santiago, Chile*. Washington, DC: IEEE Computer Society, 2015; 2425-33.
 15. Kim JH, Lee SW, Kwak D, *et al.* Multimodal residual learning for visual QA. In: Lee DD, von Luxburg U, Garnett R, *et al.*, eds. *Advances in neural information processing systems 29*. Red Hook: NY Curran Associates Inc., 2016; 361-9.
 16. LeCun Y, Bottou L, Bengio Y, Haffner P. Gradient-based learning applied to document recognition. *Proc IEEE* 1998; 86: 2278-324.
 17. Szegedy C, Liu W, Jia Y, *et al.* Going deeper with convolutions. In: *Proceedings of the IEEE Conference on Computer Vision and Pattern Recognition, 2015 Jun 7-12, Boston, MA, USA*. Silver Spring: IEEE Computer Society Press, 2015; 1-9.
 18. LeCun Y, Bengio Y, Hinton G. Deep learning. *Nature* 2015; 521: 436-44.
 19. Hochreiter S, Schmidhuber J. Long short-term memory. *Neural Comput* 1997; 9: 1735-80.
 20. Weizenbaum J. ELIZA: a computer program for the study of natural language communication between man and machine. *Commun ACM* 1966; 9: 36-45.
 21. Shortliffe EH. Mycin: a knowledge-based computer program applied to infectious diseases. In: *Proceedings of the Annual Symposium on Computer Application in Medical Care, 1977 Oct 3-5, Washington, DC, USA*. New York: Institute of Electrical and Electronics Engineers, 1977; 66-9.
 22. Heckerman DE, Horvitz EJ, Nathwani BN. Toward normative expert systems: Part I. The Pathfinder project. *Methods Inf Med* 1992; 31: 90-105.
 23. Heckerman DE, Nathwani BN. Toward normative expert systems: Part II. Probability-based representations for efficient knowledge acquisition and inference. *Methods Inf Med* 1992; 31: 106-16.
 24. Vyborny CJ, Giger ML. Computer vision and artificial intelligence in mammography. *AJR Am J Roentgenol* 1994; 162: 699-708.
 25. Kononenko I. Machine learning for medical diagnosis: history, state of the art and perspective. *Artif Intell Med* 2001; 23: 89-109.
 26. Baker JA, Rosen EL, Lo JY, Gimenez EI, Walsh R, Soo MS. Computer-aided detection (CAD) in screening mammography: sensitivity of commercial CAD systems for detecting architectural distortion. *AJR Am J Roentgenol* 2003; 181: 1083-8.
 27. Gulshan V, Peng L, Coram M, *et al.* Development and validation of a deep learning algorithm for detection of diabetic retinopathy in retinal fundus photographs. *JAMA* 2016; 316: 2402-10.
 28. Litjens G, Kooi T, Bejnordi BE, *et al.* A survey on deep learning in medical image analysis. *Med Image Anal* 2017; 42: 60-88.
 29. Kohli M, Prevedello LM, Filice RW, Geis JR. Implementing machine learning in radiology practice and research. *AJR Am J Roentgenol* 2017; 208: 754-60.
 30. Shaikhina T, Khovanova NA. Handling limited datasets with neural networks in medical applications: a small-data approach. *Artif Intell Med* 2017; 75: 51-63.
 31. Angermueller C, Parnamaa T, Parts L, Stegle O. Deep learning for computational biology. *Mol Syst Biol* 2016; 12: 878.
 32. Torkamani A, Andersen KG, Steinhubl SR, Topol EJ. High-definition medicine. *Cell* 2017; 170: 828-43.
 33. Wainberg M, Merico D, Delong A, Frey BJ. Deep learning in biomedicine. *Nat Biotechnol* 2018; 36: 829-38.
 34. Xiong HY, Alipanahi B, Lee LJ, *et al.* RNA splicing: the human splicing code reveals new insights into the genetic determinants of disease. *Science* 2015; 347: 1254806.
 35. Poplin R, Chang PC, Alexander D, *et al.* A universal SNP and small-indel variant caller using deep neural networks. *Nat Biotechnol* 2018; 36: 983-7.
 36. Rajkomar A, Oren E, Chen K, *et al.* Scalable and accurate deep

- learning with electronic health records. *NPJ Digit Med* 2018; 1: 18.
37. Fernandes K, Chicco D, Cardoso JS, Fernandes J. Supervised deep learning embeddings for the prediction of cervical cancer diagnosis. *PeerJ Comput Sci* 2018; 4: e154.
 38. Ye JJ. Artificial intelligence for pathologists is not near: it is here: description of a prototype that can transform how we practice pathology tomorrow. *Arch Pathol Lab Med* 2015; 139: 929-35.
 39. Beck JR, Salem DN, Estes NA, Pauker SG. A computer-based Markov decision analysis of the management of symptomatic bifascicular block: the threshold probability for pacing. *J Am Coll Cardiol* 1987; 9: 920-35.
 40. Schaefer AJ, Bailey MD, Shechter SM, Roberts MS. Modeling medical treatment using Markov decision processes. In: Brandeau ML, Sainfort F, Pierskalla WP, eds. *Operations research and health care: a handbook of methods and applications*. Boston: Kluwer Academic Publisher, 2004; 593-612.
 41. Alagoz O, Hsu H, Schaefer AJ, Roberts MS. Markov decision processes: a tool for sequential decision making under uncertainty. *Med Decis Making* 2010; 30: 474-83.
 42. Harbias A, Salmo E, Crump A. Implications of observer variation in Gleason scoring of prostate cancer on clinical management: a collaborative audit. *Gulf J Oncolog* 2017; 1: 41-5.
 43. Ozkan TA, Erucar AT, Cebeci OO, Memik O, Ozcan L, Kusonmaz I. Interobserver variability in Gleason histological grading of prostate cancer. *Scand J Urol* 2016; 50: 420-4.
 44. Janowczyk A, Madabhushi A. Deep learning for digital pathology image analysis: a comprehensive tutorial with selected use cases. *J Pathol Inform* 2016; 7: 29.
 45. Komura D, Ishikawa S. Machine learning methods for histopathological image analysis. *Comput Struct Biotechnol J* 2018; 16: 34-42.
 46. Garud H, Karri SP, Sheet D, *et al.* High-magnification multi-views based classification of breast fine needle aspiration cytology cell samples using fusion of decisions from deep convolutional networks. In: *Proceedings of the IEEE Conference on Computer Vision and Pattern Recognition, 2017 Jul 21-26, Honolulu, HI, USA*. New York: Institute of Electrical and Electronics Engineers, 2017; 828-33.
 47. Li Y, Ping W. Cancer metastasis detection with neural conditional random field [Internet]. Ithaca: arXiv, Cornell University, 2018 [cited 2018 Nov 22]. Available from: <http://arxiv.org/abs/1806.07064>.
 48. Rannen Triki A, Blaschko MB, Jung YM, *et al.* Intraoperative margin assessment of human breast tissue in optical coherence tomography images using deep neural networks. *Comput Med Imaging Graph* 2018; 69: 21-32.
 49. Ehteshami Bejnordi B, Mullooly M, Pfeiffer RM, *et al.* Using deep convolutional neural networks to identify and classify tumor-associated stroma in diagnostic breast biopsies. *Mod Pathol* 2018; 31: 1502-12.
 50. Litjens G, Sánchez CI, Timofeeva N, *et al.* Deep learning as a tool for increased accuracy and efficiency of histopathological diagnosis. *Sci Rep* 2016; 6: 26286.
 51. Cireşan DC, Giusti A, Gambardella LM, Schmidhuber J. Mitosis detection in breast cancer histology images with deep neural networks. *Med Image Comput Comput Assist Interv* 2013; 16: 411-8.
 52. Teramoto A, Tsukamoto T, Kiriyama Y, Fujita H. Automated classification of lung cancer types from cytological images using deep convolutional neural networks. *Biomed Res Int* 2017; 2017: 4067832.
 53. Yu KH, Zhang C, Berry GJ, *et al.* Predicting non-small cell lung cancer prognosis by fully automated microscopic pathology image features. *Nat Commun* 2016; 7: 12474.
 54. Coudray N, Ocampo PS, Sakellaropoulos T, *et al.* Classification and mutation prediction from non-small cell lung cancer histopathology images using deep learning. *Nat Med* 2018; 24: 1559-67.
 55. Campanella G, Silva VW, Fuchs TJ. Terabyte-scale deep multiple instance learning for classification and localization in pathology [Internet]. Ithaca: arXiv, Cornell University, 2018 [cited 2018 Nov 22]. Available from: <http://arxiv.org/abs/1805.06983>.
 56. Arvaniti E, Fricker KS, Moret M, *et al.* Automated Gleason grading of prostate cancer tissue microarrays via deep learning. *Sci Rep* 2018; 8: 12054.
 57. Zhou N, Fedorov A, Fennessy F, Kikinis R, Gao Y. Large scale digital prostate pathology image analysis combining feature extraction and deep neural network [Internet]. Ithaca: arXiv, Cornell University, 2017 [cited 2018 Nov 22]. Available from: <http://arxiv.org/abs/1705.02678>.
 58. Nagpal K, Foote D, Liu Y, *et al.* Development and validation of a deep learning algorithm for improving Gleason scoring of prostate cancer [Internet]. Ithaca: arXiv, Cornell University, 2018 [cited 2018 Nov 22]. Available from: <http://arxiv.org/abs/1811.06497>.
 59. Ertosun MG, Rubin DL. Automated grading of gliomas using deep learning in digital pathology images: a modular approach with ensemble of convolutional neural networks. *AMIA Annu Symp Proc* 2015; 2015: 1899-908.
 60. Mobadersany P, Yousefi S, Amgad M, *et al.* Predicting cancer outcomes from histology and genomics using convolutional networks. *Proc Natl Acad Sci U S A* 2018; 115: E2970-E9.
 61. Wu M, Yan C, Liu H, Liu Q. Automatic classification of ovarian cancer types from cytological images using deep convolutional neural networks. *Biosci Rep* 2018; 38: BSR20180289.
 62. Zhang L, Lu L, Noguez I, Summers RM, Liu S, Yao J. DeepPap: deep convolutional networks for cervical cell classification. *IEEE J Biomed Health Inform* 2017; 21: 1633-43.
 63. Xu M, Papageorgiou DP, Abidi SZ, Dao M, Zhao H, Karniadakis GE.

- A deep convolutional neural network for classification of red blood cells in sickle cell anemia. *PLoS Comput Biol* 2017; 13: e1005746.
64. Meier A, Nekolla K, Earle S, *et al.* End-to-end learning to predict survival in patients with gastric cancer using convolutional neural networks. *Ann Oncol* 2018; 29(Suppl 8): mdy269.075.
 65. Xie W, Noble JA, Zisserman A. Microscopy cell counting and detection with fully convolutional regression networks. *Comput Methods Biomech Biomed Eng Imaging Vis* 2016; 6: 283-92.
 66. Tuominen VJ, Ruotoistenmaki S, Viitanen A, Jumppanen M, Isola J. ImmunoRatio: a publicly available web application for quantitative image analysis of estrogen receptor (ER), progesterone receptor (PR), and Ki-67. *Breast Cancer Res* 2010; 12: R56.
 67. Meijering E. Cell segmentation: 50 years down the road [life sciences]. *IEEE Signal Process Mag* 2012; 29: 140-5.
 68. Ruifrok AC, Johnston DA. Quantification of histochemical staining by color deconvolution. *Anal Quant Cytol Histol* 2001; 23: 291-9.
 69. Otsu N. A threshold selection method from gray-level histograms. *IEEE Trans Syst Man Cybern* 1979; 9: 62-6.
 70. Zhang L, Sonka M, Lu L, Summers RM, Yao J. Combining fully convolutional networks and graph-based approach for automated segmentation of cervical cell nuclei. In: 2017 IEEE 14th International Symposium on Biomedical Imaging (ISBI 2017), 2017 Apr 18-21, Melbourne, VIC, Australia. New York: Institute of Electrical and Electronics Engineers, 2017; 406-9.
 71. Chen H, Qi X, Yu L, Heng PA. DCAN: deep contour-aware networks for accurate gland segmentation. In: Proceedings of the IEEE Conference on Computer Vision and Pattern Recognition, 2016 Jun 27-30, Las Vegas, NV, USA. New York: Institute of Electrical and Electronics Engineers, 2016; 2487-96.
 72. CAMELYON16 Consortium. CAMELYON16. CAMELYON16 ISBI challenge on cancer metastasis detection in lymph node, 2015 [Internet]. Grand-Challenges, 2016 [cited 2018 Nov 22]. Available from: <https://camelyon16.grand-challenge.org/>.
 73. The Cancer Genome Atlas [Internet]. Bethesda: The Cancer Genome Atlas, National Cancer Institute, 2011 [cited 2018 Nov 22]. Available from: <https://cancergenome.nih.gov/>.

Prognostic Role of S100A8 and S100A9 Protein Expressions in Non-small Cell Carcinoma of the Lung

Hyun Min Koh¹ · Hyo Jung An¹
Gyung Hyuck Ko^{2,3,4}
Jeong Hee Lee^{2,3,4} · Jong Sil Lee^{2,3,4}
Dong Chul Kim^{2,3,4} · Jung Wook Yang⁴
Min Hye Kim⁴ · Sung Hwan Kim^{2,3,5}
Kyung Nyeo Jeon^{2,3,6}
Gyeong-Won Lee^{2,3,7} · Se Min Jang⁸
Dae Hyun Song^{1,2,3}

¹Department of Pathology, Gyeongsang National University Changwon Hospital, Changwon;
²Gyeongsang National University School of Medicine, Jinju; ³Gyeongsang Institute of Health Science, Jinju; ⁴Department of Pathology, Gyeongsang National University Hospital, Jinju; Departments of ⁵Thoracic and Cardiovascular Surgery and ⁶Radiology, Gyeongsang National University Changwon Hospital, Changwon; ⁷Department of Internal Medicine, Gyeongsang National University Hospital, Jinju; ⁸Department of Pathology, Konyang University Hospital, Daejeon, Korea

Received: May 15, 2018
Revised: November 7, 2018
Accepted: November 12, 2018

Corresponding Author

Dae Hyun Song, MD, PhD
Department of Pathology, Gyeongsang National University School of Medicine, 79 Gangnam-ro, Jinju 52727, Korea
Tel: +82-55-214-3150
Fax: +82-55-214-3174
E-mail: golgy@hanmail.net

Background: S100A8 and S100A9 have been gaining recognition for modulating tumor growth and metastasis. This study aimed at evaluating the clinical significance of S100A8 and S100A9 in non-small cell lung cancer (NSCLC). **Methods:** We analyzed the relationship between S100A8 and S100A9 expressions, clinicopathological characteristics, and prognostic significance in tumor cells and peritumoral inflammatory cells. **Results:** The positive staining of S100A8 in tumor cells was significantly increased in male ($p < .001$), smoker ($p = .034$), surgical method other than lobectomy ($p = .024$), squamous cell carcinoma (SQCC) ($p < .001$) and higher TNM stage ($p = .022$) compared with female, non-smoker, lobectomy, adenocarcinoma (ADC), and lower stage. The proportion of tumor cells stained for S100A8 was related to histologic type ($p < .001$) and patient sex ($p = .027$). The proportion of inflammatory cells stained for S100A8 was correlated with patient age ($p = .022$), whereas the proportion of inflammatory cells stained for S100A9 was correlated with patient sex ($p < .001$) and smoking history ($p = .031$). Moreover, positive staining in tumor cells, more than 50% of the tumor cells stained and less than 30% of the inflammatory cells stained for S100A8 and S100A9 suggested a tendency towards increased survivability in SQCC but towards decreased survivability in ADC. **Conclusions:** S100A8 and S100A9 expressions might be potential prognostic markers in patients with NSCLC.

Key Words: S100A8; S100A9; Carcinoma, non-small cell lung; Prognosis

Lung cancer is a leading cause of cancer-related morbidity and mortality worldwide.¹ Non-small cell lung cancer (NSCLC) accounts for more than 85% of all lung cancers and majority of them are suffering from NSCLC at an advanced stage.² Despite the discovery of molecular mutations and advances in diagnosis and treatment, the prognosis for patients with NSCLC remains poor, and a considerable number of patients experience recurrence.¹ Therefore, discovery of new biomarkers aiding in early detection and accurate prediction of tumor behavior could

improve patient survival rate.³

S100 proteins are a calcium-binding protein family with at least twenty members.⁴ They have a variety of intracellular and extracellular functions, such as calcium homeostasis, regulation of enzyme activity, protein phosphorylation, cytoskeletal components, transcriptional factors, and chemo-attraction for leukocytes, and macrophage attraction.^{4,5} In addition to their physiological functions, it has been demonstrated that the expression levels of S100 proteins increase in many diseases, including

cancers.⁴ Recent clinical and experimental data have suggested that changes in the expression and/or function of S100 proteins may represent a key step during cancer development.⁶ Moreover, genomic rearrangements at the chromosomal region 1q21, where most of the S100 genes are clustered, were frequently observed in human epithelial tumors, e.g., the lung, breast, esophagus, colorectal, and liver, as well as in tumors of soft tissue and bone.⁶

S100A8 (calgranulin A) and S100A9 (calgranulin B) are members of the S100 protein family, and have been reported to be overexpressed in various kinds of cancers.⁶ Previous studies have suggested that S100A8 and S100A9 play key roles in modulation of inflammation and immune response, which is conducive to genesis of almost all tumors.⁷ And several studies demonstrated that S100A8 and S100A9 promote tumor cell proliferation and invasion, and enhance metastatic process, establishing pre-metastatic niches.⁸⁻¹⁰ Moreover, some authors reported that gene expression profiling of lung tissue at exosome induced pre-metastatic niches that revealed up-regulation of genes involved in extracellular matrix remodeling and inflammation, effectors of pre-metastatic niche formation such as S100A8 and S100A9.¹¹⁻¹³ However, little is known about the expressions and prognostic significance of S100A8 and S100A9 in lung cancer.

In this study, we aimed to evaluate the expressions of S100A8 and S100A9 and the relationship between S100A8 and S100A9 expressions, clinicopathological characteristics, and prognostic significance in NSCLC. We also analyzed to compare S100A8 and S100A9 expression between peritumoral inflammatory cells and tumor cells.

MATERIALS AND METHODS

Patients and clinicopathological data

Samples from 148 patients who underwent surgical resection for NSCLC between January, 2002 and December, 2009 at Gyeongsang National University Hospital (Jinju, Korea) were examined by two pathologists. Stages were determined according to the guidelines in the American Joint Committee on Cancer Tumor Node Metastasis (TNM) Classification of Malignant Tumors, seventh edition. The histologic type and differentiation grade of the tumors were determined using the classification system of the World Health Organization, fourth edition. Clinical data and survival data were collected through medical record examination and National Statistical Office (Seoul, Korea) records.¹⁴ Disease-free survival (DFS) was defined as the period from the date of surgery to the date of cancer recurrence, and disease-specific survival (DSS) was defined as from the date of surgery to the

date of death, which was mostly due to NSCLC.¹⁵ Smoking history was defined as non-smokers (< 100 lifetime cigarettes) or smokers including current smokers and ex-smokers. This study was approved by the Institutional Review Board of Gyeongsang National University Hospital with a waiver of informed consent (2017-03-027).

Tissue microarray construction

Hematoxylin and eosin-stained slides were reviewed and the most representative tumor area was marked based on its major differentiation and location near the invasive front on formalin-fixed, paraffin-embedded tissue blocks.¹⁴ A core sized 3 mm in diameter was obtained from each case. In total, five tissue microarray (TMA) blocks were constructed with 30 cores in each block.

Immunohistochemistry

Immunohistochemistry was performed on 4 µm thick sections from TMA blocks. Tissues were stained with monoclonal anti-S100A8 antibody at a dilution of 1:500 (EPR3554, Abcam, Cambridge, UK) and monoclonal anti-S100A9 antibody at a dilution of 1:250 (EPR3555, Abcam) using an automated immunostainer (Benchmark Ultra, Ventana Medical Systems Inc., Tucson, AZ, USA). Lymphoid cells in tonsil served as positive control for S100A8 and S100A9. The primary antibody was omitted for negative control.

S100A8 and S100A9 expressions

Immunohistochemical staining for S100A8 and S100A9 were evaluated in each TMA sample by visual counting of the tumor cells and peritumoral inflammatory cells that were defined as tumor infiltrating immune cells (Fig. 1). The staining result of tumor cells for S100A8 and S100A9 was determined as negative (not stained) or positive (stained). The proportion of tumor cells stained for S100A8 and S100A9 was categorized as less than 50% or more than 50%.^{16,17} We also assessed the proportion of inflammatory cells stained for S100A8 and S100A9 classified as following: less than 30% or more than 30%. To confirm reproducibility, all samples were scored by two independent pathologists in a blind manner. If discrepancies occurred, a consensus score was reached.

Statistical analysis

The relationship between categorical variables was determined using chi-square test. The prognostic significance of various clinicopathological characteristics for DFS and DSS was assessed by the Cox proportional hazard regression method. DFS and

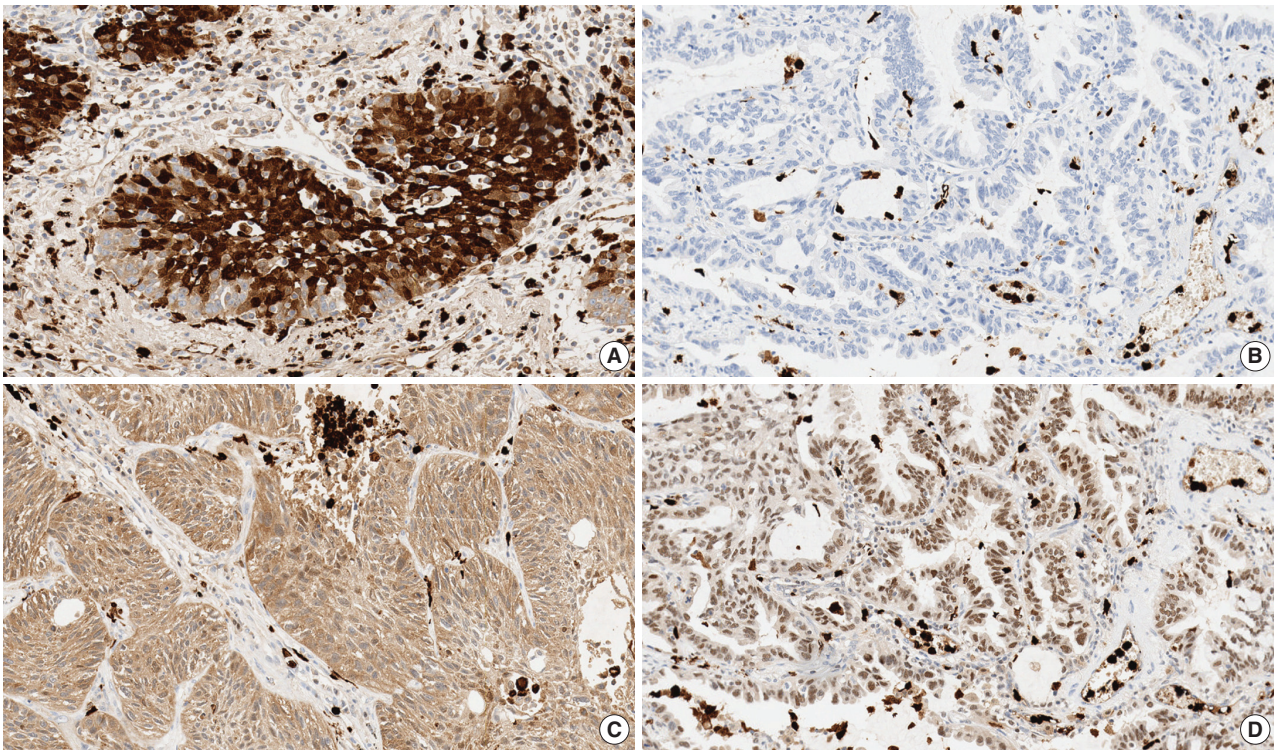


Fig. 1. S100A8 and S100A9 expressions in non-small cell lung cancer. Tumor cells and inflammatory cells stained for S100A8 in squamous cell carcinoma (A), inflammatory cells stained for S100A8 in adenocarcinoma (B), tumor cells and inflammatory cells stained for S100A9 in squamous cell carcinoma (C), tumor cells and inflammatory cells stained for S100A9 in adenocarcinoma (D).

DSS were analyzed using the Kaplan-Meier method with log-rank test between the groups. $p < .05$ was considered as statistically significant. The analysis was performed using IBM SPSS ver. 25.0 (IBM Corp., Armonk, NY, USA).

RESULTS

Patient characteristics

Clinicopathological information of the patients is shown in Table 1. The mean age of the patients was 64.85 years (range, 31 to 77 years). Histologic types of the tumor were as follows: squamous cell carcinoma (SQCC) in 96 (64.9%), adenocarcinoma (ADC) in 37 (25%), large cell neuroendocrine carcinoma in eight (5.4%), and others including pleomorphic and mucoepidermoid carcinoma in seven (4.7%). The most prevalent histologic feature of SQCC was moderately differentiated in 59 (61.4%) and ADC was acinar type in 15 (40.5%). As for the TNM stage, 83 (56.1%) were stage I, 51 (34.5%) were stage II, 12 (8.1%) were stage III, and two (1.3%) were stage IV. Of all the recruited patients, 130 patients (87.9%) underwent lobectomy including all ADC cases, while the remaining 18 patients (12.1%) underwent pneumonectomy, bilobectomy, or sleeve lobectomy.

Relationship between S100A8 and S100A9 expressions and clinicopathological characteristics in tumor cells

The relationship between S100A8 and S100A9 expression and clinicopathological characteristics in tumor cells is shown in Table 2. Positive staining for S100A8 was significantly increased in male ($p < .001$), smoker ($p = .034$), surgical methods other than lobectomy such as bilobectomy or sleeve lobectomy and pneumonectomy ($p = .024$), SQCC ($p < .001$) and higher TNM stage ($p = .022$) compared with female, non-smoker, lobectomy, ADC and lower stage. The association between positive staining for S100A8 and surgical method was derived from SQCC cases because lobectomy was done for all ADC cases. The proportion of tumor cells stained for S100A8 showed significant association with histologic type ($p < .001$) and patient sex ($p = .027$). However, positive staining for S100A9 and proportion of tumor cells stained for S100A9 did not show any significant correlation with clinicopathological characteristics.

Relationship between proportion of inflammatory cells stained for S100A8 and S100A9 and clinicopathological characteristics

The relationship between proportion of inflammatory cells

Table 1. Clinicopathological characteristics of the patients

Characteristic	No. (%) (n=148)
Mean age (yr)	64.85
Male sex	125 (84.5)
Smoking history	97 (65.5)
Surgical procedure	
Lobectomy	130 (87.9)
Bilobectomy or sleeve lobectomy	3 (2)
Pneumonectomy	15 (10.1)
Histologic type	
Squamous cell carcinoma	96 (64.9)
Well-differentiated	15
Moderately-differentiated	59
Poorly-differentiated	22
Adenocarcinoma	37 (25)
Acinar	15
Solid	6
Papillary	8
Micropapillary	3
Lepidic	3
Mucinous	2
Large cell neuroendocrine carcinoma	8 (5.4)
Others	7 (4.7)
Tumor-node-metastasis stage	
Ia	35 (23.6)
Ib	48 (32.4)
IIa	11 (7.4)
IIb	40 (27.0)
IIIa	4 (2.7)
IIIb	8 (5.4)
IV	2 (1.4)
Median survival (mo)	37
Five-year survival rate	33 (22.3)

stained for S100A8 and S100A9 and clinicopathological characteristics is shown in Table 3. The proportion of inflammatory cells stained for S100A8 was significantly correlated with patient age ($p = .022$) but not with other factors, and the proportion of inflammatory cells stained for S100A9 showed significant correlation with patient sex ($p < .001$) and smoking history ($p = .031$).

Relationship between S100A8 and S100A9 expressions in tumor cells and inflammatory cells

The relationship between S100A8 and S100A9 expressions in tumor cells and inflammatory cells is shown in Table 4. In tumor cells, the positivity of S100A8 and S100A9 significantly correlated with the proportion of tumor cells stained for each protein ($p < .001$). The positivity and proportion of tumor cells stained for S100A8 showed significant association with positivity of S100A9 ($p < .001$), and the proportion of tumor cells stained for S100A8 showed significant correlation with the proportion of tumor cells stained for S100A9 ($p < .001$). In inflammatory

cells, the proportion of inflammatory cells stained for S100A8 showed significant correlation with that of inflammatory cells stained for S100A9 ($p < .001$). In addition, the positivity of S100A8 and S100A9 in tumor cells was significantly correlated with the proportion of inflammatory cells stained for S100A9 ($p = .031$ and $p = .010$, respectively).

S100A8 and S100A9 expressions and survival analysis

The mean follow-up time of the patients in this study was 113 months. In total, 48.6% of the patients ($n=72$) had recurrence and 41.9% ($n=62$) died. The median DSS time was 37 months. The recurrence rate and survival rate had no significant differences between any groups, such as the staining result of tumor cells, proportion of tumor cells and inflammatory cells stained for S100A8 and S100A9 in NSCLC.

In SQCC, 54.2% of the patients ($n = 52$) had recurred and 46.9% ($n = 45$) died. DSS rate was significantly higher in the group in which more than 50% of the tumor cells were stained for S100A9 ($n = 36$, 62.1%) compared with the group in which less than 50% of the tumor cells were stained ($n = 15$, 39.5%) ($p = .030$). Indeed, Kaplan Meier analysis confirmed that more than 50% of the tumor cells stained for S100A9 were significantly associated with a favorable DSS ($p = .016$). Moreover, a multivariate Cox proportional hazards regression model demonstrated that more than 50% of the tumor cells stained for S100A9 represent an independent factor for good DSS (hazard ratio, 0.483; 95% confidence interval, 0.265 to 0.880; $p = .017$) (Table 5). But DFS and DSS rates did not show statistical differences between the groups with staining results of the tumor cells and the proportion of inflammatory cells stained for S100A8 and S100A9. However, the groups with positive staining in tumor cells for S100A8 and S100A9 and the group with more than 50% of the tumor cells stained for S100A8 did show a tendency towards increased DFS and DSS rates compared with the groups showing negative staining or less than 50% of the tumor cells stained. Also, groups showing less than 30% of the inflammatory cells stained for S100A8 and S100A9 revealed an increasing trend of better prognosis compared with groups showing more than 30% stained (Fig. 2A–F).

In ADC, 32.4% of the patients ($n = 12$) had recurrence and 21.6% ($n = 8$) died. The DFS and DSS rates had no significant differences between any groups, such as staining result of the tumor cells, the proportion of tumor cells and inflammatory cells stained for S100A8 and S100A9. However, the groups with positive staining in tumor cells and groups with more than 50% of the tumor cells stained for S100A8 and S100A9 did show a

Table 2. Relationship between S100A8 and S100A9 expressions and clinicopathological characteristics in tumor cells

	S100A8 expression					S100A9 expression						
	Staining result of tumor cells		Proportion of tumor cells stained			Staining result of tumor cells		Proportion of tumor cells stained				
	Negative	Positive	p-value	≤50%	>50%	p-value	Negative	Positive	p-value	≤50%	>50%	p-value
Age (yr)			.645			.237			.334			.090
<65	20 (32.8)	41 (67.2)		48 (77.4)	14 (22.6)		6 (9.8)	55 (90.2)		31 (50.0)	31 (50.0)	
≥65	31 (36.5)	54 (63.5)		59 (68.6)	27 (31.4)		13 (15.3)	72 (84.7)		31 (36)	55 (64)	
Sex			<.001			.027			.434			.867
Male	35 (28.2)	89 (71.8)		86 (68.8)	39 (31.2)		15 (12.1)	109 (87.9)		52 (41.6)	73 (58.4)	
Female	16 (72.7)	6 (27.3)		21 (91.3)	2 (8.7)		4 (18.2)	18 (81.8)		10 (43.5)	13 (56.5)	
Smoking			.034			.450			.816			.500
Non-smoker	23 (46)	27 (54)		38 (76)	12 (24)		7 (14)	43 (86)		23 (46)	27 (54)	
Smoker	27 (28.4)	68 (71.6)		68 (70.1)	29 (29.9)		12 (12.6)	83 (87.4)		39 (40.2)	58 (59.8)	
Surgery			.024			.090			.315			.783
Lobectomy	49 (38.3)	79 (61.7)		97 (74.6)	33 (25.4)		18 (14.1)	110 (85.9)		55 (42.3)	75 (57.7)	
Others ^a	2 (11.1)	16 (88.9)		10 (55.6)	8 (44.4)		1 (5.6)	17 (94.4)		7 (38.9)	11 (61.1)	
Histologic type			<.001			<.001			.060			.100
SQCC	22 (23.4)	72 (76.6)		62 (64.6)	34 (35.4)		9 (9.6)	85 (90.4)		38 (39.6)	58 (60.4)	
ADC	26 (70.3)	11 (29.7)		36 (97.3)	1 (12.5)		7 (18.9)	30 (81.1)		17 (45.9)	20 (54.1)	
LCN	3 (37.5)	5 (62.5)		7 (87.5)	1 (12.5)		3 (37.5)	5 (62.5)		6 (75)	2 (25)	
Others	0	7 (100)		2 (28.6)	5 (71.4)		0	7 (100)		1 (14.3)	6 (85.7)	
TNM stage			.022			.356			.503			.977
Ia	19 (57.6)	14 (42.4)		30 (85.7)	5 (14.3)		6 (18.2)	27 (81.8)		14 (40.0)	21 (60.0)	
Ib	13 (27.1)	35 (72.9)		32 (66.7)	16 (33.3)		7 (14.6)	41 (85.4)		22 (45.8)	26 (54.2)	
Ila	4 (36.4)	7 (63.6)		9 (81.8)	2 (18.2)		2 (18.2)	9 (81.8)		4 (36.4)	7 (63.6)	
Ilb	10 (25.0)	30 (75.0)		26 (65.0)	14 (35.0)		2 (5.0)	38 (95.0)		15 (37.5)	25 (62.5)	
IIla	1 (25.0)	3 (75.0)		3 (75.0)	1 (25.0)		0	4 (100)		2 (50.0)	2 (50.0)	
IIlb	2 (25.0)	6 (75.0)		5 (62.5)	3 (37.5)		2 (25.0)	6 (75.0)		4 (50.0)	4 (50.0)	
IV	2 (100)	0		2 (100)	0		0	2 (100)		1 (50.0)	1 (50.0)	

Values are presented as number (%).

Specimens of two patients were not informative for staining result of tumor cells in S100A8 and S100A9 expressions, due to loss of the specimen.

SQCC, squamous cell carcinoma; ADC, adenocarcinoma; LCN, large cell neuroendocrine carcinoma; TNM, tumor-node-metastasis.

^aOthers include bilobectomy or sleeve lobectomy and pneumonectomy.

tendency towards decreased DFS and DSS rates compared with groups with negative staining and less than 50% of the tumor cells stained. Also, groups with less than 30% of the inflammatory cells stained for S100A8 and S100A9 revealed a trend towards worse prognosis compared with groups with more than 30% stained (Fig. 3A–F).

DISCUSSION

S100A8 (MRP8, myeloid-related proteins 8) and S100A9 (MRP9) were originally discovered in myeloid cells.⁸ High levels of S100A8 and S100A9 expressions are characteristic of inflammatory conditions, acting as chemotactic molecules that are constitutively expressed by neutrophils, activated monocytes, macrophages, and myeloid-derived suppressor cells-derived exosomes.⁹ S100A8 and S100A9 are often co-expressed and typically function as a S100A8/A9 heterodimer (calprotectin).⁹ Due to their abundance in inflammatory cells, the main functions

of S100A8 or S100A9 have been attributed to their roles in inflammatory diseases.⁹

However, the important roles of S100A8 and S100A9 have been increasingly recognized in modulation of tumor growth and metastasis.¹⁰ Several studies have indicated that S100A8 and S100A9 promote tumor cell proliferation and invasion via activation of various intracellular signaling pathways, including phosphorylation of mitogen-activated protein kinase in tumor cells and promoting activation of nuclear factor kb; they also enhance metastatic process by mediating pre-metastatic niches as chemo-attractants and decreasing matrix metalloproteinases.^{5,10-12} Moreover, S100A8 and S100A9 are upregulated in various human cancers such as lung, prostate, colon, gastric, breast, and skin cancer, with abundant expression in neoplastic tumor cells as well as infiltrating immune cells surrounding the tumor.^{5,13}

There are only a limited number of studies investigating expressions of S100A8 and S100A9 in lung cancer. In the study by Su *et al.*,¹⁸ up-regulation of these proteins was found in ADC

Table 3. Relationship between proportion of inflammatory cells stained for S100A8 and S100A9 and clinicopathological characteristics

	Proportion of inflammatory cells stained for S100A8			Proportion of inflammatory cells stained for S100A9		
	≤30%	>30%	p-value	≤30%	>30%	p-value
Age (yr)			.022			.803
<65	4 (6.5)	58 (93.5)		5 (8.1)	57 (91.9)	
≥65	17 (19.8)	69 (80.2)		6 (7)	80 (93)	
Sex			.075			<.001
Male	15 (12)	110 (88)		5 (4)	120 (96)	
Female	6 (26.1)	17 (73.9)		6 (26.1)	17 (73.9)	
Smoking			.356			.031
Non-smoker	9 (18)	41 (82)		7 (14)	43 (86)	
Smoker	12 (12.4)	85 (87.6)		4 (4.1)	93 (95.9)	
Surgery			.748			.526
Lobectomy	18 (13.8)	112 (86.2)		9 (6.9)	121 (93.1)	
Others ^a	3 (16.7)	15 (83.3)		2 (11.1)	16 (88.9)	
Histologic type			.283			.109
SQCC	17 (17.7)	79 (82.3)		5 (5.2)	91 (94.8)	
ADC	4 (10.8)	33 (89.2)		6 (16.2)	31 (83.8)	
LCN	0	8 (100)		0	8 (100)	
Others	0	7 (100)		0	7 (100)	
TNM stage			.411			.163
Ia	2 (5.7)	33 (94.3)		1 (2.9)	34 (97.1)	
Ib	7 (14.6)	41 (85.4)		4 (8.3)	44 (91.7)	
IIa	2 (18.2)	9 (81.8)		2 (18.2)	9 (81.8)	
IIb	8 (20.0)	32 (80.0)		3 (7.5)	37 (92.5)	
IIIa	0	4 (100)		0	4 (100)	
IIIb	1 (12.5)	7 (87.5)		0	8 (100)	
IV	1 (50.0)	1 (50.0)		1 (50.0)	1 (50.0)	

Values are presented as number (%).

SQCC, squamous cell carcinoma; ADC, adenocarcinoma; LCN, large cell neuroendocrine carcinoma; TNM, tumor-node-metastasis.

^aOthers include bilobectomy or sleeve lobectomy and pneumonectomy.

Table 4. The p-values of chi-square tests between S100A8 and S100A9 expressions in tumor cells and inflammatory cells

	Tumor cells				Inflammatory cells	
	S100A8		S100A9		S100A8	S100A9
	Positivity	Proportion	Positivity	Proportion	Proportion	Proportion
Tumor cells						
S100A8						
Positivity	-	<.001	<.001	.054	.050	.031
Proportion	<.001	-	<.001	<.001	.287	.083
S100A9						
Positivity	<.001	<.001	-	<.001	.075	.010
Proportion	.054	<.001	<.001	-	.620	.436
Inflammatory cells						
Proportion for S100A8	.050	.287	.075	.620	-	<.001
Proportion for S100A9	.031	.083	.010	.436	<.001	-

that correlated with the clinical characteristics of ADC, inflammation, and stage IV lesions. Arai *et al.*¹⁹ reported that the expression level of S100A9 in pulmonary ADC showed a high correlation with poorly differentiated carcinomas, and Huang *et al.*²⁰ exhibited that positive expressions of S100A8 and S100A9 in NSCLC were significantly higher in poorly differentiated tumors

compared with moderately- and well-differentiated tumors.

In this study, we found that positive staining of tumor cells for S100A8 correlated significantly with patient sex, smoking history, surgical method, histologic type and TNM stage and the proportion of tumor cells stained for S100A8 was significantly related to the histologic type and patient sex in NSCLC. We also

Table 5. Cox proportional hazards regression model of disease-free and disease-specific survival for NSCLC patients (n = 133)

Variable	Squamous cell carcinoma				Adenocarcinoma			
	DFS		DSS		DFS		DSS	
	HR (95% CI)	p-value	HR (95% CI)	p-value	HR (95% CI)	p-value	HR (95% CI)	p-value
Univariate analysis								
Age (< 65 yr vs ≥ 65 yr)	1.402 (0.784–2.506)	.247	1.170 (0.635–2.157)	.614	0.934 (0.296–2.945)	.934	0.818 (0.195–3.428)	.784
Sex (male vs female)	0.824 (0.200–3.391)	.789	0.398 (0.055–2.895)	.363	0.736 (0.234–2.320)	.601	0.592 (0.141–2.484)	.474
Smoking history (nonsmoker vs smoker)	0.644 (0.356–1.164)	.145	0.671 (0.355–1.266)	.218	0.918 (0.269–3.139)	.892	1.690 (0.422–6.764)	.459
Surgical method (lobectomy vs others ^a)	1.562 (0.814–2.998)	.180	1.479 (0.730–2.996)	.278	NA ^b		NA ^b	
TNM stage (< IIb vs ≥ IIb)	1.711 (0.984–2.975)	.057	1.966 (1.087–3.558)	.025	2.727 (0.867–8.571)	.086	2.961 (0.738–11.871)	.126
Proportion of tumor cells stained for S100A9 (≤ 50% vs > 50%)	0.709 (0.408–1.231)	.222	0.491 (0.272–0.889)	.019	1.625 (0.475–5.557)	.439	2.891 (0.583–14.337)	.194
Multivariate analysis								
Age (< 65 yr vs ≥ 65 yr)	-	-	-	-	-	-	-	-
Sex (male vs female)	-	-	-	-	-	-	-	-
Smoking history (nonsmoker vs smoker)	-	-	-	-	-	-	-	-
Surgical method (lobectomy vs others ^a)	-	-	-	-	-	-	-	-
TNM stage (< IIb vs ≥ IIb)	1.736 (0.998–3.022)	.051	2.012 (1.110–3.644)	.021	2.577 (0.805–8.253)	.111	2.528 (0.618–10.336)	.197
Proportion of tumor cells stained for S100A9 (≤ 50% vs > 50%)	0.702 (0.402–1.224)	.212	0.483 (0.265–0.880)	.017	1.374 (0.393–4.807)	.619	2.457 (0.484–12.484)	.278

NSCLC, non-small cell lung cancer; DFS, disease-free survival; DSS, disease-specific survival; HR, hazard ratio; CI, confidence interval; NA, not applicable; TNM, tumor-node-metastasis.

^aOthers include bilobectomy or sleeve lobectomy and pneumonectomy; ^bAll of the adenocarcinoma cases underwent lobectomy.

observed that the proportion of inflammatory cells stained for S100A8 was significantly related to the patient age, and that of S100A9 showed significant correlation with patient sex and smoking history in NSCLC. In addition, positivity of tumor cells and/or proportion of tumor cells stained for S100A8 and S100A9 significantly correlated with positivity of tumor cells and/or proportion of inflammatory cells stained for S100A8 and/or S100A9 in NSCLC, indicating that inflammation is closely associated with cancer.²¹ Moreover, we analyzed that DSS rate was significantly higher in the group with more than 50% of the tumor cells stained for S100A9 compared with the group with less than 50% stained in SQCC, confirmed by Kaplan–Meier analysis and the multivariate Cox proportional hazards regression model.

Another interesting finding of this study is that the groups with positive staining in tumor cells, the groups with more than 50% of the tumor cells stained and the groups with less than 30% of the inflammatory cells stained for S100A8 and S100A9 showed a tendency towards increased DFS and DSS rates in SQCC but towards decreased rates in ADC.

The present study is the first evaluate the expressions of S100A8 and S100A9 in NSCLC and their prognostic significance.

In SQCC, several studies have demonstrated that high expres-

sion of S100A8 and/or S100A9 could be a favorable factor while showing frequent loss or reduction of the protein expressions in the head and neck, esophagus and cervix.^{22–25} There are a few studies reporting that S100A8 and S100A9 are related to the regulation of keratinocyte proliferation and differentiation.^{25,26} Our results also reveal that positive staining for S100A8 and S100A9 may have a favorable effect on the prognosis in pulmonary SQCC.

In previous studies, strong S100A8 and S100A9 up-regulation was found in breast, gastric, colorectal, pancreatic, and prostate cancer. The altered S100A8 and/or S100A9 expressions in carcinomas of glandular cell origin, such as breast, lung, and thyroid gland, were related to poor tumor differentiation and more aggressive behavior, which is consistent with our results in ADC.^{6,17,19,27–33}

Some studies have shown that cancer-related inflammation is often considered to support malignant progression and metastasis, showing up-regulation of S100A8 and S100A9 by inflammatory cells.^{9,10,21,25} However, the same inflammatory cells also participate in anti-tumor immunity and restraint of malignant disease.³⁴ The balance between anti-tumor and pro-tumor functions can be dependent on polarization state, interaction with tumor microenvironment, and/or the tumor type.^{10,35} In the same

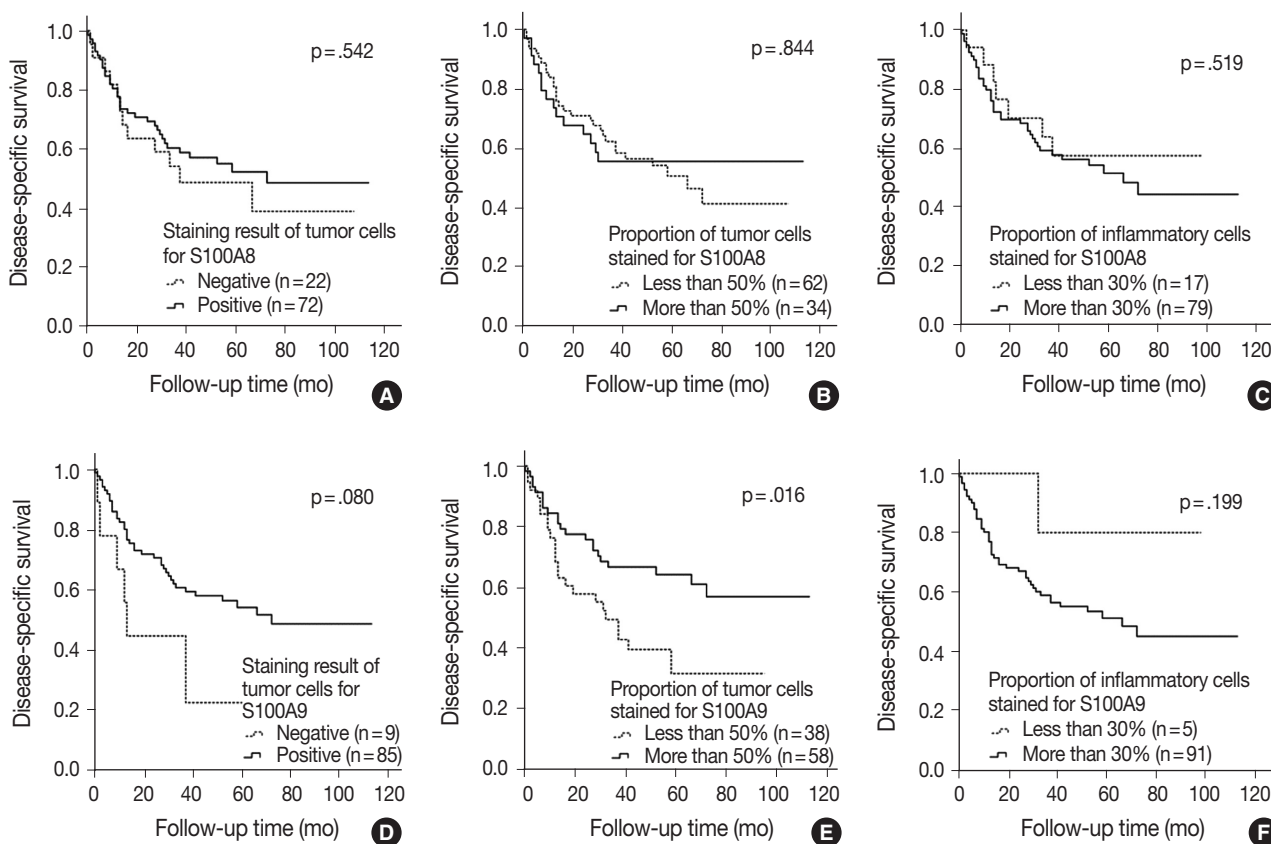


Fig. 2. Kaplan-Meier survival analysis of survival curves based on S100A8 and S100A9 expressions in patients with squamous cell carcinoma. The groups with positive staining in tumor cells (A, D), the groups with more than 50% of the tumor cells (B, E) stained and the groups with less than 30% of the inflammatory cells (C, F) stained for S100A8 and S100A9 reveal a tendency towards increased survivability compared with the groups showing negative staining, less than 50% of the tumor cells stained and more than 30% of the inflammatory cells stained.

context, our studies reveal that the proportion of inflammatory cells stained for S100A8 and S100A9 may have an influence that is quite opposite in SQCC and ADC.

There are some limitations to this study. For example, we included a TMA core per case in analysis, which could induce a lack of representativeness. In addition, we did not use an adjustment method in scoring of inflammatory cells although tumor infiltrating immune cells consist of various cells. Moreover, the number of ADC cases were small, and they were all removed by lobectomy so we could not use the variable of surgical method in Cox proportional hazards regression model. A large-scale study with an organized study design including a sufficient number of cases and tissue samples is recommended in future studies.

In summary, we have found that positive staining in tumor cells, more than 50% of the tumor cells stained and less than 30% of the inflammatory cells stained for S100A8 and S100A9 suggest a tendency towards increased survivability in SQCC, whereas positive staining in tumor cells, more than 50% of the tumor cells stained and less than 30% of the inflammatory cells

stained for S100A8 and S100A9 suggest a tendency towards decreased survivability in ADC. Consequently, S100A8 and S100A9 expressions could be potential prognostic factors in patients with NSCLC.

Many recent studies have provided evidence that implicates S100A8 and S100A9 to play important roles in cancer. However, the expressions and/or functions of S100A8 and S100A9 are much more complicated, supporting our data. Further studies are needed to fully comprehend their roles in cancer.

ORCID

Hyun Min Koh: <https://orcid.org/0000-0002-7457-7174>

Hyo Jung An: <https://orcid.org/0000-0002-2068-8370>

Gyung Hyuck Ko: <https://orcid.org/0000-0002-6721-1828>

Jeong Hee Lee: <https://orcid.org/0000-0001-5833-4773>

Jong Sil Lee: <https://orcid.org/0000-0001-9159-7575>

Dong Chul Kim: <https://orcid.org/0000-0002-9484-7792>

Jung Wook Yang: <https://orcid.org/0000-0002-9698-3667>

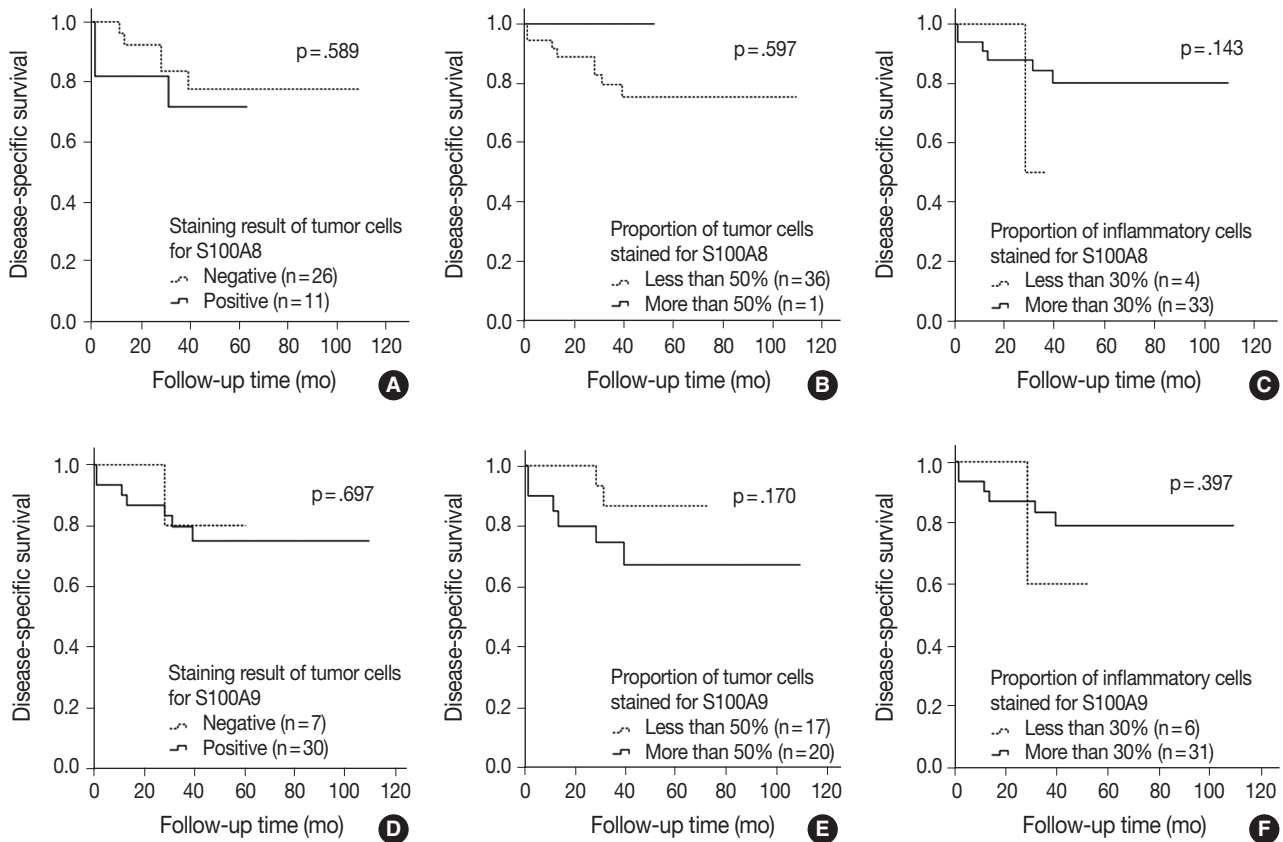


Fig. 3. Kaplan-Meier survival analysis of survival curves based on S100A8 and S100A9 expressions in patients with adenocarcinoma. The groups with positive staining in tumor cells (A, D), the groups with more than 50% of the tumor cells (B, E) stained and the groups with less than 30% of the inflammatory cells (C, F) stained for S100A8 and S100A9 reveal a trend towards decreased survivability compared with the groups showing negative staining, less than 50% of the tumor cells stained and more than 30% of the inflammatory cells stained.

Min Hye Kim: <https://orcid.org/0000-0002-8631-5104>

Sung Hwan Kim: <https://orcid.org/0000-0002-6888-774X>

Kyung Nyeo Jeon: <https://orcid.org/0000-0003-2267-0366>

Gyeong-Won Lee: <https://orcid.org/0000-0002-1781-2262>

Se Min Jang: <https://orcid.org/0000-0002-5442-3303>

Dae Hyun Song: <https://orcid.org/0000-0001-7163-0403>

Conflicts of Interest

The authors declare that they have no potential conflicts of interest.

Acknowledgments

This research was supported by the Basic Science Research Program through the National Research Foundation of Korea (NRF) funded by the Ministry of Education (2017R1C1B5014837).

REFERENCES

- Jo YM, Park TI, Lee HY, Jeong JY, Lee WK. Prognostic significance of aquaporin 5 expression in non-small cell lung cancer. *J Pathol Transl Med* 2016; 50: 122-8.
- Lee SH, Kim WS, Choi YD, *et al.* Analysis of mutations in epidermal growth factor receptor gene in Korean patients with non-small cell lung cancer: summary of a nationwide survey. *J Pathol Transl Med* 2015; 49: 481-8.
- Fan B, Zhang LH, Jia YN, *et al.* Presence of S100A9-positive inflammatory cells in cancer tissues correlates with an early stage cancer and a better prognosis in patients with gastric cancer. *BMC Cancer* 2012; 12: 316.
- Yasar O, Akcay T, Obek C, Turegun FA. Significance of S100A8, S100A9 and calprotectin levels in bladder cancer. *Scand J Clin Lab Invest* 2017; 77: 437-41.
- Salama I, Malone PS, Mihaimeed F, Jones JL. A review of the S100 proteins in cancer. *Eur J Surg Oncol* 2008; 34: 357-64.
- Gebhardt C, Nemeth J, Angel P, Hess J. S100A8 and S100A9 in inflammation and cancer. *Biochem Pharmacol* 2006; 72: 1622-31.
- Lang B, Shang C, Meng L. Targeted silencing of S100A8 gene by miR-24 to increase chemotherapy sensitivity of endometrial carcinoma.

- noma cells to paclitaxel. *Med Sci Monit* 2016; 22: 1953-8.
8. Srikrishna G. S100A8 and S100A9: new insights into their roles in malignancy. *J Innate Immun* 2012; 4: 31-40.
 9. Hiratsuka S, Watanabe A, Aburatani H, Maru Y. Tumour-mediated upregulation of chemoattractants and recruitment of myeloid cells predetermines lung metastasis. *Nat Cell Biol* 2006; 8: 1369-75.
 10. Lim SY, Yuzhalin AE, Gordon-Weeks AN, Muschel RJ. Tumor-infiltrating monocytes/macrophages promote tumor invasion and migration by upregulating S100A8 and S100A9 expression in cancer cells. *Oncogene* 2016; 35: 5735-45.
 11. Hiratsuka S, Watanabe A, Sakurai Y, *et al.* The S100A8-serum amyloid A3-TLR4 paracrine cascade establishes a pre-metastatic phase. *Nat Cell Biol* 2008; 10: 1349-55.
 12. Weidle UH, Birzele F, Kollmorgen G, Rügner R. The multiple roles of exosomes in metastasis. *Cancer Genomics Proteomics* 2017; 14: 1-15.
 13. Armstrong D, Wildman DE. Extracellular vesicles and the promise of continuous liquid biopsies. *J Pathol Transl Med* 2018; 52: 1-8.
 14. Song DH, Ko GH, Lee JH, *et al.* Myoferlin expression in non-small cell lung cancer: prognostic role and correlation with VEGFR-2 expression. *Oncol Lett* 2016; 11: 998-1006.
 15. Song DH, Ko GH, Lee JH, *et al.* Prognostic role of myoferlin expression in patients with clear cell renal cell carcinoma. *Oncotarget* 2017; 8: 89033-9.
 16. Choi DK, Li ZJ, Chang IK, *et al.* Clinicopathological roles of S100A8 and S100A9 in cutaneous squamous cell carcinoma *in vivo* and *in vitro*. *Arch Dermatol Res* 2014; 306: 489-96.
 17. Arai K, Takano S, Teratani T, Ito Y, Yamada T, Nozawa R. S100A8 and S100A9 overexpression is associated with poor pathological parameters in invasive ductal carcinoma of the breast. *Curr Cancer Drug Targets* 2008; 8: 243-52.
 18. Su YJ, Xu F, Yu JP, Yue DS, Ren XB, Wang CL. Up-regulation of the expression of S100A8 and S100A9 in lung adenocarcinoma and its correlation with inflammation and other clinical features. *Chin Med J (Engl)* 2010; 123: 2215-20.
 19. Arai K, Teratani T, Nozawa R, Yamada T. Immunohistochemical investigation of S100A9 expression in pulmonary adenocarcinoma: S100A9 expression is associated with tumor differentiation. *Oncol Rep* 2001; 8: 591-6.
 20. Huang H, Huang Q, Tang T, *et al.* Clinical significance of calcium-binding protein S100A8 and S100A9 expression in non-small cell lung cancer. *Thorac Cancer* 2018; 9: 800-4.
 21. Zhang X, Ai F, Li X, *et al.* Inflammation-induced S100A8 activates Id3 and promotes colorectal tumorigenesis. *Int J Cancer* 2015; 137: 2803-14.
 22. Zhu H, Wu TC, Chen WQ, *et al.* Roles of galectin-7 and S100A9 in cervical squamous carcinoma: clinicopathological and *in vitro* evidence. *Int J Cancer* 2013; 132: 1051-9.
 23. Roesch Ely M, Nees M, Karsai S, *et al.* Transcript and proteome analysis reveals reduced expression of calgranulins in head and neck squamous cell carcinoma. *Eur J Cell Biol* 2005; 84: 431-44.
 24. Kong JP, Ding F, Zhou CN, *et al.* Loss of myeloid-related proteins 8 and myeloid-related proteins 14 expression in human esophageal squamous cell carcinoma correlates with poor differentiation. *World J Gastroenterol* 2004; 10: 1093-7.
 25. Funk S, Mark R, Bayo P, *et al.* High S100A8 and S100A12 protein expression is a favorable prognostic factor for survival of oropharyngeal squamous cell carcinoma. *Int J Cancer* 2015; 136: 2037-46.
 26. Voss A, Bode G, Sopalla C, *et al.* Expression of S100A8/A9 in HaCaT keratinocytes alters the rate of cell proliferation and differentiation. *FEBS Lett* 2011; 585: 440-6.
 27. El-Rifai W, Moskaluk CA, Abdrabbo MK, *et al.* Gastric cancers overexpress S100A calcium-binding proteins. *Cancer Res* 2002; 62: 6823-6.
 28. Seth A, Kitching R, Landberg G, Xu J, Zubovits J, Burger AM. Gene expression profiling of ductal carcinomas *in situ* and invasive breast tumors. *Anticancer Res* 2003; 23: 2043-51.
 29. Stulík J, Osterreicher J, Koupilová K, *et al.* The analysis of S100A9 and S100A8 expression in matched sets of macroscopically normal colon mucosa and colorectal carcinoma: the S100A9 and S100A8 positive cells underlie and invade tumor mass. *Electrophoresis* 1999; 20: 1047-54.
 30. Shen J, Person MD, Zhu J, Abbruzzese JL, Li D. Protein expression profiles in pancreatic adenocarcinoma compared with normal pancreatic tissue and tissue affected by pancreatitis as detected by two-dimensional gel electrophoresis and mass spectrometry. *Cancer Res* 2004; 64: 9018-26.
 31. Hermani A, Hess J, De Servi B, *et al.* Calcium-binding proteins S100A8 and S100A9 as novel diagnostic markers in human prostate cancer. *Clin Cancer Res* 2005; 11: 5146-52.
 32. Arai K, Teratani T, Kuruto-Niwa R, Yamada T, Nozawa R. S100A9 expression in invasive ductal carcinoma of the breast: S100A9 expression in adenocarcinoma is closely associated with poor tumour differentiation. *Eur J Cancer* 2004; 40: 1179-87.
 33. Ito Y, Arai K, Ryushi, *et al.* S100A9 expression is significantly linked to dedifferentiation of thyroid carcinoma. *Pathol Res Pract* 2005; 201: 551-6.
 34. DeNardo DG, Andreu P, Coussens LM. Interactions between lymphocytes and myeloid cells regulate pro- versus anti-tumor immunity. *Cancer Metastasis Rev* 2010; 29: 309-16.
 35. Gabrilovich DI, Ostrand-Rosenberg S, Bronte V. Coordinated regulation of myeloid cells by tumours. *Nat Rev Immunol* 2012; 12: 253-68.

PLAG1, SOX10, and Myb Expression in Benign and Malignant Salivary Gland Neoplasms

Ji Hyun Lee · Hye Ju Kang
Chong Woo Yoo · Weon Seo Park
Junsun Ryu¹ · Yuh-Seog Jung¹
Sung Weon Choi² · Joo Yong Park²
Nayoung Han

Department of Pathology, National Cancer Center, Goyang; ¹Head and Neck Oncology Clinic, National Cancer Center, Goyang; ²Oral Oncology Clinic, National Cancer Center, Goyang, Korea

Received: July 24, 2018
Revised: October 10, 2018
Accepted: October 11, 2018

Corresponding Author
Nayoung Han, MD, PhD
Department of Pathology, National Cancer Center, 323 Ilsan-ro, Ilsandong-gu, Goyang 10408, Korea
Tel: +82-31-920-1756
Fax: +82-31-920-1369
E-mail: hanny@ncc.re.kr

Background: Recent findings in molecular pathology suggest that genetic translocation and/or overexpression of oncoproteins is important in salivary gland tumorigenesis and diagnosis. We investigated PLAG1, SOX10, and Myb protein expression in various salivary gland neoplasm tissues. **Methods:** A total of 113 cases of surgically resected salivary gland neoplasms at the National Cancer Center from January 2007 to March 2017 were identified. Immunohistochemical staining of PLAG1, SOX10, and Myb in tissue samples was performed using tissue microarrays. **Results:** Among the 113 cases, 82 (72.6%) were benign and 31 (27.4%) were malignant. PLAG1 showed nuclear staining and normal parotid gland was not stained. Among 48 cases of pleomorphic adenoma, 29 (60.4%) were positive for PLAG1. All other benign and malignant salivary gland neoplasms were PLAG1-negative. SOX10 showed nuclear staining. In normal salivary gland tissues SOX10 was expressed in cells of acinus and intercalated ducts. In benign tumors, SOX10 expression was observed in all pleomorphic adenoma (48/48), and basal cell adenoma (3/3), but not in other benign tumors. SOX10 positivity was observed in nine of 31 (29.0%) malignant tumors. Myb showed nuclear staining but was not detected in normal parotid glands. Four of 31 (12.9%) malignant tumors showed Myb positivity: three adenoid cystic carcinomas (AdCC) and one myoepithelial carcinoma with focal AdCC-like histology. **Conclusions:** PLAG1 expression is specific to pleomorphic adenoma. SOX10 expression is helpful to rule out excretory duct origin tumor, but its diagnostic value is relatively low. Myb is useful for diagnosing AdCC when histology is unclear in the surgical specimen.

Key Words: Salivary gland neoplasms; Immunohistochemistry; Pleomorphic adenoma gene-1; SOX transcription factors; Oncogene proteins v-Myb

Salivary gland tumors are heterogeneous tumors with many variable features including histological morphology, lineage, and biological characteristics.¹ Recently, specific fusions and overexpression of oncoproteins have been reported in some salivary gland tumors.²

Pleomorphic adenoma gene 1 (*PLAG1*) functions as an oncogene in several human tumors.³ Overexpression of *PLAG1* promotes mitogenesis, proliferation, apoptosis, and insulin-like growth factor 2 upregulation.⁴

SRY-related HMG-box 10 (*SOX10*) is known to play a crucial role in the differentiation, maturation, and maintenance of Schwann cells and melanocytes.⁵ *SOX10* is a potential marker for acinar and intercalated duct differentiation in salivary gland tumors.⁶

v-Myb is an oncogene homolog of the avian myeloblastosis virus. It acts as a DNA-binding transcription regulator and is a proto-oncogene that plays an important role in controlling proliferation and differentiation.⁷

eration and differentiation.⁷

In this study, we investigated *PLAG1*, *SOX10*, and *Myb* protein expression in human salivary gland neoplasm samples and evaluated the association between the expression profiles and histological and clinical features.

MATERIALS AND METHODS

Patients

The files of 113 patients with surgically resected primary salivary gland neoplasm who underwent operation at the National Cancer Center from January 2007 to March 2017 were obtained. Three adenoid cystic carcinoma cases reported between April 2017 and June 2018 were additionally obtained. Patient age, sex, histologic type, size, and involved site were evaluated by reviewing medical charts and pathological records. Histologic diagnosis of one case (No. 72) was discussed and revised from adenocarci-

noma, not otherwise specified (NOS) to adenoid cystic carcinoma. This study protocol was reviewed and approved by the Institutional Review Board (IRB) of the National Cancer Center (NCC2018-0182). The need for informed consent was waived by the IRB.

Tissue microarray

Tissue array blocks were prepared as described previously.⁸ Suitable areas for tissue retrieval from triplicate 2-mm-diameter cores obtained from the tumor block were marked on standard hematoxylin and eosin–stained sections, punched out from the paraffin block, and inserted into a recipient block. Sections (4- μ m-thick) were cut from each tissue array block, deparaffinized, and dehydrated. An adequate case was defined as tumor occupying more than 10% of the core area.

Immunohistochemistry

Immunohistochemistry (IHC) staining was performed using an automatic immunostainer (Ventana, Tucson, AZ, USA) according to the manufacturer's instructions. The primary antibodies used were as follows: mouse monoclonal anti-PLAG1 (clone 3B7, Novus, Littleton, CO, USA), rabbit monoclonal anti-SOX10 (clone EP268, Bio SB, Santa Barbara, CA, USA), and rabbit monoclonal anti-v-Myb+c-Myb (ab45150, Abcam, Cambridge, UK). The stroma surrounding the tumor cells preserved the normal staining pattern, thereby serving as the internal control. A case was considered positive if any of the cores were stained with any intensity.

Statistical analysis

The chi-square test or Fisher exact test (two-sided) was used to determine the correlations between parameters. Independent sample t-test (continuous variable) and chi-square/Fisher exact test (grouped variable) were conducted to determine the correlations between parameters. The results were considered significant when p-values were <0.05. Statistical analyses were conducted using the SPSS ver. 19.0 statistical software program (SPSS Inc., Chicago, IL, USA).

RESULTS

Cohort characteristics

The 113 cases of resected major and minor salivary gland neoplasms included 82 benign tumors and 31 malignant tumors. The benign tumors consisted of 48 pleomorphic adenomas (58.5%), 27 Warthin tumors (32.9%), three basal cell adenomas

(3.7%), three cystadenomas (3.7%), and one oncocytoma (1.2%). The malignant tumors consisted of six mucoepidermoid carcinomas, low grade (19.4%); three mucoepidermoid carcinomas, intermediate grade (9.7%); three mucoepidermoid carcinomas, high grade (9.7%); four salivary duct carcinomas (12.9%); three squamous cell carcinomas (9.7%); three adenoid cystic carcinomas (9.7%); two adenocarcinomas, NOS (6.5%); and one each of carcinoma ex pleomorphic adenoma (CA ex-PA), polymorphous low-grade adenocarcinoma, epithelial myoepithelial carcinoma, myoepithelial carcinoma, acinic cell carcinoma, carcinosarcoma, and poorly differentiated carcinoma.

The clinical characteristics of all 113 cases are shown in Table 1. Benign tumors typically occurred in major salivary glands (81 of 82 cases, 98.8%) whereas malignant tumors occurred in major salivary glands (18 of 31 cases, 58.1%) and minor salivary glands (13, 41.9%). The tumor size was not significantly different between malignant and benign cases. The tumor lesion was surgically completely resected in all 82 benign cases and 26 of 31 malignant cases (83.9%).

PLAG1 expression is specific for pleomorphic adenoma

Immunohistochemical staining revealed that PLAG1 protein was expressed in the nucleus (Fig. 1B). Cells in the normal salivary glands did not express PLAG1 (Fig. 1A). Among 113 cases, all 34 benign salivary gland neoplasms other than pleomorphic adenoma were PLAG1-negative. Additionally, all 31 malignant salivary gland neoplasms including one Ca ex-PA case were PLAG1-negative (Fig. 1C).

Among the 48 cases of pleomorphic adenoma, PLAG1 protein expression was observed in 29 (60.4%). Histologically, all of the tumors were composed of epithelial and myoepithelial/stromal components in a mixture of patterns. PLAG1 expression was moderately to strongly positive in myoepithelial/stromal components, regardless of its negativity and/or faint positivity in the epithelial component (Fig. 1B).

Table 1. Characteristics of 113 salivary gland neoplasms

	Benign (n=82)	Malignant (n=31)	p-value
Age (yr)	52 ± 14	56 ± 16	.165
Sex			
Male	48 (58.5)	18 (58.1)	.964
Female	34 (41.5)	13 (41.9)	
Site			
Major	81 (98.8)	18 (58.1)	< .001
Minor	1 (1.2)	13 (41.9)	
Size (cm)	2.6 ± 1.3	2.6 ± 1.4	.661

Values are presented as mean ± standard deviation or number (%).

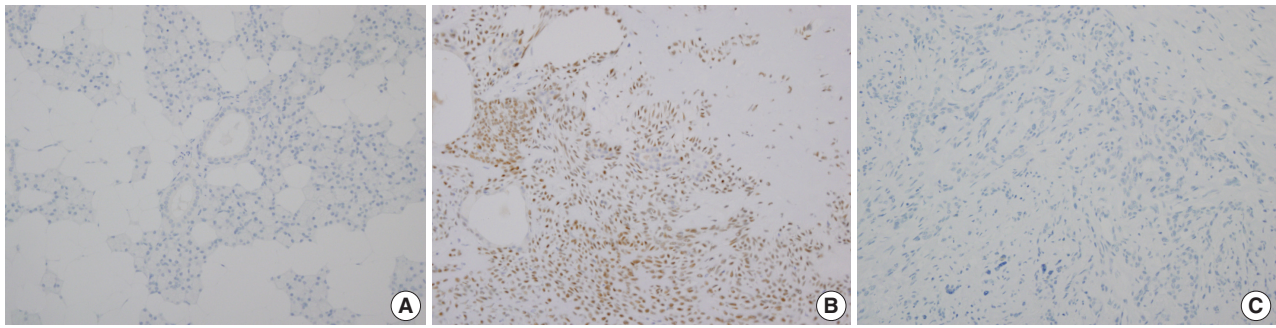


Fig. 1. Representative images of PLAG1 protein expression. (A) PLAG1 expression is not observed in the normal salivary gland parenchyme. (B) PLAG1 nuclear expression is observed in pleomorphic adenoma (myoepithelial cells). (C) PLAG1 expression is not observed in adenoid cystic carcinoma.

Table 2. Clinicopathological characteristics according to PLAG1 protein expression status in 48 pleomorphic adenoma cases

	PLAG1-negative	PLAG1-positive	p-value
Total	19 (39.6)	29 (60.4)	-
Age (yr)	48 ± 12	48 ± 16	.985
Sex			
Male	8 (40.0)	12 (60.0)	.960
Female	11 (39.3)	17 (60.7)	
Size (cm)	2.5 ± 1.0	2.6 ± 1.4	.622
Gland types			
Minor	0	1 (100)	1.000
Major	19 (40.4)	28 (59.6)	
Parotid	18 (48.6)	19 (51.4)	.034 ^a
Submandibular	1 (10.0)	9 (90.0)	

Values are presented as number (%) or mean ± standard deviation. Independent sample t-test (continuous variable) and chi-square/Fisher exact test (grouped variable) were conducted. ^aStatistically significant.

PLAG1 positivity was not associated with age, sex, or tumor size and was higher in submandibular gland pleomorphic adenomas than in parotid gland pleomorphic adenomas (90.0% vs 51.4%, respectively); however, the difference was not significant (Table 2).

The sensitivity of PLAG1 expression by IHC was found to be 60.4% (45.3%–74.2%) and specificity was 100% (94.4%–100%). The positive predictive value was 100% and negative predictive value was 77.1% (70.4%–82.7%).

SOX10 expression indicates cell of origin

SOX10 protein showed nuclear expression by IHC (Fig. 2). In normal salivary gland tissue, SOX10 staining was positive in intercalated ductal epithelial cells. Mucinous acinar cells were SOX10 negative, whereas serous acinar cells were SOX10 positive (Fig. 2A). The intensity of SOX10 nuclear staining was higher in salivary glands with atrophic change, and the intensity of staining in serous acinar cells was lower than that in interca-

lated ductal epithelial cells.

For the 82 benign salivary gland neoplasms, all 48 pleomorphic adenoma cases and all three basal cell adenoma cases were SOX10-positive. One pleomorphic adenoma showed scant positivity in most (> 50%) of the tumor cells, and we reclassified this case as SOX10-positive. All 27 Warthin tumors, one oncocytoma, and three cystadenoma cases were SOX10 negative. Although four cases of Warthin tumors also contained weakly positive tumor cells, the low proportion of positive cells (< 5%) was insufficient for reclassification.

Among the 31 malignant salivary gland neoplasms, nine (29.0%) tumors were SOX10-positive including three of three adenoid cystic carcinoma, one of one CA ex-PA, one of one epithelial-myoepithelial carcinoma, one of one myoepithelial carcinoma, one of one poorly differentiated carcinoma, and one of one polymorphous low-grade adenocarcinoma. Scant but diffuse positivity was observed in one acinic cell carcinoma, and we added this case to the SOX10-positive group. All 12 cases of mucoepidermoid carcinoma and one carcinosarcoma were SOX10-negative. Detailed results are provided in Table 3.

Myb expression is relatively common in salivary gland neoplasms

Myb expression showed nuclear and cytoplasmic staining, and the presence of nuclear staining was regarded as positive. Myb expression was not observed in the normal salivary gland parenchyme (Fig. 3A). Nuclear Myb expression was restricted to adenoid cystic carcinoma cells of myoepithelial origin (Fig. 3B).

Among the 82 benign salivary gland neoplasms, 17 cases (20.7%) were Myb-positive. Specifically, 16 of 48 pleomorphic adenomas (33.3%) and one of three basal cell adenomas (33.3%) were Myb-positive. In contrast, all 27 Warthin tumors, one oncocytoma, and three cystadenomas showed Myb negativity.

For the 31 malignant tumors with available tissue microarray,

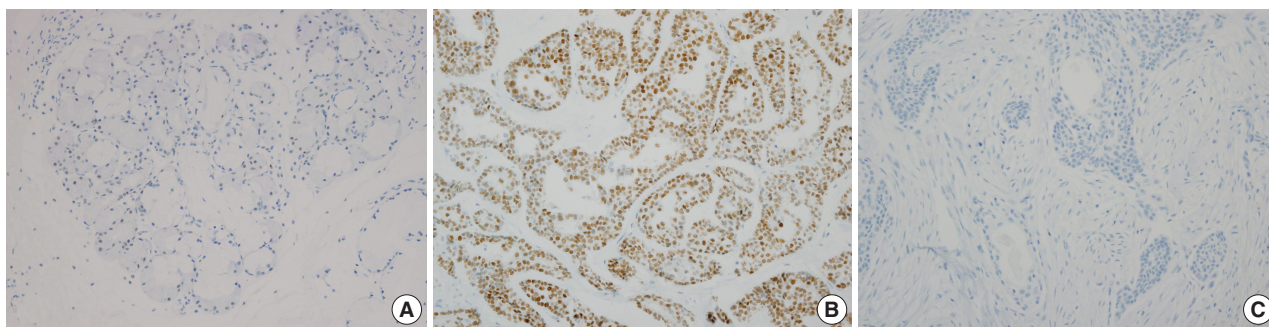


Fig. 2. Representative images of SOX10 protein expression. (A) SOX10 staining is not found in mucinous acinar cells. (B) SOX10 positivity is observed in adenoid cystic carcinoma. (C) SOX10 staining is not observed in mucoepidermoid carcinoma, low grade.

Table 3. SOX10 expression in malignant salivary gland neoplasms with different histologic types

SOX10-positive (n=9)	SOX10-negative (n=22)	Correlative normal histology
Acinic cell carcinoma (n=1)	-	Acinus
Adenoid cystic carcinoma (n=3)	-	Intercalated duct
Carcinoma ex pleomorphic adenoma (n=1)	-	Intercalated duct
Epithelial-myoeplithelial carcinoma (n=1)	-	Intercalated duct
Myoeplithelial carcinoma (n=1)	-	Intercalated duct
Polymorphous low grade adenocarcinoma (n=1)	-	Intercalated duct
	Mucoepidermoid carcinoma, high grade (n=3)	Excretory duct
	Mucoepidermoid carcinoma, intermediate grade (n=3)	Excretory duct
	Mucoepidermoid carcinoma, low grade (n=6)	Excretory duct
	Salivary duct carcinoma (n=4)	Excretory duct
	Adenocarcinoma, NOS (n=2)	NA
Poorly differentiated carcinoma (n=1)	-	NA
	Carcinosarcoma (n=1)	NA
	Squamous cell carcinoma (n=3)	NA

NOS, not otherwise specified; NA, not applicable.

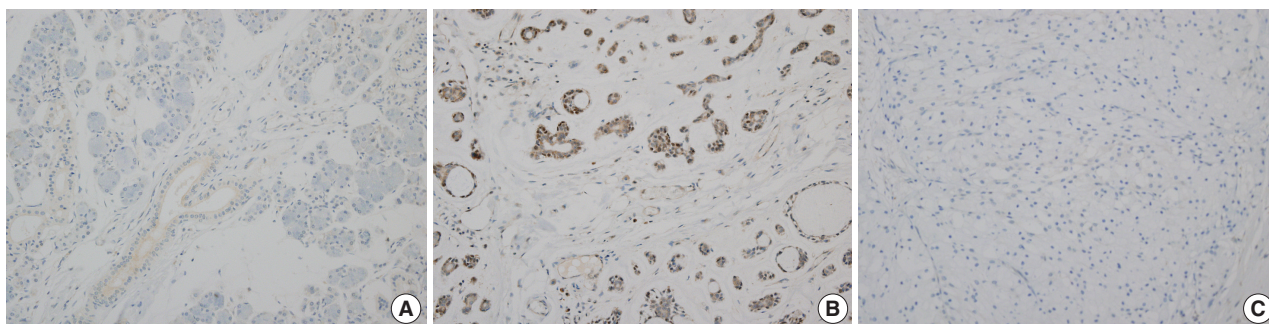


Fig. 3. Representative images of Myb protein expression. (A) Myb expression is not observed in the normal salivary gland parenchyme. (B) Myb positivity is observed in adenoid cystic carcinoma. (C) Myb protein is not observed in acinic cell carcinoma.

five tumors showed Myb positivity including all three adenoid cystic carcinomas, one myoeplithelial carcinoma, and one salivary duct carcinoma. Detailed results are provided in Table 4. All 12 cases of mucoepidermoid carcinomas, one acinic cell carcinoma, one CA ex-PA, one carcinosarcoma, one epithelial-myoeplithelial carcinoma, one poorly differentiated carcinoma, and one polymorphous low grade showed Myb negativity.

One representative paraffin tumor block ('whole section') was tested for Myb-positive cases. In three adenoid cystic carcinoma cases and one myoeplithelial carcinoma case, moderate-to-strong nuclear staining of Myb was observed in a peripheral pattern. One salivary duct carcinoma case did not show expression of Myb in whole section staining. Three additional adenoid cystic carcinoma specimens that were resected recently (less than one

Table 4. Immunohistochemical expression pattern of Myb-positive malignant salivary gland neoplasms

Case No.	Initial diagnosis	Tissue microarray			Final diagnosis
		Nucleus	Cytoplasm	No. of positive cores	
37	Adenoid cystic carcinoma (AdCC)	2+/3	0	3 of 3	AdCC
15	Adenoid cystic carcinoma	0	0	0 of 3 ^a	AdCC
72	Adenocarcinoma, NOS	3+/3	1+/3	2 of 3	AdCC
44	Myoepithelial carcinoma	3+/3	1+/3	3 of 3	Myoepithelial carcinoma with AdCC-like feature
27	Salivary duct carcinoma (SDC)	1+/3	1+/3	1 of 3	SDC

NOS, not otherwise specified.

^aMyb positivity was observed in additional whole section staining.

year ago) were immunohistochemically tested and all three cases showed Myb positivity with a peripheral pattern.

Relationships between markers

SOX10 expression and Myb expression were significantly correlated ($p < .001$). Only one case was Myb positive despite being SOX10 negative in tissue microarray, but this case was reclassified as Myb-negative after additional whole section staining. Finally, all Myb-positive cases showed SOX10 positivity.

In pleomorphic adenoma, 16 of 48 cases (33.3%) showed Myb positivity. This trend was the same regardless of PLAG1 positivity or negativity (31.0% and 36.8%, respectively).

DISCUSSION

Salivary gland neoplasms exhibit extensive morphologic diversity and overlapping characteristics. Until recently, the classification of salivary gland tumors largely depended on histomorphological findings and cellular lineages.⁹ Recent advances have been made in salivary gland tumor pathology, particularly with the development of methods for analyzing molecular tumorigenesis. Previous studies showed that many subtypes of salivary gland tumors can be defined by tumor-specific translocation.¹⁰

Specific genetic rearrangements have been recognized as useful diagnostic markers of salivary gland neoplasms. Most secretory carcinomas harbor a t(12;15)(p13;q25) translocation that results in *ETV6-NTRK3* fusion⁹: *EWSR1-ATF1* fusion was detected in nearly all cases of hyalinizing clear cell carcinoma, and approximately 80% of low-grade mucoepidermoid carcinomas exhibited *CRTC1-MAML2* fusion.² *MYB-NFIB* fusion was reported in 28%–86% of adenoid cystic carcinoma cases,⁷ although the proto-oncogene *MYB* could also have other fusion partners. Fusion involving the *PLAG1* locus has been reported in 24%–88% of pleomorphic adenomas and CA ex-PA.¹¹

Fluorescence *in situ* hybridization (FISH) is the gold-standard method for evaluating chromosomal rearrangements. However,

this detection method is costly, requires a fluorescence microscope, and is time- and labor-intensive.¹² Immunohistochemical staining is a reasonable and more economical alternative. IHC analysis is particularly advantageous in cases where oncoprotein overexpression results from low-level amplification or alternative mechanisms such as epigenetic pathways.

Several of the recognized cytogenetic alterations in pleomorphic adenoma are translocations involving 8q12 or 12q13-15.1. Researchers discovered that the oncogenes *PLAG1* (located at 8q12) and *HMGA2* (located at 12q15) are present in those particular lesions.⁹ In 2005, Martins *et al.*¹³ reported that *PLAG1* gene alterations were observed in 14 of 16 cases (87.5%) of salivary gland pleomorphic adenoma using *in situ* hybridization. Since then, five studies have reported *PLAG1* immunopositivity in salivary pleomorphic adenoma, with a rate of 92%–100% positivity.^{11,14-17} Katabi *et al.*¹¹ compared *PLAG1* FISH and IHC results in salivary pleomorphic adenoma with positivity rates of 33% (5/15) and 96% (22/23), respectively. Matsuyama *et al.*¹⁷ reported the proportion of *PLAG1* gene alteration in salivary pleomorphic adenoma as 24% (11/45) using reverse transcription polymerase chain reaction whereas *PLAG1* immunoreactivity was 100% (45/45). This discrepancy could be explained by the existence of another mechanism for *PLAG1* protein expression other than *PLAG1* rearrangement. Matsuyama *et al.*¹⁷ reported that some *PLAG1*-immunopositive PA cases did not exhibit *PLAG1* rearrangements or express the *HMGA2-WIF1* fusion transcript. Moreover, promoter swapping mechanisms or low-level amplification of chromosome 8 result in *PLAG1* overexpression in lipoblastoma.¹⁸ In human development, *HMGA2* acts as a regulator of *PLAG1* expression in the *HMGA2-PLAG1-IGF2* pathway.¹⁹ Overexpression of *PLAG1* was also reported in several other human tumors, such as lipoblastoma, hepatoblastoma, and acute myeloid leukemia,²⁰ in the absence of consistent genetic fusion including *PLAG1*. Hence, *PLAG1* fusion accounts for only a portion of *PLAG1* protein overexpression in salivary gland PA.

Our cohort included one case of CA ex-PA, which showed PLAG1 negativity. Whole-section staining was additionally conducted for the CA ex-PA case; however, PLAG1 immunoreactivity was not observed in the carcinoma or adenoma portions (not shown). Previous studies have attempted to distinguish between CA ex-PA and other carcinomas of the salivary glands using PLAG1 IHC. The proportion of PLAG1-immunopositive salivary CA ex-PA in studies including more than 10 CA ex-PA cases was 35%–60%, which was lower than that of benign PA (92%–100%).^{11,15,21}

SOX10 IHC was recently used to diagnose Schwann cell and melanocytic tumors, particularly malignant peripheral nerve sheath tumor and malignant melanoma.⁵ Immunostaining using monoclonal anti-SOX10 antibody showed consistent results and therefore can be immediately applied in clinical diagnostic practice. Epithelial structures of normal salivary gland tissue are divided into four parts: acinus, intercalated duct, striated duct, and excretory duct. SOX10 was expressed in acinar cells, myoepithelial cells in acini, and luminal cells in intercalated ducts.⁶ Although each salivary gland tumor is thought to originate in the reserve cells and/or stem cell progenitors, histological similarities between the normal salivary gland tissue and the primary salivary gland neoplasms were widely observed.²² Pleomorphic adenoma, monomorphic adenoma (including basal cell adenoma), adenoid cystic carcinoma, epithelial-myoepithelial carcinoma, and polymorphous low-grade adenocarcinoma were considered to be related to the intercalated duct²² and all of them showed SOX10 positivity in our study (Table 3). In contrast, 27 Warthin tumors and one oncocytoma, which are considered to be of striated duct origin, and three cystadenomas, considered to be of excretory duct origin, showed SOX10 negativity. SOX10 appears to be a potential marker for cells of origin and differentiation in salivary gland tumors.²³

In the literature, several authors have reported SOX10 positivity of acinic cell carcinoma (AciCC).^{6,23} Only one AciCC case was included in this study. Contrary to the findings of Hsieh *et al.*,²³ negative to scant positive tumor cells were observed in our case after whole section staining. This intensity was similar to the few positive cells found in four Warthin tumor cases. We concluded that our AciCC case was SOX10-positive, despite differing opinions among other authors. In our study, the staining intensity of SOX10 was low in normal serous acinus compared with intercalated ductal cells and intercalated duct-originated tumors, and mucinous acinar cells did not express SOX10 (Fig. 2A). Ohtomo *et al.*⁶ reported that SOX10 was weakly expressed in mucinous acinar cells and more intensely expressed in serous

acinar cells. Considering this expression pattern in normal salivary glands, the scant positivity in our AciCC cases seems to be due to the difference in experimental conditions. Several factors may have contributed towards this low intensity including the facts that acinar cells contain digestive enzymes and that tissue of this case was collected 10 years before the study.

The avian myeloblastosis viral oncogene homolog v-Myb is a proto-oncogene located at 6q22–23¹¹ and the recurrent t(6;9)(q22–23;p23–24) translocation is repeatedly observed in adenoid cystic carcinoma of the salivary glands. This translocation results in fusion of the MYB proto-oncogene with the transcription factor gene NFIB.⁷ Adenoid cystic carcinoma showed a unique histologic feature regardless of the organ of origin. Myb overexpression was detected in adenoid cystic carcinoma of the salivary glands,^{7,24} lacrimal glands,^{25,26} skin,²⁷ and breast.²⁸ The proportion of MYB translocation in salivary adenoid cystic carcinomas varied between studies, with values ranging from 28% to 86%.⁷ In previous studies 65% to 82% of adenoid cystic carcinoma cases showed Myb protein expression.^{7,24} Mitani *et al.*²⁴ conducted concurrent MYB-NFIB fusion FISH and Myb IHC and found that 61% (25 of 41) of adenoid cystic carcinomas without MYB-NFIB fusion showed Myb immunopositivity. In breast cancer, Myb IHC is more sensitive than MYB-NFIB FISH in the diagnosis of adenoid cystic carcinoma.²⁸ In our study, one case showed Myb negativity according to the tissue microarray but focal Myb positivity of the peripheral pattern was observed in whole section staining. Brill *et al.*⁷ also reported this phenomenon as a “peculiar zonal staining pattern.” Since normal Myb has a half-life of approximately 30 minutes,²⁹ the peripheral staining problem might be related to degradation and the fixation procedures used in daily practice. We also added three recent adenoid cystic carcinoma cases and all showed Myb positivity with the same staining pattern (not shown).

One case (No. 72) had ambiguous histologic features showing characteristics of both adenoid cystic carcinoma (AdCC) and adenocarcinoma, NOS at the time of primary diagnosis. After histologic review and consideration of Myb positivity, the authors concluded that this case was AdCC. Another Myb-positive case (No. 44) was initially diagnosed as myoepithelial carcinoma, and the tumor had foci of AdCC-like histologic features. Results of Myb IHC showed a marginal staining pattern and heterogeneous expression. Interpretation of Myb IHC requires caution when the study material is a biopsy or tissue microarray specimen; however, Myb IHC staining of the surgical specimen may be helpful when the diagnosis of AdCC is uncertain on histology.

In this study, we used newly developed IHC markers for the

diagnostic evaluation of salivary gland neoplasms in a relatively large number of cases. We found that PLAG1 expression was specific to pleomorphic adenoma. SOX10 IHC may be helpful for diagnosing salivary gland neoplasms, which show acinus and/or intercalated duct differentiation. Since SOX10 is expressed in various malignant tumors of salivary gland, its diagnostic value as a marker is relatively low. Myb immunohistochemistry is sensitive for adenoid cystic carcinoma detection in large resected specimens, especially when the tumor has ambiguous histology; however, caution is required for small biopsy specimens. Salivary gland tumors include a large and diverse group of tumors with overlapping histological features. New immunohistochemistry markers may play an important role in confirming the diagnosis of specific salivary gland tumors and broadening our understanding of salivary gland tumorigenesis.

ORCID

Ji Hyun Lee: <https://orcid.org/0000-0002-7971-6516>
 Hye Ju Kang: <https://orcid.org/0000-0002-2178-0005>
 Chong Woo Yoo: <https://orcid.org/0000-0002-5221-4516>
 Weon Seo Park: <https://orcid.org/0000-0002-0035-1455>
 Junsun Ryu: <https://orcid.org/0000-0002-6730-6755>
 Yuh-Seog Jung: <https://orcid.org/0000-0002-9467-4916>
 Sung Weon Choi: <https://orcid.org/0000-0002-2038-2881>
 Joo Yong Park: <https://orcid.org/0000-0002-0969-151X>
 Nayoung Han: <https://orcid.org/0000-0001-8710-4280>

Conflicts of Interest

The authors declare that they have no potential conflicts of interest.

Acknowledgments

This research was supported by a National Cancer Center of the Republic of Korea Grant (no. 1810022-1).

REFERENCES

- Rosai J. Rosai and Ackerman's surgical pathology. Philadelphia: Mosby, 2011.
- Griffith CC, Schmitt AC, Little JL, Magliocca KR. New Developments in salivary gland pathology: clinically useful ancillary testing and new potentially targetable molecular alterations. *Arch Pathol Lab Med* 2017; 141: 381-95.
- Van Dyck F, Declercq J, Braem CV, Van de Ven WJ. PLAG1, the prototype of the PLAG gene family: versatility in tumour development (review). *Int J Oncol* 2007; 30: 765-74.
- Zatkova A, Rouillard JM, Hartmann W, *et al.* Amplification and overexpression of the IGF2 regulator PLAG1 in hepatoblastoma. *Genes Chromosomes Cancer* 2004; 39: 126-37.
- Dabbs DJ. Diagnostic immunohistochemistry: theranostic and genomic applications. Philadelphia: Saunders, 2018.
- Ohtomo R, Mori T, Shibata S, *et al.* SOX10 is a novel marker of acinus and intercalated duct differentiation in salivary gland tumors: a clue to the histogenesis for tumor diagnosis. *Mod Pathol* 2013; 26: 1041-50.
- Brill LB 2nd, Kanner WA, Fehr A, *et al.* Analysis of MYB expression and MYB-NFIB gene fusions in adenoid cystic carcinoma and other salivary neoplasms. *Mod Pathol* 2011; 24: 1169-76.
- Kim SH, Park B, Joo J, *et al.* Retrospective analysis of 25 immunohistochemical tissue markers for differentiating multilocular cystic renal neoplasm of low malignant potential and multicystic renal cell carcinoma. *Histol Histopathol* 2018; 33: 589-96.
- El-Naggar AK, Chan JK, Grandis JR, Takata T, Slootweg PJ. WHO classification of head and neck tumors. Lyon: IARC Press, 2017.
- Vasef M, Auerbach A. Diagnostic pathology: molecular oncology. Philadelphia: Elsevier, 2016.
- Katabi N, Xu B, Jungbluth AA, *et al.* PLAG1 immunohistochemistry is a sensitive marker for pleomorphic adenoma: a comparative study with PLAG1 genetic abnormalities. *Histopathology* 2018; 72: 285-93.
- Han N, Kim MA, Lee HS, Kim WH. Evaluation of fibroblast growth factor receptor 2 expression, heterogeneity and clinical significance in gastric cancer. *Pathobiology* 2015; 82: 269-79.
- Martins C, Fonseca I, Roque L, *et al.* PLAG1 gene alterations in salivary gland pleomorphic adenoma and carcinoma ex-pleomorphic adenoma: a combined study using chromosome banding, in situ hybridization and immunocytochemistry. *Mod Pathol* 2005; 18: 1048-55.
- Rotellini M, Palomba A, Baroni G, Franchi A. Diagnostic utility of PLAG1 immunohistochemical determination in salivary gland tumors. *Appl Immunohistochem Mol Morphol* 2014; 22: 390-4.
- de Brito BS, Giovanelli N, Egal ES, *et al.* Loss of expression of Plag1 in malignant transformation from pleomorphic adenoma to carcinoma ex pleomorphic adenoma. *Hum Pathol* 2016; 57: 152-9.
- Avadhani V, Cohen C, Siddiqui MT. PLAG1: an immunohistochemical marker with limited utility in separating pleomorphic adenoma from other basaloid salivary gland tumors. *Acta Cytol* 2016; 60: 240-5.
- Matsuyama A, Hisaoka M, Nagao Y, Hashimoto H. Aberrant PLAG1 expression in pleomorphic adenomas of the salivary gland: a molecular genetic and immunohistochemical study. *Virchows Arch* 2011; 458: 583-92.

18. Deen M, Ebrahim S, Schloff D, Mohamed AN. A novel PLAG1-RAD51L1 gene fusion resulting from a t(8;14)(q12;q24) in a case of lipoblastoma. *Cancer Genet* 2013; 206: 233-7.
19. Abi Habib W, Brioude F, Edouard T, *et al.* Genetic disruption of the oncogenic HMGA2-PLAG1-IGF2 pathway causes fetal growth restriction. *Genet Med* 2018; 20: 250-8.
20. Bartlett JM, Shaaban A, Schmitt F. *Molecular pathology: a practical guide for the surgical pathologist and cytopathologist*. Cambridge: Cambridge University Press, 2015.
21. Bahrami A, Dalton JD, Shivakumar B, Krane JF. PLAG1 alteration in carcinoma ex pleomorphic adenoma: immunohistochemical and fluorescence *in situ* hybridization studies of 22 cases. *Head Neck Pathol* 2012; 6: 328-35.
22. Mills SE. *Histology for pathologists*. Philadelphia: Lippincott Williams & Wilkins, 2012.
23. Hsieh MS, Lee YH, Chang YL. SOX10-positive salivary gland tumors: a growing list, including mammary analogue secretory carcinoma of the salivary gland, sialoblastoma, low-grade salivary duct carcinoma, basal cell adenoma/adenocarcinoma, and a subgroup of mucoepidermoid carcinoma. *Hum Pathol* 2016; 56: 134-42.
24. Mitani Y, Li J, Rao PH, *et al.* Comprehensive analysis of the MYB-NFIB gene fusion in salivary adenoid cystic carcinoma: incidence, variability, and clinicopathologic significance. *Clin Cancer Res* 2010; 16: 4722-31.
25. von Holstein SL, Fehr A, Persson M, *et al.* Adenoid cystic carcinoma of the lacrimal gland: MYB gene activation, genomic imbalances, and clinical characteristics. *Ophthalmology* 2013; 120: 2130-8.
26. Chen TY, Keeney MG, Chintakuntlawar AV, *et al.* Adenoid cystic carcinoma of the lacrimal gland is frequently characterized by MYB rearrangement. *Eye (Lond)* 2017; 31: 720-5.
27. North JP, McCalmont TH, Fehr A, van Zante A, Stenman G, LeBoit PE. Detection of MYB alterations and other immunohistochemical markers in primary cutaneous adenoid cystic carcinoma. *Am J Surg Pathol* 2015; 39: 1347-56.
28. Poling JS, Yonescu R, Subhawong AP, *et al.* MYB labeling by immunohistochemistry is more sensitive and specific for breast adenoid cystic carcinoma than MYB labeling by FISH. *Am J Surg Pathol* 2017; 41: 973-9.
29. Ramsay RG, Gonda TJ. MYB function in normal and cancer cells. *Nat Rev Cancer* 2008; 8: 523-34.

Uterine Malignant Mixed Müllerian Tumors Following Treatment with Selective Estrogen Receptor Modulators in Patients with Breast Cancer: A Report of 13 Cases and Their Clinicopathologic Characteristics

Byung-Kwan Jeong
Chang Ohk Sung
Kyu-Rae Kim

Department of Pathology, Asan Medical Center,
University of Ulsan College of Medicine, Seoul,
Korea

Received: September 28, 2018
Revised: October 30, 2018
Accepted: November 16, 2018

Corresponding Author

Kyu-Rae Kim, MD, PhD
Department of Pathology, Asan Medical Center,
University of Ulsan College of Medicine,
88 Olympic-ro 43-gil, Songpa-gu, Seoul 05505,
Korea
Tel: +82-2-3010-4514
Fax: +82-2-472-7878
E-mail: krkim@amc.seoul.kr

Background: Breast cancer treatment with selective estrogen receptor modulators (SERMs) increases the incidence of uterine malignant mixed Müllerian tumors (uMMMTs). We examine clinicopathologic characteristics and prognosis of SERM-associated uMMMTs (S-uMMMTs) and discuss possible pathogenetic mechanisms. **Methods:** Among 28,104 patients with breast cancer, clinicopathologic features and incidence of uMMMT were compared between patients who underwent SERM treatment and those who did not. Of 92 uMMMT cases that occurred during the same period, incidence, dose, and duration of SERM treatment, as well as overall survival rate, were compared for patients with breast cancer who underwent SERM treatment and those who did not (S-uMMMT vs NS-uMMMT) and for patients without breast cancer (de novo-uMMMT). Histopathological findings and immunophenotypes for myogenin, desmin, p53, WT-1, estrogen receptor (ER) α , ER β , progesterone receptor, and GATA-3 were compared between S-uMMMT and de novo-uMMMT. **Results:** The incidence of S-uMMMT was significantly higher than that of NS-uMMMT (6.35-fold). All patients with SERM were postmenopausal and received daily 20–40 mg SERM. Cumulative SERM dose ranged from 21.9 to 73.0 g (mean, 46.0) over 39–192 months (mean, 107). Clinicopathologic features, such as International Federation of Gynecology and Obstetrics stage and overall survival, were not significantly different between patients with S-uMMMT and NS-uMMMT or between patients with S-uMMMT and de novo-uMMMT. All 11 S-uMMMT cases available for immunostaining exhibited strong overexpression/null expression of p53 protein and significantly increased ER β expression in carcinomatous and sarcomatous components. **Conclusions:** SERM therapy seemingly increases risk of S-uMMMT development; however, clinicopathologic features were similar in all uMMMTs from different backgrounds. p53 mutation and increased ER β expression might be involved in the etiology of S-uMMMT.

Key Words: Malignant Müllerian mixed tumor; Selective estrogen receptor modulators; Tamoxifen; Breast neoplasm; p53

The use of selective estrogen receptor modulators (SERMs), including tamoxifen and toremifen, in patients with estrogen receptor (ER)-positive breast cancer is known to cause uterine and ovarian tumors. The therapeutic effect of SERMs in breast cancer is caused by blockade of estrogen binding to ER α ,^{1,2} which induces an antiestrogen effect. However, this also produces pro-estrogenic effects in other organ tissues, including the ovaries and endometrium,³⁻⁵ especially in postmenopausal women.⁶⁻¹¹ A variety of uterine tumors, including endometrial polyps, endometrial hyperplasia, endometrioid adenocarcinoma, Müllerian adenosarcoma,^{10,12-14} endometrial stromal sarcoma,^{15,16} leiomyosarcoma, and uterine malignant mixed Müllerian tumors (uMMMTs),¹⁷ have been associated with SERM treatment. Some

studies have suggested that the relative risk of uMMMTs after tamoxifen treatment is higher than that of endometrial adenocarcinomas, which are well-known secondary malignant tumors associated with tamoxifen treatment.^{10-13,18} Ovarian tumors, including serous cystadenoma, serous cystadenofibroma, fibroma, and endometrioid adenocarcinoma,¹⁹ as well as small cell carcinoma of pulmonary type,²⁰ are also known to be associated with SERM treatment, although a causative relationship has not been clearly elucidated. Tamoxifen treatment also induces vascular torsion, cystic necrosis, and ovarian cysts more frequently in premenopausal than postmenopausal women due to supraphysiological level of serum estrogen.²¹⁻²³ For this reason, the current recommendation of the American College of Obstetricians and

Gynecologists (ACOG) is close monitoring of patients receiving tamoxifen, especially those who are postmenopausal.²⁴

The etiology of uterine or ovarian tumors after SERM treatment remains unknown; however, it could be associated with certain factors common to postmenopausal women since most patients are postmenopausal. SERMs or their metabolites may induce a germline or somatic mutation in certain genes, or even epigenetic modifications,²⁵ resulting in increased oncogenicity and/or invasiveness.

However, uMMMTs have also been described in patients with BRCA1-associated breast cancer who have not received hormone therapy.²⁶ BRCA1 mutation carriers are predisposed to ovarian or uterine papillary serous carcinoma, from which uMMMTs often arise through sarcomatous transformation of high-grade serous carcinomas.^{27,28}

As a first step to unveiling the pathogenetic mechanism of uMMMT development after SERM treatment, we studied the incidence and prognosis of uMMMT in patients with breast cancer after SERM treatment, reviewed their clinicopathologic characteristics, and compared histopathological features between uMMMTs with and without SERM treatment and between those that occurred de novo without a prior history of breast cancer. Moreover, we examined the immunohistochemical expression of ER α , ER β , and p53 to investigate the roles of ER subtype and p53 in the pathogenetic mechanism.

MATERIALS AND METHODS

Patient selection

A group of patients with uMMMT but with no breast cancer history was designated as the de novo-uMMMT group. Another group of breast cancer patients who had undergone SERM treatment and later developed uMMMT were designated the SERM-associated uMMMTs (S-uMMMT) group, and breast cancer patients who did not receive SERM treatment but later developed uMMMT were designated the NS-uMMMT group. To analyze the incidence and relative risk of developing S-uMMMT, the prevalence of uMMMT was compared between patients who received SERM treatment and those who did not among 28,104 patients with breast cancer treated at Asan Medical Center, Seoul, Korea, between 2006 and 2016.

Of these patients, 14,221 were treated with SERM. A total of 13 patients developed S-uMMMT, while only two of 13,883 patients who were not treated with SERM developed NS-uMMMT during the same period.

Independently, a list of 92 patients who were histologically

diagnosed with uMMMTs during the same study period was retrieved from the database of the Department of Pathology at Asan Medical Center. Patients were divided into two groups based on the presence (13 patients) or absence of a clinical history of breast cancer with SERM treatment (79 patients, de novo-uMMMTs, including two patients with breast cancer history without SERM treatment). Clinical features for all patients, including age at diagnosis of breast or uterine tumors, menopausal status, International Federation of Gynecology and Obstetrics (FIGO) stage, family history of any malignancies, history of primary malignant tumors in other organs, and follow-up results, were obtained from their medical records. The histological characteristics of S-uMMMTs and NS-uMMMTs were analyzed, including primary site, size of uterine tumors, types of heterologous tumor components, and immunophenotypes. All patients provided written informed consent, and the institutional review board of Asan Medical Center (Seoul, Korea) approved this study (protocol 2018-1154). All study data were obtained in a completely anonymized form.

Histological examination and immunohistochemical staining

The histopathological features of all 92 patients with uMMMT were reviewed by two pathologists (B.-K.J. and K.-R.K.) with an emphasis on the presence of any particular tumor components.

Tissue sections for immunohistochemical staining were available for 13 of the 15 patients who developed uMMMT with a clinical history of breast cancer. Two of the 15 patients without available tissue sections belonged to the S-uMMMT group.

Paraffin-embedded tissue sections from 13 patients were stained immunohistochemically with mouse monoclonal antibodies to ER α (dilution 1:100, 6F11, Novocastra, Newcastle upon Tyne, UK), ER β (dilution 1:400, 14C8, Thermo Fisher Scientific, San Jose, CA, USA), progesterone receptor (PR; 1:200, Novocastra), GATA3 (dilution 1:200, L50-823, Cell Marque, Rocklin, CA, USA), WT-1 (dilution 1:100, 6F-H2, Dako, Glostrup, Denmark), myogenin (1:200, Neomarkers, Fremont, CA, USA), desmin (1:200, D33, Dako), and p53 (1:1,500, DO-7, Dako) using an Autoimmunostainer Benchmark XT (Ventana Medical Systems, Tucson, AZ, USA) and an Optiview DAB IHC detection kit (Ventana Medical Systems). Positive controls were normal endometrial tissue samples for ER α and PR, normal kidney tissue for GATA 3 and WT-1, normal skeletal muscle for desmin, rhabdomyosarcoma tissue for myogenin, and tubal high-grade serous carcinoma for p53. Primary antibodies were omitted for negative controls.

The immunoreactivity in all slides was scored by Allred's method by considering both the proportion and intensity of positive cells, which were independently recorded for each sample. The proportion of stained cells for ER α , ER β , PR, GATA3, WT-1, myogenin, and desmin on each slide was scored using a scale from 0 to 5, and staining intensity was scored from 0 to 3. The sum of these two partial scores produced the final score. Zero on this scale indicated negative staining. All cases with a final score ≥ 3 were considered positive.

A homogeneous staining pattern with strong intensity in more than 80% of tumor cell nuclei was considered "overexpression" for p53, while an inhomogeneous and/or weak staining pattern in < 80% of tumor cell nuclei was considered "non-overexpression." Complete negativity in any tumor cell nuclei, which is associated with null mutations,²⁹ was also considered abnormal. Immunoreactivity in the sarcomatous component was evaluated using the same methods as for the carcinomatous component.

Statistical analysis

Statistical analysis was performed by SPSS for Windows ver. 23.0 (IBM Corp., Armonk, NY, USA). The odds ratio of uMMMT associated with SERM treatment was estimated by comparing the incidences of S-uMMMT and NS-uMMMT in patients with breast cancer. The comparison was performed using Pearson's chi-square test. Comparison of categorical variables between S-uMMMTs and de novo-uMMMTs was also assessed by Pearson's chi-square test, while comparison of quantitative variables was analyzed by Student's t-test. Overall survival was calculated from the date of initial diagnosis until the date of last follow-up or patient death. Overall and recurrence-free survival rates were assessed by the Kaplan–Meier method, and differences between survival curves of patients with S-uMMMT and de novo-uMMMT were compared by the log-rank test. Differences with $p <$

.05 were considered significant.

RESULTS

Relative risk of developing uMMMTs in patients with breast cancer after SERM treatment

There was a significant difference in incidence of uMMMT between the two groups of patients with breast cancer (Table 1); a higher proportion of SERM patients developed S-uMMMT ($n = 13$, 0.091%) compared with those who did not receive SERM treatment ($n = 2$, 0.014%), with a 6.35-fold increased risk of developing S-uMMMT ($p = .005$). The age of patients with breast cancer at diagnosis ranged from 15 to 94 years (median, 53). Patients who did not receive SERM treatment were older than patients with SERM treatment ($p < .001$) (Table 2).

Of the 13 patients with SERM, nine were treated with tamoxifen and three were treated with toremifen for 5 years. One was treated with toremifen for the first 4 years and then switched to tamoxifen treatment for uMMMT. The duration of SERM treatment ranged from 36 to 60 months (mean 58 months) with a daily dose of 20–40 mg. The cumulative dose of tamoxifen or toremifen ranged from 21.9 to 73.0 g (mean, 46.0 g; median, 36.5 g).

Of the 10 patients with S-uMMMT whose breast cancer tissue was available for p53 immunostaining, eight exhibited a wild-type pattern, while two exhibited strong reactivity. In contrast, strong immunoreactivity or complete negativity was present in all 11 patients whose S-uMMMT tissue was available for p53 immunostaining, suggesting that a new p53 mutation had occurred in the uterine tumor.

Clinicopathologic features of S-uMMMTs

The age of patients with breast cancer who later developed S-uMMMT ranged from 37 to 67 years (mean, 53), and all but one

Table 1. Incidence of uMMMTs in patients with breast cancer who did or did not undergo preceding long-term SERM treatment

	uMMMT, n (%)	Odds ratio	p-value
Breast cancer treated with long-term SERM	13/14,221 (0.091)	6.350	.004
Breast cancer treated without long-term SERM	2/13,883 (0.014)		

uMMMTs, uterine malignant mixed Müllerian tumors; SERM, selective estrogen receptor modulator.

Table 2. Comparison of age in patients with breast cancer who did or did not undergo preceding long-term SERM treatment

	Median age and older (≥ 53 yr)	Younger than median age (< 53 yr)	p-value
Breast cancer treated with long-term SERM	6,911 (48.6)	7,310 (51.4)	$< .001$
Breast cancer treated without long-term SERM	7,650 (55.1)	6,233 (44.9)	

Values are presented as number (%).

SERM, selective estrogen receptor modulator.

patient (n=12, 92.3%) were postmenopausal (Table 3). The age at diagnosis of S-uMMMT ranged from 40 to 76 years (mean, 62), at which point all were menopausal or postmenopausal. The duration from start of SERM treatment to onset of S-uMMMT ranged from 39 to 192 months (mean, 107 months).

The size of S-uMMMTs ranged from 1.5 to 13 cm in longest dimension (mean, 6.8 cm). Three patients (23.1%) had lymph node metastasis at the time of diagnosis of S-uMMMT, and eight patients (53.8%) had lymphovascular invasion. Seven patients had FIGO stage I (53.8%), three had stage III (23.1%), and three had stage IV (23.1%).

BRCA mutation tests were not performed in any patients; however, none of the 13 patients with S-uMMMT had any family history of breast, ovarian, or endometrial cancers. One of the two NS-uMMMT patients had a family history of breast and endometrial cancers in her siblings.

Clinical outcomes including lymph node metastasis (p = .694), FIGO stage (p = .518), overall survival rate (p = .859), and recurrence-free survival rate (p = .696) were not significantly different between patients with S-uMMMTs and de novo-uMMMTs (Table 4, Fig. 1), nor between patients with S-uMMMT and NS-uMMMT. The rate of lymph node metastasis was slightly lower in

Table 3. Clinicopathologic characteristics of patients with uterine malignant mixed Müllerian tumor with preceding breast cancer history

Age (yr)	SERM treatment	Time from treatment to onset (mo)	Menopause	Tumor size (greatest dimension in cm)	Lymph node metastasis	Lymphovascular invasion	FIGO stage	Sarcomatous component
72	TOR 5 yr	61	Postmenopause	6.5	Not identified	Not identified	1A	Heterologous
68	TAM 5 yr	48	Postmenopause	1.5	Not identified	Not identified	1B	Homologous
52	TAM 5 yr	61	Postmenopause	2.8	Present	Present	3C2	Homologous
40	TAM 3 yr	39	Postmenopause	10.9	Not identified	Present	3A	Homologous
58	TAM 5 yr	119	Postmenopause	6.0	Not identified	Present	3A	Homologous
64	TOR 5 yr	131	Postmenopause	10.0	Not identified	Present	1A	Homologous
59	TAM 5 yr	128	Postmenopause	25.0	Present	Present	4B	Heterologous
69	TOR 5 yr	107	Postmenopause	6.8	Not identified	Not identified	1A	Homologous
53	TAM 5 yr	69	Premenopause	13.0	Present	Present	4B	Heterologous
61	TAM 5 yr	115	Postmenopause	7.5	Not identified	Not identified	4B	Heterologous
55	TAM 5 yr	77	Postmenopause	1.5	Not identified	Not identified	1A	Homologous
75	TAM 5 yr	178	Postmenopause	8.0	Not identified	Present	1A	Heterologous
76	TAM 5 yr	192	Postmenopause	2.6	Not resected ^a	Present	1A	Homologous
54	No	60	Postmenopause	2.4	Not resected ^a	Not identified	1A	Heterologous
65	No	65	Postmenopause	9.0	Not identified	Present	4B	Heterologous

SERM, selective estrogen receptor modulator; FIGO, International Federation of Gynecology and Obstetrics; TOR, toremifen; TAM, tamoxifen.

^aLymph nodes were preserved.

Table 4. Comparison of clinicopathologic characteristics between patients with uMMMT with preceding SERM treatment (S-uMMMT) and patients with de novo-uMMMT

Baseline characteristic	Total (n = 92)	S-uMMMT (n = 13)	De novo-uMMMT (n = 79)	p-value ^a
				.555
Patient age (yr)	61 (40–77)	60 (40–76)	60 (45–77)	
Menopause				.523
Premenopause	4 (4.3)	1 (7.7)	3 (3.8)	
Postmenopause	88 (95.7)	12 (92.3)	76 (96.2)	
Tumor size (greatest dimension)				.404
Size (cm)	6 (0.6–15.2)	6.8 (1.5–13.0)	6 (0.6–15.2)	
Node metastasis	37 (40.2)	3 (23.1)	34 (45.9)	.174
Lymphovascular invasion	52 (56.5)	8 (61.5)	44 (55.7)	.694
FIGO stage				.518
Stage 1	37 (40.7)	7 (53.8)	30 (38.5)	
Stage 2	5 (5.5)	0	5 (6.4)	
Stage 3	32 (35.2)	3 (23.1)	29 (37.1)	
Stage 4	17 (18.7)	3 (23.1)	14 (17.9)	
Heterologous sarcomatous component	34 (37.0)	5 (38.5)	29 (36.7)	.903

Values are presented as median (range) or number (%).

uMMMT, uterine malignant mixed Müllerian tumor; SERM, selective estrogen receptor modulator; FIGO, International Federation of Gynecology and Obstetrics.

^aBased on a chi-square test for categorical variables and on a t-test for continuous variables.

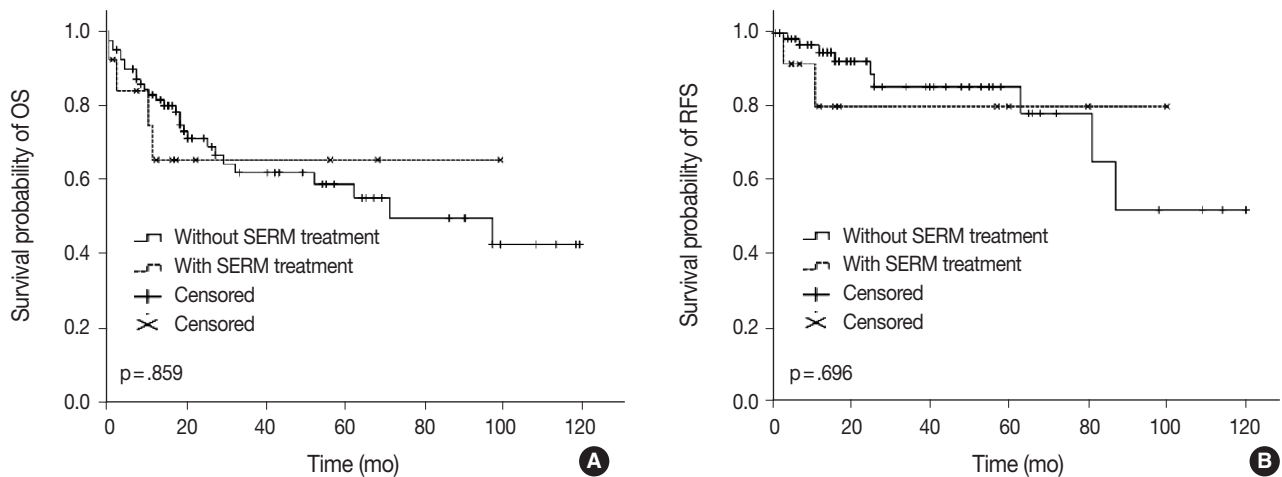


Fig. 1. Kaplan-Meier survival curves comparing overall survival (OS) (A) and recurrence-free survival (RFS) (B) rates in patients with selective estrogen receptor modulators (SERM)-treated breast cancer with subsequent uterine malignant mixed Müllerian tumors (uMMMTs) and de novo-uMMMTs in patients with no preceding breast cancer or preceding breast cancer without SERM treatment.

patients with S-uMMMT compared to those with de novo-uMMMT (23.1% vs 45.9%), but the difference was not statistically significant ($p = .174$).

Histological comparison of uMMMTs in breast cancer patients with and without SERM treatment

Histologically, all 13 S-uMMMTs were composed of a mixture of malignant epithelial and mesenchymal components. Rhabdomyoblasts were frequently identified in hematoxylin and eosin-stained sections in five patients (38.5%), and the exclusive presence of rhabdomyoblasts was a characteristic of one patient, mimicking a pure rhabdomyosarcoma. Other components such as chondrosarcomatous, osteosarcomatous, or liposarcomatous components were not identified. Of the 79 de novo-uMMMT, 50 were homologous, while 29 (36.7%) contained heterologous elements in the form of rhabdomyoblasts (18 cases, 22.8%) or malignant cartilage (8 cases, 10.1%). Epithelial components were mostly composed of high-grade papillary serous carcinomas both in S-uMMMTs and de novo-uMMMTs, and serous carcinoma was the only epithelial component in seven cases (53.8%). Three cases of S-uMMMT (23.1%) exhibited sarcomatous overgrowth with a hardly discernible carcinomatous component, while this feature was found in eight cases of de novo-uMMMT (10.1%). Collectively, significant histopathological differences were not identified between S-uMMMTs and de novo-uMMMTs.

Immunohistochemistry of uMMMT cases with preceding breast cancer

Protein expression as revealed by immunohistochemical staining

did not show any significant differences between S-uMMMTs ($n = 11$) and NS-uMMMTs ($n = 2$) (Fig. 2). All 11 S-uMMMT samples exhibited either diffuse overexpression ($n = 8$) or complete loss of p53 expression ($n = 3$) in the nuclei.

All 11 S-uMMMT cases exhibited strong immunoreactivity for ER β in both carcinomatous and sarcomatous components (Fig. 2). Only 45.5% of cases ($n = 5$) showed weak, focal immunoreactivity to ER α , and the remaining cases were negative, suggesting an increased ratio of ER β to ER α expression. Progesterone receptors were expressed in a smaller number of cases ($n = 2$), while the frequency of immunoreactivity to myogenin and desmin, which highlight rhabdomyoblasts, was 45.5% ($n = 5$) and 45.5% ($n = 5$), respectively. Detailed information of immunohistochemical staining results is presented in Table 5.

DISCUSSION

The occurrence of uMMMTs has been described in patients with *BRCA1*-associated breast cancer who did not receive hormone therapy, as well as in patients with SERM treatment.²⁶ Moreover, one population-based study proposed that hormone therapy itself has a negligible effect on the incidence of uMMMT.²⁶ Therefore, we initially suspected that oncogenicity after SERM treatment could be associated with preexisting genetic changes, such as *BRCA* mutations. However, none of the 13 S-uMMMT patients in our cohort had a family history of malignant tumors, especially in breasts and female genital organs. In addition, most patients were postmenopausal at the time of breast or uterine cancer diagnosis, which is not a typical clinical

feature of *BRCA* mutation-associated tumors. It is less likely that patients with S-uMMMT have a hereditary cancer predisposition, although comprehensive genetic analysis was not per-

formed in this study. Patients with breast cancer who were treated with SERM were younger than those who were not treated with SERM. This result is not consistent with previous studies

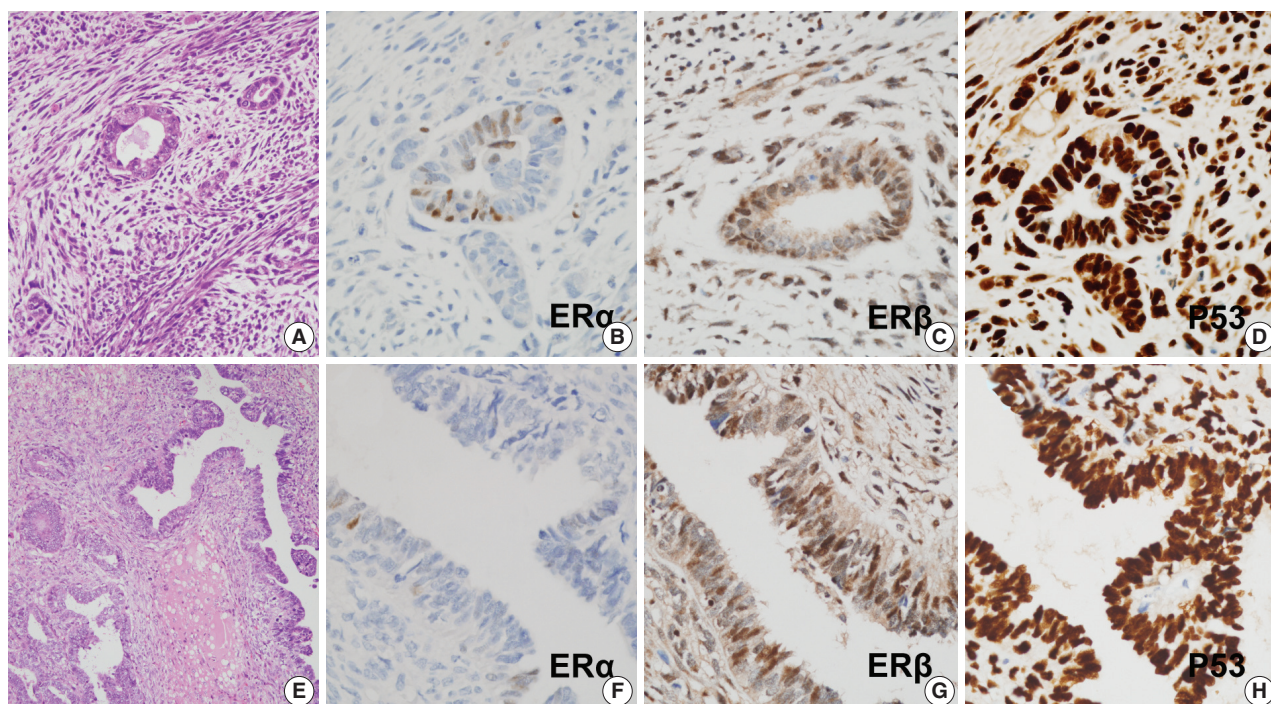


Fig. 2. Histopathologic and immunohistochemical features of uterine malignant mixed Müllerian tumors (A–D) occurring in patients with breast cancer with (A–D) or without (E–H) prior selective estrogen receptor modulator treatment, showing no significant differences: hematoxylin and eosin (A, E), estrogen receptor (ER) α (B, F), ER β (C, G), and p53 (D, H).

Table 5. Allred scoring of immunohistochemical results of patients with uMMMT with preceding breast cancer

Patient	Allred score	ER α	ER β	PR	GATA-3	WT-1	p53	Myogenin	Desmin
SERM (+)									
Negative	0	6 (54.5)	-	9 (81.8)	11 (100)	1 (9.1)	3 (27.3) ^a	6 (54.5)	6 (54.5)
	2	-	-	-	-	-	-	-	-
Positive	3	-	-	-	-	-	-	-	-
	4	2 (18.2)	-	-	-	-	-	-	-
	5	1 (9.1)	-	-	-	3 (27.3)	-	4 (36.4)	4 (36.4)
	6	-	2 (18.2)	-	-	4 (36.4)	-	1 (9.1)	1 (9.1)
	7	2 (18.2)	7 (63.6)	2 (18.2)	-	-	-	-	-
	8	-	2 (18.2)	-	-	3 (27.3)	8 (72.7)	-	-
SERM (-)									
Negative	0	-	-	1 (50)	2 (100)	-	-	-	-
	2	-	-	-	-	-	-	-	-
Positive	3	-	-	-	-	-	-	-	-
	4	-	-	-	-	-	-	2 (100)	2 (100)
	5	2 (100)	-	1 (50)	-	-	-	-	-
	6	-	1 (50)	-	-	2 (100)	-	-	-
	7	-	1 (50)	-	-	-	-	-	-
	8	-	-	-	-	-	2 (100)	-	-

Values are presented as number (%).

uMMMT, uterine malignant mixed Müllerian tumor; ER, estrogen receptor; PR, progesterone receptor; SERM, selective estrogen receptor modulator.

^aAll tumor cell nuclei were negative.

showing that triple negative breast cancers are diagnosed at a younger age than ER and/or PR positive breast cancers.^{30,31} This might be related to the methodology of the present study, which only reflects SERM treatment status, while exact statuses of ER, PR, and HER2 were not collected. Our results suggest that differences in menopause status due to age did not alter the effect of SERM treatment on uMMMT.

Endometrial carcinomas develop in females who have had cumulative doses greater than 35 g of tamoxifen,³² however, only a small proportion of patients who received this amount of drug developed uterine malignancy in this study, irrespective of dose. The duration of SERM treatment ranged widely from 39 to 192 months (mean, 107 months), so dose and duration may not be closely related to risk factors of uMMMT.

While endometrial carcinomas after tamoxifen treatment are equally distributed in pre- and postmenopausal women,³³ S-uMMMT occurs almost exclusively in postmenopausal women in both this study and in the literature.^{17,34} Thus, the tumorigenic mechanism of S-uMMMT could be associated with certain factors common to postmenopausal women. One cross-sectional study reported that ER β expression, but not ER α , was higher in postmenopausal women than in premenopausal women,³⁵ suggesting that ER β expression or the ratio of ER β to ER α is elevated in postmenopausal women. ER α and ER β have similarities in structure and mechanism of action, including interaction with other transcription factors, but they have distinct functions in hormonal resistance and cellular processes.

Resistance to endocrine therapy develops in 25%–50% of patients who receive tamoxifen treatment for breast cancer, and the mechanism by which this occurs has been partly elucidated. Tamoxifen disrupts estrogen–ER α binding and can block cell proliferation and induce apoptotic cell death. During tamoxifen treatment, ubiquitin ligase CUE domain-containing protein 2 (CUEDC2) is expressed at low levels, which causes a low rate of proteasome-mediated degradation of ER α .³⁶ Tamoxifen-resistant cells with increased expression of CUEDC2 may appear, thereby elevating degradation and turnover of ER α and conferring resistance to tamoxifen treatment.³⁶ The inhibitory effect of ER β on binding of p53–ER α suggests that competition between ER subtypes on the binding of p53 may occur in cells that express both receptors. While there are inverse associations between ER α activity and p53, ER β has been reported to inhibit breast tumorigenesis by acting alone or in concert with p53 and p63.³⁷ In our study, all 11 cases of S-uMMMT available for immunostaining exhibited diffuse, strong overexpression for p53 and ER β and negative or weak expression for ER α and PR in both

carcinomatous and sarcomatous components. Further research is needed to clarify how SERM works on ER β , especially in postmenopausal women.

In conclusion, the immunohistochemical results in our study suggest that both S-uMMMTs and NS-uMMMTs are related to p53 mutation, and clinicopathologic features were similar in all uMMMTs from different backgrounds. Increased ER β expression or ratio of ER β to ER α in postmenopausal women and binding of ER β to mutant p53 might induce carcinogenesis, sarcomatous transformation, epithelial mesenchymal transition, and invasiveness in organ tissues expressing both receptors. This hypothesis should be tested in further detailed studies.

ORCID

Byung-Kwan Jeong: <https://orcid.org/0000-0002-0038-3959>
 Chang O. Sung: <https://orcid.org/0000-0002-8567-456X>
 Kyu-Rae Kim: <https://orcid.org/0000-0002-5781-7447>

Conflicts of Interest

The authors declare that they have no potential conflicts of interest.

REFERENCES

- Kennedy BJ. Hormone therapy for advanced breast cancer. *Cancer* 1965; 18: 1551-7.
- Elwood JM, Godolphin W. Oestrogen receptors in breast tumours: associations with age, menopausal status and epidemiological and clinical features in 735 patients. *Br J Cancer* 1980; 42: 635-44.
- Cook LS, Weiss NS, Schwartz SM, *et al.* Population-based study of tamoxifen therapy and subsequent ovarian, endometrial, and breast cancers. *J Natl Cancer Inst* 1995; 87: 1359-64.
- Webb P, Lopez GN, Uht RM, Kushner PJ. Tamoxifen activation of the estrogen receptor/AP-1 pathway: potential origin for the cell-specific estrogen-like effects of antiestrogens. *Mol Endocrinol* 1995; 9: 443-56.
- Assikis VJ, Jordan VC. Gynecologic effects of tamoxifen and the association with endometrial carcinoma. *Int J Gynaecol Obstet* 1995; 49: 241-57.
- van Leeuwen FE, Benraadt J, Coebergh JW, *et al.* Risk of endometrial cancer after tamoxifen treatment of breast cancer. *Lancet* 1994; 343: 448-52.
- Fisher B, Costantino JP, Redmond CK, Fisher ER, Wickerham DL, Cronin WM. Endometrial cancer in tamoxifen-treated breast cancer patients: findings from the National Surgical Adjuvant Breast and

- Bowel Project (NSABP) B-14. *J Natl Cancer Inst* 1994; 86: 527-37.
8. Barakat RR. The effect of tamoxifen on the endometrium. *Oncology (Williston Park)* 1995; 9: 129-34.
 9. Bernstein L, Deapen D, Cerhan JR, *et al.* Tamoxifen therapy for breast cancer and endometrial cancer risk. *J Natl Cancer Inst* 1999; 91: 1654-62.
 10. Bergman L, Beelen ML, Gallee MP, Hollema H, Benraadt J, van Leeuwen FE. Risk and prognosis of endometrial cancer after tamoxifen for breast cancer. *Comprehensive Cancer Centres' ALERT Group. Assessment of liver and endometrial cancer risk following tamoxifen. Lancet* 2000; 356: 881-7.
 11. Jones ME, van Leeuwen FE, Hoogendoorn WE, *et al.* Endometrial cancer survival after breast cancer in relation to tamoxifen treatment: pooled results from three countries. *Breast Cancer Res* 2012; 14: R91.
 12. Wysowski DK, Honig SF, Beitz J. Uterine sarcoma associated with tamoxifen use. *N Engl J Med* 2002; 346: 1832-3.
 13. Wickerham DL, Fisher B, Wolmark N, *et al.* Association of tamoxifen and uterine sarcoma. *J Clin Oncol* 2002; 20: 2758-60.
 14. Lavie O, Barnett-Griness O, Narod SA, Rennett G. The risk of developing uterine sarcoma after tamoxifen use. *Int J Gynecol Cancer* 2008; 18: 352-6.
 15. Eddy GL, Mazur MT. Endolymphatic stromal myosis associated with tamoxifen use. *Gynecol Oncol* 1997; 64: 262-4.
 16. Christie DB 3rd, Day JD, Moore AB, Chapman JR, Nakayama DK, Conforti AM. Endometrial stromal sarcoma development after hysterectomy and tamoxifen therapy. *Am Surg* 2008; 74: 726-8.
 17. McCluggage WG, Abdulkader M, Price JH, *et al.* Uterine carcinosarcomas in patients receiving tamoxifen: a report of 19 cases. *Int J Gynecol Cancer* 2000; 10: 280-4.
 18. Curtis RE, Freedman DM, Sherman ME, Fraumeni JF Jr. Risk of malignant mixed mullerian tumors after tamoxifen therapy for breast cancer. *J Natl Cancer Inst* 2004; 96: 70-4.
 19. Cohen I, Altaras MM, Lew S, Tepper R, Beyth Y, Ben-Baruch G. Ovarian endometrioid carcinoma and endometriosis developing in a postmenopausal breast cancer patient during tamoxifen therapy: a case report and review of the literature. *Gynecol Oncol* 1994; 55(3 Pt 1): 443-7.
 20. Yin L, Li J, Wei Y, Ma D, Sun Y, Sun Y. Primary ovarian small cell carcinoma of pulmonary type with coexisting endometrial carcinoma in a breast cancer patient receiving tamoxifen: a case report and literature review. *Medicine (Baltimore)* 2018; 97: e10900.
 21. Shushan A, Peretz T, Uziely B, Lewin A, Mor-Yosef S. Ovarian cysts in premenopausal and postmenopausal tamoxifen-treated women with breast cancer. *Am J Obstet Gynecol* 1996; 174(1 Pt 1): 141-4.
 22. Cohen I, Figer A, Tepper R, *et al.* Ovarian overstimulation and cystic formation in premenopausal tamoxifen exposure: comparison between tamoxifen-treated and nontreated breast cancer patients. *Gynecol Oncol* 1999; 72: 202-7.
 23. Kojima N, Yamasaki Y, Koh H, Miyashita M, Morita H. Long-acting luteinizing hormone-releasing hormone agonist for ovarian hyperstimulation induced by tamoxifen for breast cancer. *Case Rep Obstet Gynecol* 2018; 2018: 4931852.
 24. Committee Opinion No. 601: Tamoxifen and uterine cancer. *Obstet Gynecol* 2014; 123: 1394-7.
 25. Pandey V, Zhang M, Chong QY, *et al.* Hypomethylation associated enhanced transcription of trefoil factor-3 mediates tamoxifen-stimulated oncogenicity of ER+ endometrial carcinoma cells. *Oncotarget* 2017; 8: 77268-91.
 26. Wilson BT, Cordell HJ. Uterine carcinosarcoma/malignant mixed Mullerian tumor incidence is increased in women with breast cancer, but independent of hormone therapy. *J Gynecol Oncol* 2015; 26: 249-51.
 27. Biron-Shental T, Drucker L, Altaras M, Bernheim J, Fishman A. High incidence of *BRCA1-2* germline mutations, previous breast cancer and familial cancer history in Jewish patients with uterine serous papillary carcinoma. *Eur J Surg Oncol* 2006; 32: 1097-100.
 28. Pennington KP, Walsh T, Lee M, *et al.* *BRCA1*, *TP53*, and *CHEK2* germline mutations in uterine serous carcinoma. *Cancer* 2013; 119: 332-8.
 29. Yemelyanova A, Vang R, Kshirsagar M, *et al.* Immunohistochemical staining patterns of p53 can serve as a surrogate marker for *TP53* mutations in ovarian carcinoma: an immunohistochemical and nucleotide sequencing analysis. *Mod Pathol* 2011; 24: 1248-53.
 30. Martinez ME, Wertheim BC, Natarajan L, *et al.* Reproductive factors, heterogeneity, and breast tumor subtypes in women of mexican descent. *Cancer Epidemiol Biomarkers Prev* 2013; 22: 1853-61.
 31. Song N, Choi JY, Sung H, *et al.* Heterogeneity of epidemiological factors by breast tumor subtypes in Korean women: a case-case study. *Int J Cancer* 2014; 135: 669-81.
 32. Ismail SM. Pathology of endometrium treated with tamoxifen. *J Clin Pathol* 1994; 47: 827-33.
 33. Swerdlow AJ, Jones ME; For the British Tamoxifen Second Cancer Study Group. Tamoxifen treatment for breast cancer and risk of endometrial cancer: a case-control study. *J Natl Cancer Inst* 2005; 97: 375-84.
 34. Vasconcelos AL, Nunes B, Duarte C, *et al.* Tamoxifen in breast cancer ipse dixit in uterine malignant mixed Mullerian tumor and sarcoma: a report of 8 cases and review of the literature. *Rep Pract Oncol Radiother* 2013; 18: 251-60.
 35. McInnes KJ, Andersson TC, Simonyte K, *et al.* Association of 11beta-

- hydroxysteroid dehydrogenase type I expression and activity with estrogen receptor beta in adipose tissue from postmenopausal women. *Menopause* 2012; 19: 1347-52.
36. Thomas C, Gustafsson JA. A CUE hints at tumor resistance. *Nat Med* 2011; 17: 658-60.
37. Bado I, Nikolos F, Rajapaksa G, Gustafsson JÅ, Thomas C. ERbeta decreases the invasiveness of triple-negative breast cancer cells by regulating mutant p53 oncogenic function. *Oncotarget* 2016; 7: 13599-611.

Prognostic Impact of *Fusobacterium nucleatum* Depends on Combined Tumor Location and Microsatellite Instability Status in Stage II/III Colorectal Cancers Treated with Adjuvant Chemotherapy

Hyeon Jeong Oh¹ · Jung Ho Kim¹
Jeong Mo Bae¹ · Hyun Jung Kim²
Nam-Yun Cho²
Gyeong Hoon Kang^{1,2}

¹Department of Pathology, Seoul National University Hospital, Seoul National University College of Medicine, Seoul; ²Laboratory of Epigenetics, Cancer Research Institute, Seoul National University College of Medicine, Seoul, Korea

Received: July 20, 2018
Revised: November 9, 2018
Accepted: November 29, 2018

Corresponding Author

Jung Ho Kim, MD, PhD
Department of Pathology, Seoul National University Hospital, 101 Daehak-ro, Jongno-gu, Seoul 03080, Korea
Tel: +82-2-2072-2828
Fax: +82-2-743-5530
E-mail: junghokim@snuh.org

Gyeong Hoon Kang, MD, PhD
Department of Pathology, Seoul National University College of Medicine, 103 Daehak-ro, Jongno-gu, Seoul 03080, Korea
Tel: +82-2-740-8263
Fax: +82-2-765-5600
E-mail: ghkang@snu.ac.kr

Background: This study aimed to investigate the prognostic impact of intratumoral *Fusobacterium nucleatum* in colorectal cancer (CRC) treated with adjuvant chemotherapy. **Methods:** *F. nucleatum* DNA was quantitatively measured in a total of 593 CRC tissues retrospectively collected from surgically resected specimens of stage III or high-risk stage II CRC patients who had received curative surgery and subsequent oxaliplatin-based adjuvant chemotherapy (either FOLF-*OX* or CAPOX). Each case was classified into one of the three categories: *F. nucleatum*-high, -low, or -negative. **Results:** No significant differences in survival were observed between the *F. nucleatum*-high and -low/negative groups in the 593 CRCs ($p = .671$). Subgroup analyses according to tumor location demonstrated that disease-free survival was significantly better in *F. nucleatum*-high than in -low/negative patients with non-sigmoid colon cancer (including cecal, ascending, transverse, and descending colon cancers; $n = 219$; log-rank $p = .026$). In multivariate analysis, *F. nucleatum* was determined to be an independent prognostic factor in non-sigmoid colon cancers (hazard ratio, 0.42; 95% confidence interval, 0.18 to 0.97; $p = .043$). Furthermore, the favorable prognostic effect of *F. nucleatum*-high was observed only in a non-microsatellite instability-high (non-MSI-high) subset of non-sigmoid colon cancers (log-rank $p = 0.014$), but not in a MSI-high subset (log-rank $p = 0.844$), suggesting that the combined status of tumor location and MSI may be a critical factor for different prognostic impacts of *F. nucleatum* in CRCs treated with adjuvant chemotherapy. **Conclusions:** Intratumoral *F. nucleatum* load is a potential prognostic factor in a non-MSI-high/non-sigmoid/non-rectal cancer subset of stage II/III CRCs treated with oxaliplatin-based adjuvant chemotherapy.

Key Words: Colorectal neoplasms; *Fusobacterium*; Gastrointestinal microbiome; Prognosis

Accumulating evidence has implicated the gut microbiota as having various roles in carcinogenesis, prognosis, and treatment response of colorectal cancer (CRC).¹⁻⁵ Among the gut microbiota, *Fusobacterium nucleatum* has been identified as a specifically enriched species within the tumor tissue of human CRC.^{6,7} Although *F. nucleatum* composes a relatively small proportion of the normal intestinal flora, the amount of tumor-invasive *F. nucleatum* was reported to be remarkably increased in a subset of CRC cases.^{6,9}

In the colorectal carcinogenesis pathway, the amount of invasive *F. nucleatum* gradually increases from premalignant adenoma-

tous lesions to carcinomas in the large intestine.⁹⁻¹¹ Among the premalignant colorectal lesions, sessile serrated adenomas have been suggested to be closely correlated with *F. nucleatum* enrichment.^{9,10} Therefore, it has been suspected that *F. nucleatum* might have roles in the serrated carcinogenesis pathway of the colorectum. However, detailed mechanisms of the increase of invasive *F. nucleatum* abundance and pathobiological implications of *F. nucleatum* in the serrated pathway are unclear. Experimental data indicate that *F. nucleatum* might have carcinogenic roles through the modulation of the E-cadherin/ β -catenin signaling pathway and/or promotion of the pro-inflammatory micro-

environment.^{1,2} However, these biological mechanisms cannot fully explain the basis of the association of *F. nucleatum* with the serrated pathway in CRC.

The findings using clinical samples support the suggestion that a high load of intratumoral *F. nucleatum* is associated with various clinicopathological and molecular features of CRC, including right-sided tumor location, poor prognosis, poor response to chemotherapy, low density of CD3⁺ tumor-infiltrating lymphocytes, high density of tumor-infiltrating macrophages, CpG island methylator phenotype (CIMP), and microsatellite instability (MSI).^{3,4,8,12-14} However, these observed associations of *F. nucleatum* in CRC are less robust, since the results were derived from limited study cohorts. Thus, precise clinicopathological and molecular implications of *F. nucleatum*–high CRC need to be elucidated and validated using additional independent data.

Recent studies reported that the gut microbiota is associated with responses to chemotherapy and immunotherapy in solid tumors.^{4,5,15-17} Especially, Yu *et al.*⁴ reported that *F. nucleatum* can promote chemoresistance in CRC by modulating the Toll-like receptor, micro-RNAs, and autophagy pathways. Based on these results, we designed a study to investigate the prognostic impacts of *F. nucleatum* in CRC patients treated with adjuvant chemotherapy. The amount of intratumoral *F. nucleatum* and its prognostic associations were analyzed in a total of 593 stage III or high-risk stage II CRCs treated with adjuvant FOLFOX (folinic acid/5-fluorouracil plus oxaliplatin) or CAPOX (capecitabine plus oxaliplatin) chemotherapy.

MATERIALS AND METHODS

Case selection

Formalin-fixed, paraffin-embedded (FFPE) tissues of 747 consecutive series of primary CRCs were collected from the pathology archive of Seoul National University Hospital, Seoul, Korea. All the tissues were from surgical specimens of patients who underwent curative surgery and subsequent adjuvant chemotherapy for stage III or high-risk stage II CRC at Seoul National University Hospital from 2005 to 2012. The inclusion criteria for the case selection were age greater than 18 years, adenocarcinoma histology without neuroendocrine or squamous cell component, stage III or high-risk stage II according to pathological staging, complete resection (R0) of the primary tumor with tumor-free resection margins, and the completion of at least six cycles of adjuvant FOLFOX chemotherapy or four cycles of adjuvant CAPOX therapy. The criteria for high-risk stage II were tumor invasion into visceral peritoneum or direct invasion into adjacent

organs/structures (pT4), clinically obstruction or perforation, poorly differentiated or undifferentiated histology (G3/G4), lymphovascular invasion, and perineural invasion. The patients who received pre-operative neoadjuvant chemotherapy and/or radiotherapy (especially patients with rectal cancer) and patients with a history of other malignancy within 5 years were excluded. Initially, 747 cases were subjected to quantitative polymerase chain reaction (qPCR) analysis for *F. nucleatum*. Among them, 154 inadequate samples determined by invalid or poor quality results from the qPCR analysis, as described subsequently, were excluded. Finally, a total of 593 CRC cases were analyzed. The Institutional Review Board of our hospital approved this study (IRB No. 1805-018-944). The Institutional Review Board exempted our study from obtaining informed consent from patients because our study was a retrospective, anonymous, tissue-based investigation.

Clinicopathological data

Clinical data, including age, sex, tumor location, and gross tumor type, were collected from electronic medical records. Hematoxylin and eosin-stained tissue slides of each case were independently reviewed by pathologists (J.M.B. and G.H.K.) to evaluate histopathological features, including pT/pN categories, tumor grade, lymphovascular invasion, perineural invasion, and mucinous histology.

qPCR for *F. nucleatum*

Genomic DNA extraction from FFPE tissues of the 747 CRCs and qPCR for *F. nucleatum*, using the 747 tumor DNA samples, were conducted as previously described.¹⁴ In brief, the following primers and probes targeting the 16S rRNA gene DNA sequence of *F. nucleatum* and the reference gene (prostaglandin transporter, PGT), were used: *F. nucleatum* forward primer, 5'-CAACCAT-TACTTTAACTCTACCATGTTCA-3'; *F. nucleatum* reverse primer, 5'-GTTGACTTTACAGAAGGAGATTATGTA-AAAATC-3'; *F. nucleatum* FAM probe, 5'-GTTGACTTTA-CAGAAGGAGATTA-3'; PGT forward primer, 5'-ATCCCCAAAGCACCTGGTTT-3'; PGT reverse primer, 5'-AGAGGC-CAAGATAGTCCTGGTAA-3'; PGT VIC probe, 5'-CCATC-CATGTCCTCATCTC-3'.¹⁴ The PCR conditions were 95°C for 10 minutes followed by 45 cycles of 95°C for 15 seconds, and 60°C for 1 minute.¹⁴ To compare the *F. nucleatum* DNA amounts between tumor DNA samples, the relative values ($2^{-\Delta C_t}$) calculated from the threshold cycle (Ct) values for *F. nucleatum* normalized to PGT were used. The qPCR method was validated using serially-diluted *F. nucleatum* genomic DNA samples (25586D-5;

ATCC, Manassas, VA, USA). The results of the validation analysis are summarized in Supplementary Fig. S1. *F. nucleatum*-positive CRCs were further classified into two subgroups (*F. nucleatum*-high or *F. nucleatum*-low) using a cut-off median value of $2^{-\Delta C_t}$. Among the samples of the initial 747 cases subjected to *F. nucleatum* qPCR analysis, those of 154 cases were determined as failed or inadequate, based on non-evaluable or high Ct values of PGT. Thus, 593 cases were finally included in this study. The qPCR experiment of each sample was performed independently in triplicate.

DNA analyses for MSI, CIMP, KRAS, and BRAF

Major molecular factors, including MSI, CIMP, and *KRAS*/*BRAF* mutations, in the CRC samples were analyzed as previously described.¹⁸ Genomic DNA of each tumor was isolated from representative FFPE tissue blocks by microdissection. MSI testing was performed by DNA fragment analysis using five microsatellite markers (BAT-25, BAT-26, D5S346, D17S250, and D2S123) according to the Bethesda guideline.¹⁹ MSI status of each case was classified into one of the three categories: MSI-high, MSI-low, and microsatellite stable (MSS). CIMP analysis was carried out by the real-time PCR-based MethyLight assay using eight CIMP markers (*MLH1*, *NEUROG1*, *CRABP1*, *CACNA1G*, *CDKN2A*, *IGF2*, *SOCS1*, and *RUNX3*) as previously described.¹⁸ CIMP status of each case was classified into one of the three cat-

egories: CIMP-high, CIMP-low, and CIMP-negative. Mutational status of *KRAS* exon 2 codons 12 and 13 and *BRAF* exon 15 codon 600 were examined by Sanger sequencing.

Statistical analyses

All statistical analyses in this study were performed using SPSS ver. 23 (IBM Corp., Armonk, NY, USA). Comparison analysis between categorical variables was conducted using chi-square test or Fisher exact test. Univariate and multivariate survival analyses were carried out using the Kaplan-Meier method with log-rank test and Cox proportional hazards regression model. All p-values were considered to indicate statistically significant differences if less than 0.05.

RESULTS

Variable amounts of *F. nucleatum* according to tumor location bowel subsite in CRCs

Among the 593 stage II/III CRCs treated with oxaliplatin-based adjuvant chemotherapy (FOLFOX or CAPOX), intratumoral *F. nucleatum* DNA was detected in 408 cases (68.8%). Each *F. nucleatum*-positive CRC was classified as *F. nucleatum*-high or -low based on *F. nucleatum* DNA load, using a cut-off median value of $2^{-\Delta C_t}$. The proportions of *F. nucleatum*-high, -low, and -negative CRCs along the tumor location bowel subsite varied

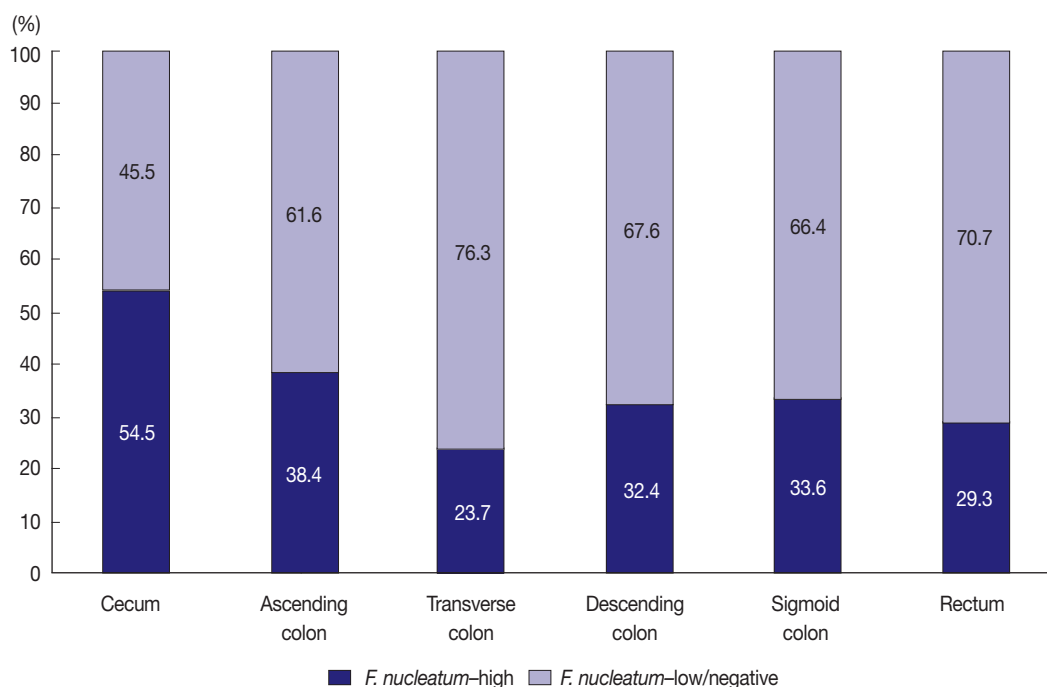


Fig. 1. Different proportions of *Fusobacterium nucleatum*-high vs *F. nucleatum*-low/negative colorectal cancers according to tumor location bowel subsites.

(Fig. 1). The proportion of *F. nucleatum*-high tumors was highest among cecal cancers, whereas that of *F. nucleatum*-high tumors was lowest among transverse colon cancers (54.5% and 23.7%, respectively) (Fig. 1).

Clinicopathological and molecular associations of *F. nucleatum* in CRCs

We analyzed the relationship between *F. nucleatum* status (high vs. low/negative) and clinicopathological (age, sex, tumor sidedness, pT/pN categories, tumor grade, lymphovascular and perineural invasions, and mucinous histology) and molecular characteristics (MSI, CIMP, and *KRAS/BRAF* mutations) in overall stage II/III CRCs treated with oxaliplatin-based adjuvant chemotherapy (n = 593). The results are summarized in Table 1. Among the variables, the pT category was the only factor with statistical significance. *F. nucleatum*-high was significantly associated with advanced pT stage (pT3/pT4) (p = .005) (Table 1). CIMP-high and *KRAS* mutations were more frequent in *F. nucleatum*-high CRCs than in *F. nucleatum*-low/negative CRCs, without statistical significance (p = .174 and p = .093, respectively) (Table 1).

Prognostic impact of *F. nucleatum* in CRCs treated with adjuvant chemotherapy

In survival analysis, no significant difference in disease-free survival (DFS) was evident between the *F. nucleatum* high and *F. nucleatum* low/negative groups in overall 593 stage II/III CRC patients treated with oxaliplatin-based adjuvant chemotherapy (log-rank p = .671) (Fig. 2A). In addition, the prognostic significance of *F. nucleatum* was not identified in subgroups stratified by MSI status (log-rank p = .858 in MSI-high CRCs (n = 40), log-rank p = .625 in MSS/MSI-low CRCs (n = 545) (Supplementary Fig. S2). However, subgroup analyses according to tumor location demonstrated that DFS of the *F. nucleatum*-high group was significantly better than that of the *F. nucleatum*-low/negative group in patients with adjuvant FOLFOX or CAPOX-treated colon cancer located in the non-sigmoid colon (from cecum to descending colon, n = 219) (log-rank p = .026) (Fig. 2B). In sigmoid colon and rectal cancer patients treated with oxaliplatin-based adjuvant chemotherapy (n = 374), the *F. nucleatum*-high group showed a tendency toward worse DFS compared to the *F. nucleatum*-low/negative group, but this survival difference was not statistically significant (log-rank p = .199) (Fig. 2C). In multivariate analysis, *F. nucleatum*-high was an independently favorable prognostic factor in non-sigmoid colon cancer patients treated with oxaliplatin-based adjuvant chemotherapy (hazard ratio, 0.42; 95% confidence interval, 0.18 to 0.97; p = .043) (Table 2).

Table 1. Characteristics of adjuvant chemotherapy-treated, stage II/III CRCs according to the *Fusobacterium nucleatum* status

Variable	F. nucleatum-high	F. nucleatum-low/negative	p-value
Age			.286
Younger (<59 yr)	84 (41.2)	178 (45.8)	
Older (≥59 yr)	120 (58.8)	211 (54.2)	
Sex			.925
Male	124 (60.8)	238 (61.2)	
Female	80 (39.2)	151 (38.8)	
Tumor sidedness			.287
Right-sided	69 (33.8)	115 (29.6)	
Left-sided	135 (66.2)	274 (70.4)	
Gross tumor type			.243
Polypoid/fungating	119 (58.3)	246 (63.2)	
Ulceroinfiltrative	85 (41.7)	143 (36.8)	
pT category			.005
pT1/pT2	9 (4.4)	44 (11.3)	
pT3/pT4	195 (95.6)	345 (88.7)	
pN category			.464
pN0	34 (16.7)	56 (14.4)	
pN1/pN2	170 (83.3)	333 (85.6)	
Tumor histological grade			.687
G1/G2	188 (92.2)	362 (93.1)	
G3/G4	16 (7.8)	27 (6.9)	
Lymphovascular invasion			.419
Absent	112 (54.9)	200 (51.4)	
Present	92 (45.1)	189 (48.6)	
Perineural invasion			.171
Absent	143 (70.1)	293 (75.3)	
Present	61 (29.9)	96 (24.7)	
Mucinous histology			.269
Absent	184 (90.2)	361 (92.8)	
Present	20 (9.8)	28 (7.2)	
MSI status ^a			.647
MSS/MSI-low	185 (92.5)	360 (93.5)	
MSI-high	15 (7.5)	25 (6.5)	
CIMP status ^b			.174
CIMP-low/negative	189 (92.6)	369 (95.3)	
CIMP-high	15 (7.4)	18 (4.7)	
<i>KRAS</i> mutation ^c			.093
Absent	137 (67.2)	286 (73.7)	
Present	67 (32.8)	102 (26.3)	
<i>BRAF</i> mutation			.213
Absent	200 (98)	374 (96.1)	
Present	4 (2)	15 (3.9)	

Values are presented as number (%). CRC, colorectal cancer; G1, grade 1 (well differentiated); G2, grade 2 (moderately differentiated); G3, grade 3 (poorly differentiated); G4, grade 4 (undifferentiated); MSI, microsatellite instability; MSS, microsatellite-stable; CIMP, CpG island methylator phenotype. ^aAmong the 593 cases, MSI status could not be determined in eight cases due to inadequate DNA quality or quantity; ^bAmong the 593 cases, CIMP status could not be determined in two cases due to inadequate DNA quality or quantity; ^cAmong the 593 cases, *KRAS* mutation could not be determined in one case due to inadequate DNA quality or quantity.

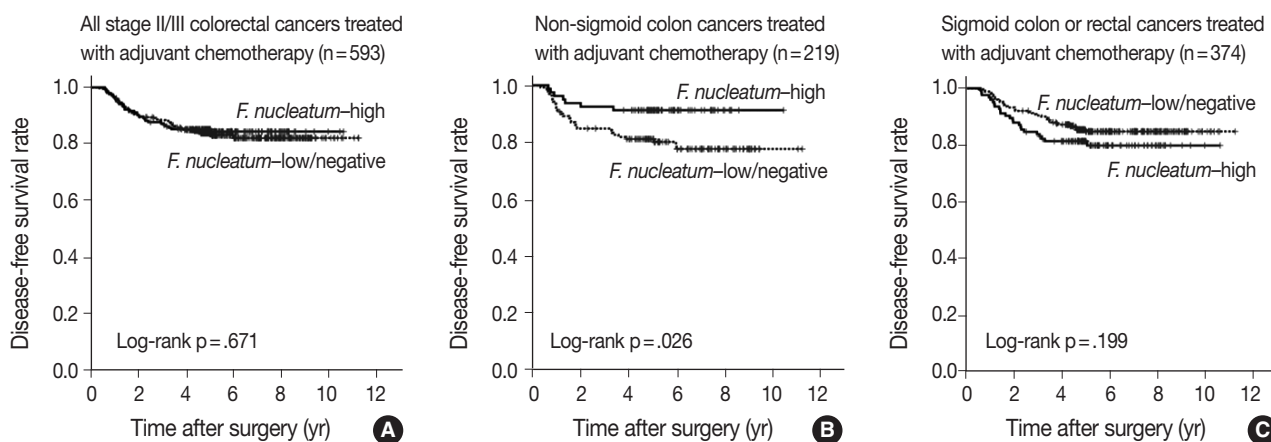


Fig. 2 . Kaplan-Meier survival analysis, including subgroup analysis according to tumor location. (A) No significant difference in disease-free survival was evident between *Fusobacterium nucleatum*-high and -low/negative subgroups in the overall 593 stage II/III colorectal cancer patients treated with oxaliplatin-based adjuvant chemotherapy. (B) The *F. nucleatum*-high subgroup was significantly associated with better disease-free survival in non-sigmoid colon cancer patients treated with oxaliplatin-based adjuvant chemotherapy (n=219). (C) In sigmoid colon and rectal cancer patients treated with oxaliplatin-based adjuvant chemotherapy (n=374), the *F. nucleatum*-high subgroup shows a tendency toward worse disease-free survival without statistical significance.

To further identify the molecular basis of the favorable prognostic effect of *F. nucleatum* observed in non-sigmoid colon cancers, we analyzed the prognostic impact of *F. nucleatum* in subsets of non-sigmoid colon cancer patients according to MSI status. In an MSS/MSI-low subset of non-sigmoid colon cancer patients treated with adjuvant chemotherapy (n = 185), DFS was significantly better in the *F. nucleatum*-high group than in the *F. nucleatum*-low/negative group (log-rank p = .014) (Fig. 3A). However, significant DFS difference according to *F. nucleatum* status was not observed in an MSI-high subset of non-sigmoid colon cancer patients (n = 31) (log-rank p = .844) (Fig. 3B). Finally, survival analyses in MSS/MSI-low (n = 360) and MSI-high (n = 9) subgroups of sigmoid colon or rectal cancers treated with oxaliplatin-based adjuvant chemotherapy demonstrated tendencies toward worse DFS of *F. nucleatum*-high group than of *F. nucleatum*-low/negative group, but there was no statistical significance (log-rank p = .193 in MSS/MSI-low subgroup, Fig. 3C; log-rank p = .885 in MSI-high subgroup, Fig. 3D)

DISCUSSION

Direct or indirect roles of gut microbiota in the pathogenesis of a variety of human diseases have been recently proposed. The demonstration of the close association between *F. nucleatum* and CRC has prompted exploration of the pathogenetic, prognostic, and predictive roles of *F. nucleatum* in CRC. However, there are still limited data regarding the prognostic and predictive values of *F. nucleatum* in CRC. Several studies using clinical samples

have indicated that intratumoral *F. nucleatum* is potentially associated with poor prognosis in CRC patients.^{3,11,20} Moreover, an experimental study suggested that *F. nucleatum* might be able to induce resistance to chemotherapy by modulating autophagy in CRC cells.⁴ Based on the emerging prognostic significance and potential predictive value of *F. nucleatum* in CRC, we decided to investigate the prognostic relevance of *F. nucleatum* in CRCs treated with adjuvant chemotherapy. Most patients with stage III or high-risk stage II CRC are treated with adjuvant chemotherapy after curative surgery to prevent tumor recurrence. Thus, we collected a large series of stage III or high-risk stage II CRCs treated with oxaliplatin-based adjuvant chemotherapy. The survival differences in patient subgroups according to DNA amount of intratumoral *F. nucleatum* measured by qPCR were statistically analyzed. We found that a high load of intratumoral *F. nucleatum* was independently correlated with improved survival in patients with stage II/III non-sigmoid colon cancer treated with oxaliplatin-based adjuvant chemotherapy (Table 2).

There is a discrepancy between our research and previous studies. Several previous studies revealed that *F. nucleatum*-high CRC patients group tended to have shorter disease-specific survival than *F. nucleatum*-low/negative CRC patients group.^{3,11,20} However, in the current study, *F. nucleatum* had different prognostic impacts based on tumor location in CRCs treated with adjuvant chemotherapy. In detail, tumors with high levels of *F. nucleatum* had better prognosis than those with low or negative levels of *F. nucleatum* in non-sigmoid colon cancers, including cecum, ascending colon, transverse colon, and descending colon

Table 2. Univariate and multivariate survival analyses of patients with stage II/III non-sigmoid colon cancer treated with oxaliplatin-based adjuvant chemotherapy (n=219)

Variable	No.	Univariate analysis HR (95% CI)	p-value	Multivariate analysis HR (95% CI)	p-value
<i>F. nucleatum</i>					
<i>F. nucleatum</i> –low/negative	139	Reference		Reference	
<i>F. nucleatum</i> –high	80	0.4 (0.18–0.92)	.031	0.42 (0.18–0.97)	.043
pT category					
pT1/pT2/pT3	183	Reference		Reference	
pT4	36	5.13 (2.65–9.92)	<.001	5.04 (2.53–10.07)	<.001
pN category					
pN0/pN1	176	Reference		Reference	
pN2	43	2.88 (1.47–5.64)	.002	2.65 (1.31–5.35)	.007
Lymphovascular invasion					
Absent	129	Reference		Reference	
Present	90	2.78 (1.41–5.50)	.003	1.39 (0.66–2.95)	.387
Perineural invasion					
Absent	169	Reference		Reference	
Present	50	2.81 (1.45–5.45)	.002	2.92 (1.41–6.05)	.004
BRAF mutation					
Absent	204	Reference		Reference	
Present	15	3.12 (1.30–7.49)	.011	2.21 (0.86–5.69)	.1
Tumor histological grade					
G1/G2	190	Reference		-	
G3/G4	29	1.14 (0.44–2.92)	.791	-	-
MSI status ^a					
MSS/MSI-low	185	Reference		-	
MSI-high	31	0.57 (0.17–1.87)	.353	-	-
CIMP status ^b					
CIMP-low/negative	192	Reference		-	
CIMP-high	25	1.32 (0.51–3.40)	.567	-	-
KRAS mutation ^c					
Absent	148	Reference		-	
Present	71	0.93 (0.46–1.89)	.844	-	-

HR, hazard ratio; 95% CI, 95% confidence interval of HR; G1, grade 1 (well differentiated); G2, grade 2 (moderately differentiated); G3, grade 3 (poorly differentiated); G4, grade 4 (undifferentiated); MSI, microsatellite instability; MSS, microsatellite-stable; CIMP, CpG island methylator phenotype.

^aAmong the 219 cases, MSI status could not be determined in three cases due to inadequate DNA quality or quantity; ^bAmong the 219 cases, CIMP status could not be determined in two cases due to inadequate DNA quality or quantity.

cancers (Table 2, Fig. 2B). On the other hand, *F. nucleatum*–high CRCs showed a tendency toward worse prognosis compared to *F. nucleatum*–low/negative CRCs in sigmoid colon and rectal cancers (Fig. 2C). Since these contrasting prognostic implications of *F. nucleatum* according to tumor location may counterbalance the overall prognostic effect of *F. nucleatum* in CRCs, presently *F. nucleatum* displayed no association with prognosis in a total of 593 stage II/III CRC patients treated with adjuvant chemotherapy (Fig. 2A). The reason for the discrepancy between the current and prior findings may be the difference in the composition of the study populations. Yamaoka *et al.*²⁰ described that *F. nucleatum* was highly correlated with shorter disease specific survival especially in stage IV CRCs. In that study, in all stages of CRCs, disease-specific survival was decreased in CRCs featuring a high level of

F. nucleatum compared with that in CRCs with low levels of *F. nucleatum*, although the survival differences according to *F. nucleatum* level was decreased compared to that in the stage IV CRC subgroup.²⁰ In addition, it cannot be excluded that there might be heterogeneities of detailed treatment approaches, such as adjuvant chemotherapy regimen, in the CRC cohorts of other studies. By contrast, our study samples were a well-selected and relatively-homogeneous cohort that contained only stage III or high-risk stage II CRCs treated with oxaliplatin-based adjuvant chemotherapy. Therefore, the prognostic implications of *F. nucleatum* in CRC that is evident from our study could be meaningfully different from the results of other research groups.

In an experimental study, *F. nucleatum* promoted resistance to chemotherapy in CRC cells.⁴ However, our results indicate that

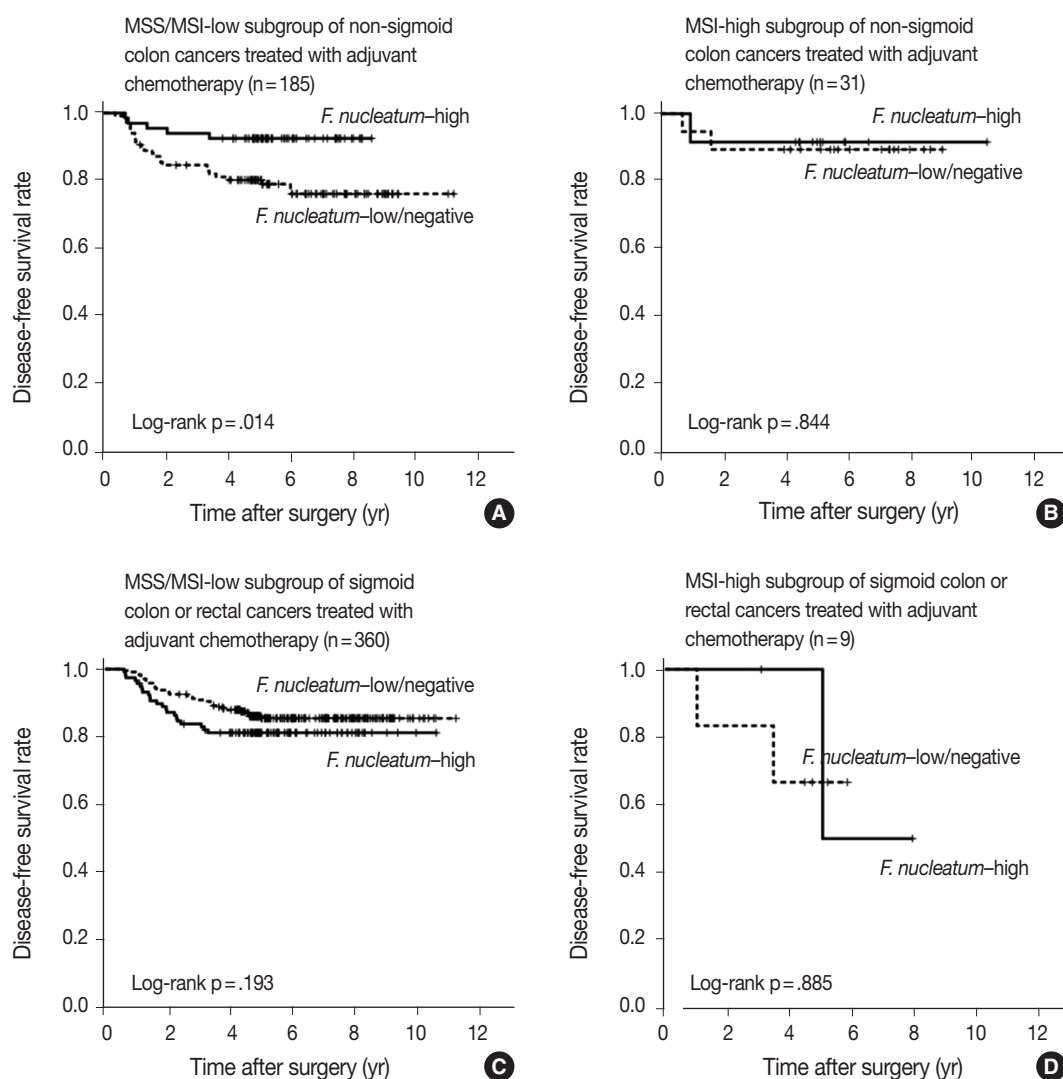


Fig. 3. Kaplan-Meier survival analysis, including subgroup analysis according to combined tumor location and microsatellite instability (MSI) status. (A) The *Fusobacterium nucleatum*-high subgroup was significantly associated with better disease-free survival in an MSS/MSI-low subset of non-sigmoid colon cancer patients treated with oxaliplatin-based adjuvant chemotherapy (n=185). (B) No significant survival difference according to *F. nucleatum* status was observed in an MSI-high subset of non-sigmoid colon cancer patients treated with oxaliplatin-based adjuvant chemotherapy (n=31). (C) There is a tendency toward worse survival in the *F. nucleatum*-high subgroup without statistical significance in an MSS/MSI-low subset of sigmoid colon or rectal cancer patients treated with oxaliplatin-based adjuvant chemotherapy (n=360). (D) No significant survival difference according to *F. nucleatum* status was observed in an MSI-high subset of sigmoid colon or rectal cancer patients treated with oxaliplatin-based adjuvant chemotherapy (n=9).

influences of *F. nucleatum* on responses to chemotherapy might be diverse in the context of tumor location of CRCs. In sigmoid colon and rectal cancers, the expected chemoresistant effect of *F. nucleatum* seems to have occurred because *F. nucleatum*-high was linked with poor prognosis in sigmoid colon and rectal cancer patients treated with adjuvant chemotherapy, although statistical significance was not reached (Fig. 2C). Nevertheless, in non-sigmoid colon cancers, a chemoresistant role of *F. nucleatum* seems to be attenuated. Rather, *F. nucleatum* might induce a chemoresponsive effect because *F. nucleatum*-high was significantly asso-

ciated with favorable prognosis in non-sigmoid colon cancers treated with adjuvant chemotherapy (Table 2, Fig. 2B). The underlying mechanism of the potential contrasting effects of *F. nucleatum* on the chemotherapy response depending on location of CRC is unclear. However, the idea that different tumor locations can define different prognosis and treatment responses in CRC has been increasingly addressed. In fact, based on the accumulating clinical data, primary tumor location is regarded as a prognostic factor in metastatic CRCs.²¹ Stage IV CRCs primarily located in the right-sided colon are significantly associated with worse prognosis

compared with left-sided stage IV CRCs. The different molecular, pathological, and clinical features between right-sided colon cancers and left-sided CRCs have been reported.^{21,22} Therefore, the potential different impacts of *F. nucleatum* on prognosis and treatment responses according to tumor location in CRCs are not surprising. To the best of our knowledge, this study is the first report to investigate the prognostic effect of *F. nucleatum* according to tumor location in CRCs, especially in adjuvant chemotherapy-treated CRCs. Our study suggests that the prognostic effect of *F. nucleatum* should be evaluated considering the location of the tumor.

In this study, the proportion of *F. nucleatum*-high CRCs differed in each tumor location bowel subsite. The proportion of *F. nucleatum*-high tumors in all the CRCs was 34.4% (204 of 593). Cecal cancers displayed the highest proportion of *F. nucleatum*-high tumors (54.5%), followed by ascending colon cancers (38.4%) (Fig. 1). It was notable that over half of the cecal cancers were *F. nucleatum*-high tumors. Our results are consistent with those of previous studies demonstrating the significant association of the proximal location of CRCs with a high level of intratumoral *F. nucleatum*. According to the study by Mima *et al.*,¹³ the proportion of *F. nucleatum*-high CRCs increased along the distance from the anal verge, and cecal cancers showed the highest proportion of *F. nucleatum*-high subtype. The underlying mechanism of the specific enrichment of *F. nucleatum* in cecal and ascending colon cancers is still unclear, but microenvironmental or biological factors specifically found in the cecal to ascending colon areas could influence the increase of intratumoral *F. nucleatum*. For example, bacterial biofilms are intensively enriched in right-sided colon tumors compared with those in left-sided colorectal tumors.²³ Based on recent experimental findings, potential molecular mechanisms can be hypothesized. According to a previous experimental study, *F. nucleatum* is enriched in colorectal tumor tissue by Fap2 binding to Gal-GalNAc expressed on tumor cells.²⁴ Thus, it can be hypothesized that Gal-GalNAc expression on tumor cells might be more upregulated in the right-sided colon than in the left-sided colon. Further investigations are needed to elucidate the biological reason of the preference of invasive *F. nucleatum* for right-sided colon cancers.

According to the recent data reported by Ogino group, *F. nucleatum* in CRCs differentially impacts tumor-infiltrating lymphocyte (TIL) density depending on MSI status.²⁵ In detail, there was an inverse association between *F. nucleatum* load and TIL density in MSI-high CRCs, whereas a positive correlation between *F. nucleatum* load and TIL density was observed in non-MSI-high CRCs.²⁵ This finding can provide an important clue for the interpretation of our present results. It has been validated

that high TIL density is strongly associated with favorable prognosis in CRCs.²⁶ Thus, because *F. nucleatum*-high tumors might be associated with increased antitumor immunity and subsequent improved prognosis in non-MSI-high CRCs, the favorable prognostic effect of *F. nucleatum*-high in the MSS/MSI-low subset of non-sigmoid colon cancers, which was observed in our present study, could be a reasonable finding. However, we also found that the prognostic significance of *F. nucleatum* was valid only in non-sigmoid colon cancers, but not in sigmoid colon/rectal cancers, suggesting that both tumor location and MSI status should be concurrently considered for understanding the prognostic implications of *F. nucleatum* in CRCs.

There have been several reports regarding the poor prognostic effect of *F. nucleatum* in CRCs, which was mainly observed in Western CRC cohorts or stage IV CRC cohorts.^{3,20,27} However, our present data indicate that high intratumoral *F. nucleatum* load might be associated with favorable prognosis in a limited subgroup of CRCs, a MSS/MSI-low subset of non-sigmoid colon cancers. We suspect that different compositions of tumor locations and MSI subtypes in CRC cohorts might influence the different prognostic effects of *F. nucleatum* in overall CRCs. Because it has been known that the frequency of MSI-high in CRCs is definitely lower in East Asia countries than in Western countries,²⁸ the potential favorable prognostic effect of *F. nucleatum* in proximal colonic-located, non-MSI-high CRCs might be significantly attenuated in CRC cohorts of Western countries, which consist of relatively high numbers of MSI-high tumors. Instead, both the tendency toward worse prognosis of *F. nucleatum*-high in MSI-high tumors (Supplementary Fig. S2A) and the potential poor prognostic effect of *F. nucleatum*-high tumors observed in sigmoid colon/rectal cancers (Fig. 2C) might augment the adverse prognostic impact of *F. nucleatum* in overall CRCs. To confirm this hypothesis, additional investigations using various CRC cohorts having different ethnic backgrounds would be needed. Regarding the poor prognostic feature of *F. nucleatum* in stage IV CRCs observed in a few studies,^{20,27} it could be explained by relatively high proportion of distal-located CRCs as primary origin of stage IV CRCs. Thus, the potential worse prognostic effect of *F. nucleatum* in sigmoid colon or rectal cancers might be augmented especially in a stage IV subset of CRCs.

Although significant associations between CIMP-high (and/or MSI-high) and *F. nucleatum* in CRCs were reported in several previous studies,^{3,8,9} significant correlation between *F. nucleatum*-high group and CIMP-high or MSI-high molecular subtype was not observed in our present study (Table 1). However, there was an evident tendency toward higher proportion of

CIMP-high tumors in *F. nucleatum*-high group than in *F. nucleatum*-low/negative group (7.4% vs. 4.7%) (Table 1). In addition, we performed mean comparison of *F. nucleatum* DNA amount ($2^{-\Delta C_t}$) between CIMP-high and CIMP-low/negative tumors, and the results indicated that mean *F. nucleatum* DNA amount was higher in CIMP-high tumors than in CIMP-low/negative tumors although statistical significance was not reached (0.986 vs. 0.367, $p = .157$) (Supplementary Fig. S3). The reason for unclear molecular association of *F. nucleatum* in our study samples may be explained by potential ethnic differences and biased sample composition. As mentioned above, the frequencies of MSI-high and CIMP-high in CRCs are lower in East Asian population than in Western population. If a high number of CIMP-high cases were included in our cohort, significant association between *F. nucleatum*-high and CIMP-high might have been observed. Moreover, our study samples were confined to selected stage III or high-risk stage II CRCs treated with adjuvant chemotherapy. Thus, molecular compositions of our CRC cohort were possibly biased. For example, the CIMP-high/non-MSI-high subtype has been known as an aggressive phenotype of CRCs and can be more enriched in stage IV tumors. Because stage IV cases were excluded from our study samples, the potential association between *F. nucleatum*-high and CIMP-high could be weakened. Considering that data are limited, the relationship between *F. nucleatum* and specific molecular phenotypes in CRCs has not been conclusive yet. Therefore, further clinical and experimental investigations are needed to elucidate whether CIMP-high and/or MSI-high molecular phenotype can significantly interact with intratumoral *F. nucleatum* enrichment in CRCs.

The proportion of *F. nucleatum*-positive cases in CRCs by qPCR analysis has been variable according to different investigations (8.6%–74%).²⁹ In our results, *F. nucleatum* DNA was detected in 408 out of 593 cases (68.8%). The reason for variability in the *F. nucleatum*-positive rate in CRCs is unclear, but tissue quality might be a critical factor for this discrepancy. Recently, Lee *et al.*²⁷ found that the tissue fixation method could affect different results of *F. nucleatum* qPCR analysis. We also found that when the FFPE tissues were more recent, the positive rate of *F. nucleatum* was increased (unpublished data). Therefore, it can be inferred that *F. nucleatum*-positive rate by qPCR method could be variable, depending on tissue fixation method and tissue storage time.

There are several limitations in this study. First, we assessed the amount of *F. nucleatum* in genomic DNA samples extracted from FFPE tissues. The precise quantification of *F. nucleatum* could be disturbed owing to the degraded nature of DNA extract-

ed from FFPE tissues although a substantial number of previous studies that analyzed *F. nucleatum* in clinical CRC samples also used FFPE tissue-derived DNA. Second, our study cohort was retrospectively collected. The results from our study should be validated by other prospective studies.

In conclusion, the prognostic impact of *F. nucleatum* in CRCs treated with adjuvant chemotherapy may differ depending on the combined status of primary tumor location and MSI molecular phenotype. Intratumoral *F. nucleatum* load may be a potential prognostic factor in stage III or high-risk stage II non-sigmoid colon cancers treated with oxaliplatin-based adjuvant chemotherapy, especially in an MSS/MSI-low molecular subtype. There have been very limited data regarding the detailed prognostic implications of *F. nucleatum* in CRCs according to various clinicopathologic and molecular contexts. Therefore, further studies using large prospective cohorts will be necessary to validate the different location/MSI-dependent prognostic impacts of *F. nucleatum* in CRCs treated with adjuvant chemotherapy.

ORCID

Hyeon Jeong Oh: <https://orcid.org/0000-0002-9998-3988>

Jung Ho Kim: <https://orcid.org/0000-0002-6031-3629>

Jeong Mo Bae: <https://orcid.org/0000-0003-0462-3072>

Hyun Jung Kim: <https://orcid.org/0000-0002-8136-7095>

Nam-Yun Cho: <https://orcid.org/0000-0002-2126-9549>

Gyeong Hoon Kang: <https://orcid.org/0000-0003-2380-6675>

Electronic Supplementary Material

Supplementary materials are available at Journal of Pathology and Translational Medicine (<http://jpatholm.org>).

Conflicts of Interest

The authors declare that they have no potential conflicts of interest.

Acknowledgments

This study was supported by the National Research Foundation of Korea grant funded by the Korea government (Ministry of Science and ICT) (2016R1C1B2010627), a grant from the National Research Foundation of Korea grants funded by the Korea government (Ministry of Science and ICT) (2016M3A9B6026921), and a grant from the Korea Health Technology R&D Project through the Korea Health Industry Development Institute funded by the Korea government (Ministry of Health and Welfare) (HI14C1277).

REFERENCES

1. Kostic AD, Chun E, Robertson L, *et al.* *Fusobacterium nucleatum* potentiates intestinal tumorigenesis and modulates the tumor-immune microenvironment. *Cell Host Microbe* 2013; 14: 207-15.
2. Rubinstein MR, Wang X, Liu W, Hao Y, Cai G, Han YW. *Fusobacterium nucleatum* promotes colorectal carcinogenesis by modulating E-cadherin/beta-catenin signaling via its FadA adhesin. *Cell Host Microbe* 2013; 14: 195-206.
3. Mima K, Nishihara R, Qian ZR, *et al.* *Fusobacterium nucleatum* in colorectal carcinoma tissue and patient prognosis. *Gut* 2016; 65: 1973-80.
4. Yu T, Guo F, Yu Y, *et al.* *Fusobacterium nucleatum* promotes chemoresistance to colorectal cancer by modulating autophagy. *Cell* 2017; 170: 548-63.e16.
5. Geller LT, Barzily-Rokni M, Danino T, *et al.* Potential role of intratumor bacteria in mediating tumor resistance to the chemotherapeutic drug gemcitabine. *Science* 2017; 357: 1156-60.
6. Kostic AD, Gevers D, Pedamallu CS, *et al.* Genomic analysis identifies association of *Fusobacterium* with colorectal carcinoma. *Genome Res* 2012; 22: 292-8.
7. Castellarin M, Warren RL, Freeman JD, *et al.* *Fusobacterium nucleatum* infection is prevalent in human colorectal carcinoma. *Genome Res* 2012; 22: 299-306.
8. Tahara T, Yamamoto E, Suzuki H, *et al.* *Fusobacterium* in colonic flora and molecular features of colorectal carcinoma. *Cancer Res* 2014; 74: 1311-8.
9. Ito M, Kanno S, Noshio K, *et al.* Association of *Fusobacterium nucleatum* with clinical and molecular features in colorectal serrated pathway. *Int J Cancer* 2015; 137: 1258-68.
10. Yu J, Chen Y, Fu X, *et al.* Invasive *Fusobacterium nucleatum* may play a role in the carcinogenesis of proximal colon cancer through the serrated neoplasia pathway. *Int J Cancer* 2016; 139: 1318-26.
11. Flanagan L, Schmid J, Ebert M, *et al.* *Fusobacterium nucleatum* associates with stages of colorectal neoplasia development, colorectal cancer and disease outcome. *Eur J Clin Microbiol Infect Dis* 2014; 33: 1381-90.
12. Mima K, Sukawa Y, Nishihara R, *et al.* *Fusobacterium nucleatum* and T cells in colorectal carcinoma. *JAMA Oncol* 2015; 1: 653-61.
13. Mima K, Cao Y, Chan AT, *et al.* *Fusobacterium nucleatum* in colorectal carcinoma tissue according to tumor location. *Clin Transl Gastroenterol* 2016; 7: e200.
14. Park HE, Kim JH, Cho NY, Lee HS, Kang GH. Intratumoral *Fusobacterium nucleatum* abundance correlates with macrophage infiltration and CDKN2A methylation in microsatellite-unstable colorectal carcinoma. *Virchows Arch* 2017; 471: 329-36.
15. Routy B, Le Chatelier E, Derosa L, *et al.* Gut microbiome influences efficacy of PD-1-based immunotherapy against epithelial tumors. *Science* 2018; 359: 91-7.
16. Vetzou M, Pitt JM, Daillère R, *et al.* Anticancer immunotherapy by CTLA-4 blockade relies on the gut microbiota. *Science* 2015; 350: 1079-84.
17. Gopalakrishnan V, Spencer CN, Nezi L, *et al.* Gut microbiome modulates response to anti-PD-1 immunotherapy in melanoma patients. *Science* 2018; 359: 97-103.
18. Bae JM, Kim JH, Oh HJ, *et al.* Downregulation of acetyl-CoA synthetase 2 is a metabolic hallmark of tumor progression and aggressiveness in colorectal carcinoma. *Mod Pathol* 2017; 30: 267-77.
19. Boland CR, Thibodeau SN, Hamilton SR, *et al.* A National Cancer Institute Workshop on Microsatellite Instability for cancer detection and familial predisposition: development of international criteria for the determination of microsatellite instability in colorectal cancer. *Cancer Res* 1998; 58: 5248-57.
20. Yamaoka Y, Suehiro Y, Hashimoto S, *et al.* *Fusobacterium nucleatum* as a prognostic marker of colorectal cancer in a Japanese population. *J Gastroenterol* 2018; 53: 517-24.
21. Stintzing S, Tejpar S, Gibbs P, Thiebach L, Lenz HJ. Understanding the role of primary tumour localisation in colorectal cancer treatment and outcomes. *Eur J Cancer* 2017; 84: 69-80.
22. Bae JM, Kim JH, Kang GH. Molecular subtypes of colorectal cancer and their clinicopathologic features, with an emphasis on the serrated neoplasia pathway. *Arch Pathol Lab Med* 2016; 140: 406-12.
23. Dejea CM, Wick EC, Hechenbleikner EM, *et al.* Microbiota organization is a distinct feature of proximal colorectal cancers. *Proc Natl Acad Sci U S A* 2014; 111: 18321-6.
24. Abed J, Emgård JE, Zamir G, *et al.* Fap2 mediates *Fusobacterium nucleatum* colorectal adenocarcinoma enrichment by binding to tumor-expressed Gal-GalNAc. *Cell Host Microbe* 2016; 20: 215-25.
25. Hamada T, Zhang X, Mima K, *et al.* *Fusobacterium nucleatum* in colorectal cancer relates to immune response differentially by tumor microsatellite instability status. *Cancer Immunol Res* 2018; 6: 1327-36.
26. Pagès F, Mlecnik B, Marliot F, *et al.* International validation of the consensus Immunoscore for the classification of colon cancer: a prognostic and accuracy study. *Lancet* 2018; 391: 2128-39.
27. Lee DW, Han SW, Kang JK, *et al.* Association between *Fusobacterium nucleatum*, pathway mutation, and patient prognosis in colorectal cancer. *Ann Surg Oncol* 2018; 25: 3389-95.
28. Kim JH, Kang GH. Molecular and prognostic heterogeneity of microsatellite-unstable colorectal cancer. *World J Gastroenterol* 2014; 20: 4230-43.
29. Shang FM, Liu HL. *Fusobacterium nucleatum* and colorectal cancer: a review. *World J Gastrointest Oncol* 2018; 10: 71-81.

Quilty Lesions in the Endomyocardial Biopsies after Heart Transplantation

Haeyon Cho¹ · Jin-Oh Choi²
Eun-Seok Jeon² · Jung-Sun Kim^{1,3}

¹Department of Pathology and Translational Genomics, ²Division of Cardiology, Department of Medicine, Samsung Medical Center, Sungkyunkwan University School of Medicine, Seoul; ³Department of Health Sciences and Technology, Sungkyunkwan University, SAHST, Seoul, Korea

Received: September 3, 2018
Revised: November 28, 2018
Accepted: November 30, 2018

Corresponding Author

Jung-Sun Kim, MD, PhD
Department of Pathology and Translational Genomics, Samsung Medical Center, Sungkyunkwan University School of Medicine, 81 Irwon-ro, Gangnam-gu, Seoul 06351, Korea
Tel: +82-2-3410-2767
Fax: +82-2-3410-0025
E-mail: jsunkim@skku.edu

Background: The aim of this study was to investigate the clinical significance of Quilty lesions in endomyocardial biopsies (EMBs) of cardiac transplantation patients. **Methods:** A total of 1190 EMBs from 117 cardiac transplantation patients were evaluated histologically for Quilty lesions, acute cellular rejection, and antibody-mediated rejection. Cardiac allograft vasculopathy was diagnosed by computed tomography coronary angiography. Clinical information, including the patients' survival was retrieved by a review of medical records. **Results:** Eighty-eight patients (75.2%) were diagnosed with Quilty lesions, which were significantly associated with acute cellular rejection, but not with acute cellular rejection $\geq 2R$ or antibody-mediated rejection. In patients diagnosed with both Quilty lesions and acute cellular rejection, the time-to-onset of Quilty lesions from transplantation was longer than that of acute cellular rejections. We found a significant association between Quilty lesions and cardiac allograft vasculopathy. No significant relationship was found between Quilty lesions and the patients' survival. **Conclusions:** Quilty lesion may be an indicator of previous acute cellular rejection rather than a predictor for future acute cellular rejection.

Key Words: Quilty lesion; Endocardial inflammatory infiltrates; Acute cellular rejection; Cardiac allograft vasculopathy; Heart transplantation

Cardiac transplantation is a final therapeutic option for patients with end-stage heart failure. Approximately 4,000 cardiac transplantations are performed per year worldwide and the survival rate is approximately 81% at 1 year and 69% at 5 years.¹ The use of endomyocardial biopsies (EMBs) to monitor cardiac allograft rejection contributes to the excellent survival rates of cardiac transplantations. The diagnosis and grading of acute rejection are important for guiding the clinical management of heart recipients.

Along with acute rejection, other histologic findings have been observed in EMBs. One of these findings is nodular endocardial inflammatory infiltrates, which was termed Quilty lesion after the first patient in whom it was observed.² Quilty lesions may mimic acute cellular rejection when they extend into the myocardium.^{3,4} Other than mimicking acute cellular rejection, the clinical implications of Quilty lesions are poorly understood and controversial.

The aim of this study was to investigate the clinical signifi-

cance of Quilty lesions in cardiac transplant patients using a series of EMBs performed in a single institute. We analyzed the association of Quilty lesions with acute cellular rejection, antibody-mediated rejection, cardiac allograft vasculopathy, and patient survival and graft loss.

MATERIALS AND METHODS

Case selection

This retrospective study protocol was approved with exemption of informed consents from patients by the Institutional Review Board of Samsung Medical Center, Seoul, Korea (IRB No. 2018-08-149). One hundred and fifty-six patients underwent cardiac transplantation between January 2007 and December 2015 at Samsung Medical Center. Patients were included in the study group when all of their hematoxylin and eosin (H&E)-stained EMB slides were available. Patients who survived for less than 30 days, had fewer than three EMBs, or had heart failure

associated with cardiac malignancy were excluded. As such, 117 patients were included in this retrospective study. All patients received immunosuppression therapy with basiliximab, prednisolone, tacrolimus, cyclosporine A, and/or mycophenolate after cardiac transplantation. Patients with acute cellular rejection of grade 2R or greater according to the 2005 grading system of the International Society for Heart and Lung Transplantation (ISHLT) (grade 3 or greater according to the 1990 grading system of the ISHLT) were treated with steroid pulse therapy.

Endomyocardial biopsies

As a surveillance biopsy protocol, EMBs were obtained at 2, 4, 8, 12, 18, 24, 36, and 48 weeks following cardiac transplantation. Additional EMBs were obtained when acute rejection was clinically suspected. All H&E-stained EMB slides of the study patients were retrieved and evaluated histologically by a cardiovascular pathologist (J.-S.K.).

Diagnostic criteria of Quilty lesion, acute cellular rejection, antibody-mediated rejection, and coronary allograft vasculopathy

Quilty lesions are defined by dense endocardial inflammatory

infiltrates. Patients with at least one EMB with Quilty lesions are classified as Quilty positive, while patients who had never had Quilty lesions in the series of EMBs are classified as Quilty negative. Quilty lesions are subclassified as Quilty A when they are confined to the endocardium and Quilty B when they extend into the myocardium. Quilty-positive patients are further subdivided into Quilty B positive when they have at least one Quilty B lesion and Quilty A positive when they have never shown Quilty B lesions.

The diagnosis and histologic grading of acute cellular rejection were performed using the 2005 ISHLT criteria (Table 1, Fig. 1).⁵ Antibody-mediated rejection was defined by intravascular

Table 1. 2005 Grading system of the ISHLT for acute cellular rejection

Grade	Definition
Grade 0R ^a	No rejection
Grade 1R ^a	Interstitial and/or perivascular infiltrate with up to 1 focus of myocyte damage
Grade 2R ^a	Two or more foci of infiltrate with associated myocyte damage
Grade 3R ^a	Diffuse infiltrate with multifocal myocyte damage ± edema, ± hemorrhage ± vasculitis

ISHLT, International Society for Heart and Lung Transplantation. ^a“R” denotes revised grade to avoid confusion with 1990 scheme.

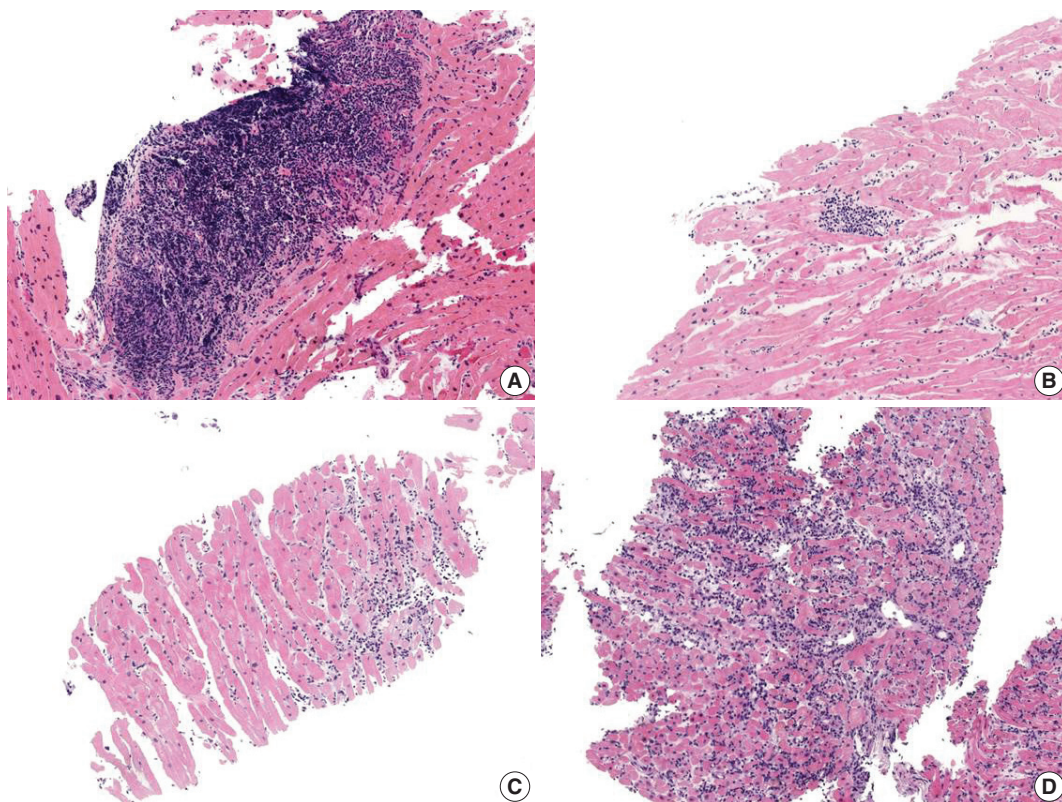


Fig. 1. Quilty lesion and acute cellular rejection. (A) Quilty lesion. (B) Grade 1R. (C) Grade 2R. (D) Grade 3R.



Fig. 2. Antibody-mediated rejection. (A) Swollen endothelial cells and intravascular mononuclear cells. (B) Multifocal C4d staining in capillary endothelial cells. (C) CD 68 staining in intravascular macrophages (arrow).

macrophages and endothelial cell damage, confirmed by immunostaining against C4d (1:50, polyclonal, Cell Marque, Rocklin, CA, USA) and CD68 (1:1,000, clone KP1, Dako, Glostrup, Denmark) (Fig. 2).

The coronary arteries of transplantation patients were evaluated using coronary angiography at 4 weeks from transplantation and with computed tomography coronary angiography annually following transplantation. Any stenosis of the coronary artery of >30% was considered cardiac allograft vasculopathy. Stenosis of coronary artery that required either intervention or retransplantation was considered significantly severe cardiac allograft vasculopathy.

Statistics

The IBM SPSS Statistics software package (ver. 24.0, IBM Corp., Armonk, NY, USA) was used for all statistical analyses, and a p-value of <.05 was considered statistically significant. The associations between Quilty lesions and acute cellular rejection or cardiac allograft vasculopathy were evaluated with chi-square test or Fisher exact test.

For patients with both Quilty lesions and acute cellular rejection, the time-to-onset from transplantation to Quilty lesions and acute cellular rejection was calculated by subtracting the date of transplantation from the date when Quilty lesions or acute cellular rejection were diagnosed for the first time, respectively. A paired T-test was used for comparison. The association between Quilty lesions and transplantation failure was evaluated using Kaplan-Meier estimation and assessed using the log-rank test. The clinical variables including the presence of Quilty lesion were evaluated by univariate and multivariate analyses of disease-free survival with Cox proportional hazards model. The composite end-points were graft loss and mortality of any causes.

Table 2. Summary of clinical characteristics of the study patients

Characteristic	Total (n=117)	Quilty-positive (n=88)	Quilty-negative (n=29)
Age at heart transplantation (yr)	46.6	46.2	47.8
Sex			
Male	73 (62.4)	54 (61.4)	19 (65.5)
Female	44 (37.6)	34 (38.6)	10 (34.5)
Cause of heart failure			
DCMP	86 (73.5)	65 (73.9)	21 (72.4)
Ischemic heart disease	16 (13.7)	13 (14.8)	3 (10.3)
HCMP	7 (6.0)	6 (6.8)	1 (3.4)
Others	8 (6.8)	4 (4.5)	4 (13.8)
No. of EMBs	10.2	10.4	9.5
Follow-up period (mo)	55.7	55.7	55.4

Values are presented as mean or number (%).

DCMP, dilated cardiomyopathy; HCMP, Hypertrophic cardiomyopathy; EMB, endomyocardial biopsy.

RESULTS

Transplant recipients

The study population consisted of 73 (62.4%) males and 44 (37.6%) females. The mean age at cardiac transplantation was 46 ± 16 years. The most common cause of heart failure was dilated cardiomyopathy (73.5%), followed by ischemic heart disease (13.7%), and hypertrophic cardiomyopathy (5.8%). The mean follow-up period for all patients was 58 months. A total of 1190 EMBs were collected from 117 patients, and the average number of EMBs per patient was 10.2 ± 0.2 (Table 2).

Quilty lesions in EMBs

Quilty lesions were found in 88 (75.2%) patients, and the average number of the EMBs with Quilty lesions in these patients was 2.8 ± 0.2 . The number of EMBs with Quilty lesions for each biopsy order was shown in Fig. 3. The number of EMBs with Quilty lesions had a tendency to increase as the biopsy order increases. There were no significant differences in the age ($46.2 \pm$

16.6 years vs 47.8 ± 14.3 years) or sex (53 males/35 females vs 17 males/12 females) between Quilty-positive and Quilty-negative patients (Table 2).

Quilty A–positive patients and Quilty B–positive patients showed no significant differences in clinical outcomes, which concur with the previous report (Supplemental Table S1).² As such, we decided not to subdivide Quilty-positive patients for further analyses.

Quilty lesions and acute cellular rejection

Of the 117 patients, 103 (88.0%) were diagnosed with acute cellular rejection in at least one of the series of EMBs and among them, 28 (23.9%) patients were diagnosed with acute cellular rejection of ISHLT grade 2R or higher. In the series of EMBs, Quilty-positive patients were more likely to be diagnosed with acute cellular rejections than Quilty-negative patients, and the difference was significant ($p = .006$). However, there was no significant association between Quilty lesions and acute cellular rejection of ISHLT grade 2R or higher ($p = .697$) (Table 3).

When comparing the time-to-onset of Quilty lesions and acute cellular rejection during the post-transplantation follow-up period, the time-to-onset of Quilty lesions was significantly longer than that of acute cellular rejection (179.2 days vs 65.5 days, $p < .001$) (Fig. 4).

Quilty lesions and antibody-mediated rejection

Of the 117 patients, 15 (12.8%) showed at least one episode of antibody-mediated rejection in the series of EMBs. Among the 15 patients with antibody-mediated rejection, 11 were Quilty positive while four were Quilty negative. There was no statistically significant association between Quilty lesions and antibody-

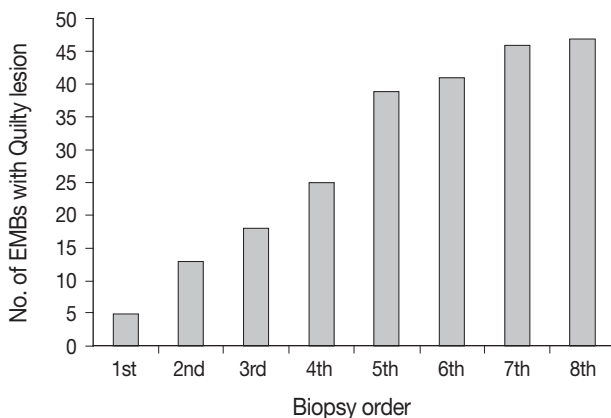


Fig. 3. Then number of Quilty-positive endomyocardial biopsies (EMBs) for each biopsy order. The number of Quilty-positive EMBs increases as biopsy order increases.

mediated rejection (Table 3).

Quilty lesions and cardiac allograft vasculopathy

Of the 117 patients, 43 (36.8%) developed cardiac allograft vasculopathy detected by coronary angiography, from as early as 4 weeks to 71 months after transplantation. Among them, 13 patients showed significantly severe cardiac allograft vasculopathy that required treatment: seven underwent percutaneous coronary intervention (PCI) or balloon dilatation, five suffered graft loss and underwent retransplantation, and one underwent retransplantation after PCI. There was a significant correlation between the presence of Quilty lesions and cardiac allograft vasculopathy ($p = .012$) (Table 3). In addition, a significant correlation was

Table 3. Clinical outcomes in Quilty-positive and Quilty-negative patients

Clinical outcome	Quilty-positive (n=88)	Quilty-negative (n=29)	p-value
Acute cellular rejection			
Any ACR	82 (93.2)	21 (72.4)	.006*
ACR \geq 2R	23 (26.1)	5 (17.2)	.697
Antibody mediated rejection	11 (12.5)	4 (13.8)	>.990
Cardiac allograft vasculopathy			
Any CAV	38 (43.2)	5 (17.2)	.012*
Significant CAV	13 (14.8)	0	.036*

Values are presented as number (%).
 ACR, acute cellular rejection; CAV, cardiac allograft vasculopathy.
 *Statistically significant ($p < .05$).

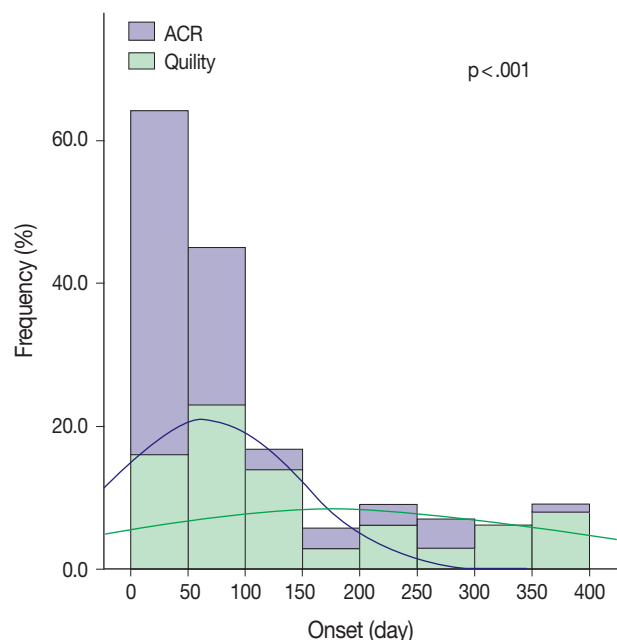


Fig. 4. Time-to-onset from cardiac transplantation to acute cellular rejection (ACR) and Quilty lesions. The time-to-onset of Quilty lesion is significantly longer than that of acute cellular rejection.

found between the presence of Quilty lesions and significantly severe cardiac allograft vasculopathy requiring either intervention or retransplantation ($p = .036$) (Table 3).

Quilty lesions and transplantation failure

A Kaplan–Meier analysis was performed for all-cause transplant failure (mortality and graft loss) according to the presence of Quilty lesions (Fig. 5). Median disease-free survival time was 109.5 months for Quilty-positive patients and 96.4 months for Quilty-negative patients, but this difference was not significant ($p = .990$). No significant difference in survival was observed

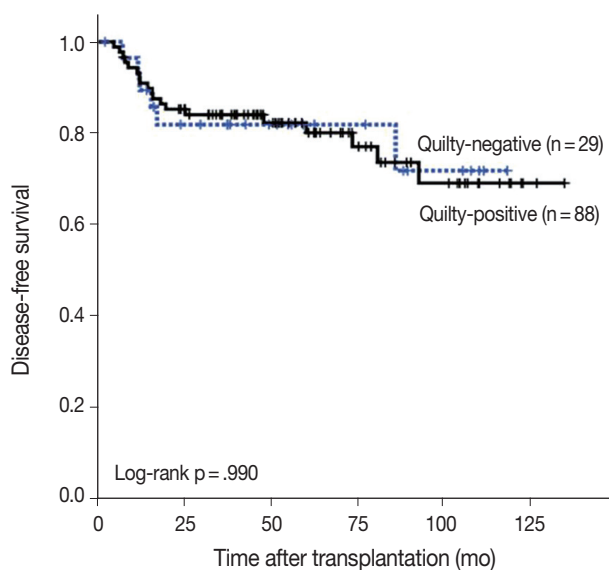


Fig. 5. Kaplan-Meier analysis for disease-free survival (death, graft loss) in Quilty-positive and Quilty-negative patients. The difference in survival between Quilty-positive and Quilty-negative is not significant.

between Quilty-positive and Quilty-negative groups in multivariate Cox regression analysis, either. The presence of antibody mediated rejection was the only independent factor of disease-free survival in multivariate Cox regression analysis (Table 4).

DISCUSSION

Quilty lesions in EMBs appear as focal flat to nodular, densely cellular endocardial infiltrates composed mainly of lymphocytes with histiocytes, dendritic cells and occasional plasma cells with a high proportion of T lymphocytes.^{3,6,7} Some Quilty lesions appear as extensive inflammatory infiltrates with an extension to the myocardium, and often misinterpreted as high grade acute cellular rejections. Quilty lesions have been reported to occur in 10% to 20% of EMBs and 58% to 74% of cardiac transplantation patients.^{8,9} Although Quilty lesions are frequently reported in EMBs and many studies have been conducted on Quilty lesions, the relationship between Quilty lesions and clinical outcomes remains unclear.

Quilty lesions have been reported to be associated with acute cellular rejection and are claimed to signal acute cellular rejection episodes in future EMBs,⁸⁻¹² while other studies have suggested that there is no significant association between Quilty lesions and acute cellular rejection.^{2,6,13} In our study, patients with Quilty lesions showed a significantly higher incidence of acute cellular rejection, which agrees with some of previous studies,⁸⁻¹² but no significant association with grade 2R or higher acute cellular rejection, which required additional treatment. When we evaluated time-to-onset from transplantation to EMBs with Quilty lesions and acute cellular rejection, we found that Quilty lesions

Table 4. Cox regression analysis for disease-free survival

	Univariate analysis			Multivariate analysis		
	HR	95% CI	p-value	HR	95% CI	p-value
Quilty lesion	1.006	0.401–2.521	.990	-	-	-
Antibody mediated rejection	5.048	2.222–11.470	<.001*	4.185	1.510–11.598	.006*
Any ACR	3.136	0.424–23.187	.263	-	-	-
ACR \geq 2R	2.424	1.081–4.437	.032*	-	-	-
Any CAV	0.550	0.229–1.323	.550	-	-	-
Significant CAV	2.564	1.057–6.220	.037*	-	-	-
Age at transplantation	0.973	0.951–0.995	.019	-	-	-
History of dialysis	1.527	0.570–4.085	.400	-	-	-
History of DM	1.862	0.737–4.709	.189	-	-	-
VAD at time of transplantation	2.359	1.069–5.206	.034*	-	-	-
Ventilator at time of transplantation	5.609	2.470–12.736	<.001*	-	-	-
PRA >20%	2.500	1.139–5.486	.022*	-	-	-

HR, hazard ratio; CI, confidence interval; ACR, acute cellular rejection; CAV, cardiac allograft vasculopathy; DM, diabetes mellitus; VAD, ventricular assist device; PRA, panel reactive antibody.

*Statistically significant ($p < .05$).

had a significantly longer time-to-onset than acute cellular rejection. This may suggest that Quilty lesion is an indicator of previous acute cellular rejection rather than a predictor of future acute cellular rejections.

We observed a significant correlation between Quilty lesions and cardiac allograft vasculopathy in the graft. Cardiac allograft vasculopathy is a long-term complication after heart transplantation to cause myocardial ischemic injury and graft loss. Histologically, cardiac allograft vasculopathy appears as concentric intimal hyperplasia of the coronary arteries and diffusely involves the coronary arteries, from epicardial arteries to small intramyocardial branches but the native vessels of recipients are spared.¹⁴ The pathogenesis of cardiac allograft vasculopathy is not fully understood. However, the sparing of native vessels suggests an immune mechanism targeting the allograft.¹⁵ Hiemann *et al.*¹⁶ suggested that Quilty lesions might be associated with endothelial disease, which could lead to graft failure. Yamani *et al.*¹⁷ observed the expression of the vitronectin receptor ($\alpha v\beta 3$) in Quilty lesions and suggested that the vitronectin receptor may be the link between Quilty lesions and transplant vasculopathy, since vitronectin receptor involves endothelial cell migration and vascular smooth muscle cell proliferation induced by growth factors and cytokines. Our result on the association between Quilty lesions and cardiac allograft vasculopathy in the graft was supported by the studies of Hiemann *et al.*¹⁶ and Yamani *et al.*¹⁷

Szymanska *et al.*¹⁸ reported a significantly higher incidence of Quilty lesions in the EMBs of patients with C4d capillary depositions (antibody-mediated rejection). Cano *et al.*¹⁹ reported a significant association between Quilty lesions and endocardial C4d deposition in patients without evidence of rejection and suggested association between Quilty lesions and complement activation. We observed no significant association between Quilty lesions and antibody-mediated rejection, in contrast with the previous study by Szymanska *et al.*¹⁸ This result might be related to the smaller population in our study and the difference in the prevalence of antibody-mediated rejection: the prevalence of antibody-mediated rejection in our study (16/117, 13.7%) was higher than that in the Szymanska's study (16/212, 7.5%). Further validation in larger groups is desired since there are few reports on the relationship between Quilty lesions and antibody-mediated rejection.

The major causes of mortality after cardiac transplantation are early graft failure, allograft rejection, and infection in the first 3 years following transplantation and cardiac allograft vasculopathy, malignancy, and renal failure after 5 years from transplantation.¹ A long list of risk factors such as increasing donor and recipient

age, long cold ischemic time, congenital heart disease, history of dialysis and transfusions, prior transplantation are reported to be significantly associated with cardiac transplantation patient survival.¹ Quilty lesions have been reported to be associated with poor survival rates,^{16,20} while other studies have reported that Quilty lesions were associated with improved survival¹⁰ or had no significant association with survival.² In our study, there was no significant difference in the median survival time between Quilty-positive patients and Quilty-negative patients, in spite of the association of Quilty lesions with cardiac allograft vasculopathy and acute cellular rejection. It also supports that Quilty lesion is an indicator of previous acute cellular rejection rather than a meaningful risk factor for patients' survival.

There are some limitations of our study. (1) The total number of the patients was relatively small and their follow-up was rather short. (2) Evaluation of acute cellular rejection and Quilty lesions was based on the biopsy specimen instead of the whole heart. We evaluated at least three fragments of tissue for each EMB, but there is still the possibility of false negativity for the lesions. (3) The frequency of acute cellular rejection was rather high (88%). However, that of acute cellular rejection $\geq 2R$ was 24%, which was comparable to that 28% of recipients experienced at least 1 episode of treated acute rejection during follow-up between 2004 and June 2016, according to 2017 ISHLT reports.²¹

Our study is the first to describe the significance of Quilty lesions among cardiac transplantation patients in Korea. Our results suggest that Quilty lesion is in fact an indicator of previous acute cellular rejection and has a correlation with cardiac allograft vasculopathy. Further studies employing longer follow-up periods and/or more data from multiple centers are required, and additional studies on pathogenesis would be helpful to understand the biological significance of Quilty lesions.

ORCID

Haeyon Cho: <https://orcid.org/0000-0001-9782-7562>
 Jin-Oh Choi: <https://orcid.org/0000-0002-2441-2267>
 Eun-Seok Jeon: <https://orcid.org/0000-0002-9946-5611>
 Jung-Sun Kim: <https://orcid.org/0000-0002-7221-2737>

Electronic Supplementary Material

Supplementary materials are available at Journal of Pathology and Translational Medicine (<http://jpatholm.org>).

Conflicts of Interest

The authors declare that they have no potential conflicts of interest.

REFERENCES

- Lund LH, Edwards LB, Kucheryavaya AY, *et al.* The Registry of the International Society for Heart and Lung Transplantation: Thirtieth official adult heart transplant report 2013: focus theme: age. *J Heart Lung Transplant* 2013; 32: 951-64.
- Joshi A, Masek MA, Brown BW Jr, Weiss LM, Billingham ME. "Quilty" revisited: a 10-year perspective. *Hum Pathol* 1995; 26: 547-57.
- Marboe CC, Billingham M, Eisen H, *et al.* Nodular endocardial infiltrates (Quilty lesions) cause significant variability in diagnosis of ISHLT Grade 2 and 3A rejection in cardiac allograft recipients. *J Heart Lung Transplant* 2005; 24(7 Suppl): S219-26.
- Mozaffari K, Bakhshandeh H, Amin A, *et al.* Diagnostic pitfalls and challenges in interpretation of heart transplantation rejection in endomyocardial biopsies with focus on our experience. *Res Cardiovasc Med* 2014; 3: e13986.
- Stewart S, Winters GL, Fishbein MC, *et al.* Revision of the 1990 working formulation for the standardization of nomenclature in the diagnosis of heart rejection. *J Heart Lung Transplant* 2005; 24: 1710-20.
- Kottke-Marchant K, Ratliff NB. Endomyocardial lymphocytic infiltrates in cardiac transplant recipients: incidence and characterization. *Arch Pathol Lab Med* 1989; 113: 690-8.
- Radio SJ, McManus BM, Winters GL, *et al.* Preferential endocardial residence of B-cells in the "Quilty effect" of human heart allografts: immunohistochemical distinction from rejection. *Mod Pathol* 1991; 4: 654-60.
- Chu KE, Ho EK, de la Torre L, Vasilescu ER, Marboe CC. The relationship of nodular endocardial infiltrates (Quilty lesions) to survival, patient age, anti-HLA antibodies, and coronary artery disease following heart transplantation. *Cardiovasc Pathol* 2005; 14: 219-24.
- Costanzo-Nordin MR, Winters GL, Fisher SG, *et al.* Endocardial infiltrates in the transplanted heart: clinical significance emerging from the analysis of 5026 endomyocardial biopsy specimens. *J Heart Lung Transplant* 1993; 12: 741-7.
- Pardo-Mindan FJ, Lozano MD. "Quilty effect" in heart transplantation: is it related to acute rejection? *J Heart Lung Transplant* 1991; 10: 937-41.
- Smith RN, Chang Y, Houser S, Dec GW, Grazette L. Higher frequency of high-grade rejections in cardiac allograft patients after Quilty B lesions or grade 2/4 rejections. *Transplantation* 2002; 73: 1928-32.
- Zakliczynski M, Nozynski J, Konecka-Mrowka D, *et al.* Quilty effect correlates with biopsy-proven acute cellular rejection but does not predict transplanted heart coronary artery vasculopathy. *J Heart Lung Transplant* 2009; 28: 255-9.
- Suit PF, Kottke-Marchant K, Ratliff NB, Pippenger CE, Easley K. Comparison of whole-blood cyclosporine levels and the frequency of endomyocardial lymphocytic infiltrates (the Quilty lesion) in cardiac transplantation. *Transplantation* 1989; 48: 618-21.
- Colvin-Adams M, Agnihotri A. Cardiac allograft vasculopathy: current knowledge and future direction. *Clin Transplant* 2011; 25: 175-84.
- Hosenpud JD, Shipley GD, Wagner CR. Cardiac allograft vasculopathy: current concepts, recent developments, and future directions. *J Heart Lung Transplant* 1992; 11(1 Pt 1): 9-23.
- Hiemann NE, Knosalla C, Wellnhofer E, Lehmkuhl HB, Hetzer R, Meyer R. Quilty indicates increased risk for microvasculopathy and poor survival after heart transplantation. *J Heart Lung Transplant* 2008; 27: 289-96.
- Yamani MH, Ratliff NB, Starling RC, *et al.* Quilty lesions are associated with increased expression of vitronectin receptor (alpha5beta1) and subsequent development of coronary vasculopathy. *J Heart Lung Transplant* 2003; 22: 687-90.
- Szymanska S, Grajkowska W, Sobieszczanska-Malek M, Zielinski T, Pyzlak M, Pronicki M. Prevalence of the Quilty effect in endomyocardial biopsy of patients after heart transplantation: from cellular rejection to antibody-mediated rejection? *Pol J Pathol* 2016; 67: 216-20.
- Cano LC, Arteta AA, Fernández R, *et al.* Quilty effect areas are frequently associated with endocardial C4d deposition. *J Heart Lung Transplant* 2008; 27: 775-9.
- Hiemann NE, Knosalla C, Wellnhofer E, Lehmkuhl HB, Hetzer R, Meyer R. Quilty in biopsy is associated with poor prognosis after heart transplantation. *Transpl Immunol* 2008; 19: 209-14.
- Chambers DC, Yusem RD, Cherikh WS, *et al.* The Registry of the International Society for Heart and Lung Transplantation: Thirty-fourth Adult Lung And Heart-Lung Transplantation Report-2017; focus theme: allograft ischemic time. *J Heart Lung Transplant* 2017; 36: 1047-59.

Primary Peripheral Gamma Delta T-Cell Lymphoma of the Central Nervous System: Report of a Case Involving the Intramedullary Spinal Cord and Presenting with Myelopathy

Jeemin Yim · Seung Geun Song
Sehui Kim · Jae Won Choi¹
Kyu-Chong Lee² · Jeong Mo Bae
Yoon Kyung Jeon

Departments of Pathology and ¹Radiology, Seoul National University Hospital, Seoul; ²Department of Radiology, Korea University Guro Hospital, Seoul, Korea

Received: July 23, 2018
Revised: August 20, 2018
Accepted: August 21, 2018

Corresponding Author

Yoon Kyung Jeon, MD, PhD
Department of Pathology, Seoul National University College of Medicine, 103 Daehak-ro, Jongno-gu, Seoul 03080, Korea
Tel: +82-2-740-8323
Fax: +82-2-743-5530
E-mail: ykjeon@snu.ac.kr

Primary central nervous system lymphoma of T-cell origin (T-PCNSL) is rare, and its clinicopathological features remain unclear. Peripheral T-cell lymphoma of $\gamma\delta$ T-cell origin is an aggressive lymphoma mainly involving extranodal sites. Here, we report a case of $\gamma\delta$ T-PCNSL involving the intramedullary spinal cord and presenting with paraplegia. A 75-year-old Korean woman visited the hospital complaining of back pain and lower extremity weakness. Magnetic resonance imaging revealed multifocal enhancing intramedullary nodular lesions in the thoracic and lumbar spinal cord. An enhancing nodular lesion was observed in the periventricular white matter of the lateral ventricle in the brain. There were no other abnormalities in systemic organs or skin. Laminectomy and tumor removal were performed. The tumor consisted of monomorphic, medium-to-large atypical lymphocytes with pale-to-eosinophilic cytoplasm. Immunohistochemically, the tumor cells were CD3(+), TCR β F1(-), TCR γ (+), CD30(-), CD4(-), CD8(-), CD56(+), TIA1(+), granzyme B(+), and CD103(+). Epstein-Barr virus *in situ* was negative. This case represents a unique T-PCNSL of $\gamma\delta$ T-cell origin involving the spinal cord.

Key Words: Primary central nervous system lymphoma; Primary intramedullary spinal cord lymphoma; Peripheral T-cell lymphoma; $\gamma\delta$ T-cell lymphoma

Primary central nervous system lymphoma (PCNSL) is defined as a lymphoma arising in the brain, spinal cord, leptomeninges, or eye with no evidence of systemic disease.¹ PCNSL accounts for 6% of all primary brain tumors and 4%–5% of extranodal lymphomas.¹ Although diffuse large B-cell lymphoma (DLBCL) accounts for the majority (more than 90%) of PCNSL, those of T- or B-cell origin other than DLBCL have been reported in immunocompetent and immunocompromised hosts.²⁻⁵ The incidence of PCNSL of T-cell origin (T-PCNSL) has been variably reported as 2%–4% (Western countries) to 7%–9% (East-Asian) of PCNSL.^{2,3} Intramedullary spinal tumor accounts for 5%–10% of spinal tumors, and most of them are glial tumors.⁶ Primary intramedullary spinal cord lymphoma (PISCL) comprises about 1% of all central nervous system (CNS) lymphoma.⁶⁻⁸ A recent Western population-based study on PISCL demonstrated that only 1.4% of PISCL was of T-cell origin.⁸ Peripheral T-cell lymphoma (PTCL) of $\gamma\delta$ T-cell origin is a rare aggressive lymphoma

that mainly involves extranodal sites including spleen, liver, skin, and intestine.⁹ Here, we report a primary CNS PTCL of $\gamma\delta$ T-cell origin presenting with myelopathy from intramedullary spinal cord involvement.

CASE REPORT

A 75-year-old Korean woman presented with back pain and lower extremity weakness for 3.5 months. Lower extremity weakness causing difficulty in ambulation was temporarily relieved after steroid therapy. She had underlying hypertension, hyperlipidemia, and type 2 diabetes and had no history of immunodeficiency. Spine magnetic resonance imaging (MRI) revealed multiple enhancing intramedullary nodular lesions in the spinal cord at T9/10, T11, and L5 levels (Fig. 1A). Brain MRI revealed a small enhancing nodular lesion in the periventricular white matter of the left lateral ventricle (Fig. 1C–E). Clinicoradiological

diagnoses included tumorous conditions such as lymphoma, glioma, and metastasis or nontumorous myelitis. Spinal and brain lesions had increased in size on MRI taken 1.5 months after initial presentation (Fig. 1B, F–J). Multiple newly developed enhancing nodules were observed in the lateral subependymal lining, left frontal lobe, and right temporal lobe (Fig. 1K). Positron emission tomography scan showed mild hypermetabolism in spinal cord lesions. No other abnormal findings were identified in the systemic organs and skin. The patient underwent T11 laminectomy and tumor removal. Microscopic examination of tumor revealed diffuse infiltration of monotonous, medium-to-large atypical lymphocytes with round nuclei, condensed chromatin, pale-to-eosinophilic cytoplasm, and small inconspicuous nucleoli (Fig. 2). Vasculature with high endothelial cells was noted throughout the tumor, and perivascular infiltration of tumor cells was occasionally observed along with diffuse infiltration of tumor cells in glial tissue (Fig. 2). Immunohistochemically, the atypical cells were CD3(+), CD20(–), TCR β F1(–),

TCR γ (+), CD30(–), CD4(–), CD8(–), CD10(–), BCL6(–), MUM1(–), CD56(+), TIA-1(+), granzyme B(focal +), and CD103(+). The Ki-67 index was about 80%, and Epstein-Barr virus *in situ* hybridization showed no positive cells. T-cell monoclonality was detected by *TCRG* gene rearrangement study using IdentiClone *TCRG* Gene Clonality Assay (Invivoscribe Technologies Inc., San Diego, CA, USA) (Fig. 3I). This case represents a unique PCNSL of $\gamma\delta$ T-cell origin involving the spinal cord that presented with paraplegia.

The Institutional Review Board (IRB) of Seoul National University Hospital (SNUH) approved this study (No. H-1807-070-958) and waived the need for informed consent from patients.

DISCUSSION

The detailed pathological features of T-PCNSL remain unclear. In the largest series of T-PCNSL ($n = 45$) published 2005 by Shenkier *et al.*,² tumor cells were “small or small-to-medium

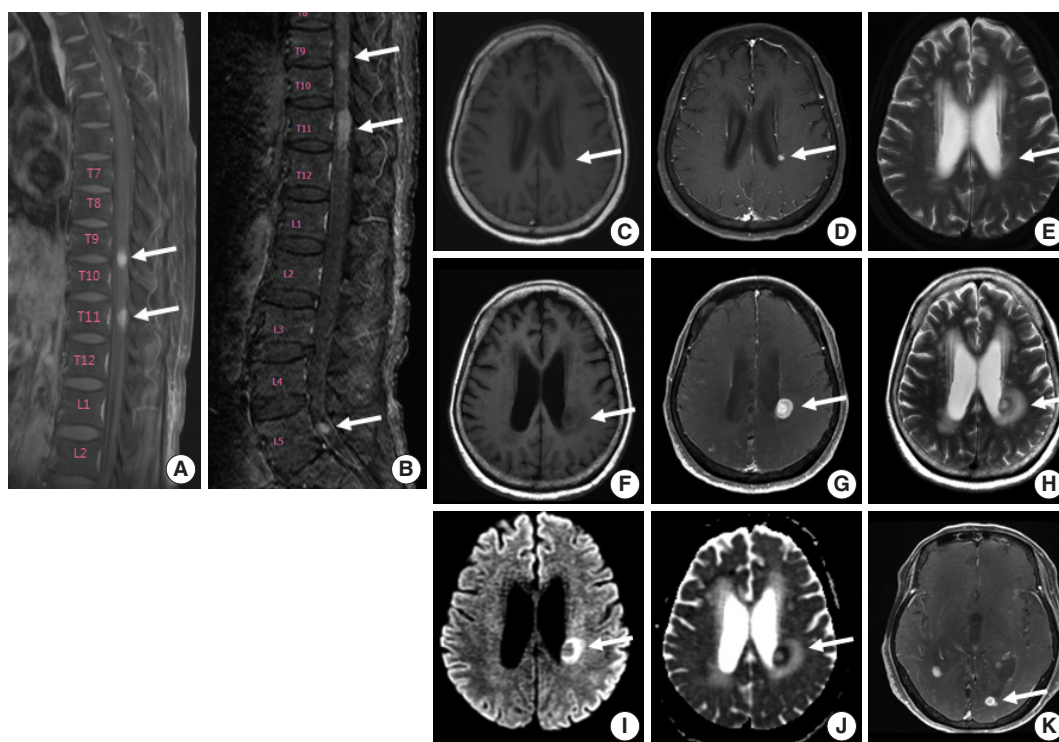


Fig. 1. Spine and brain magnetic resonance imaging (MRI) features at presentation (A, C–E) and 6 weeks later (B, F–K). (A) Spine MRI sagittal view revealed enhancing intramedullary nodular lesions at T9/10 and T11 levels (arrows). (B) Six weeks later, enhancing intramedullary nodular lesions (arrows) at T7/8, T9/10, and T11 levels were enlarged, and an enhancing nodule appeared at L5 level with leptomeningeal enhancement. (C–E) A nodular lesion (arrows) was observed in the periventricular white matter of the left lateral ventricle, which showed enhancement in T1 enhanced image (D) compared to T1 weighted image (C) and heterogeneous high signal intensity in T2 weighted images (E). (F–H) After 6 weeks, the lesion (arrows) increased in size with surrounding edema in T1 weighted (F), T1 enhanced (G), and T2 weighted images (H). (I, J) Diffusion weighted images revealed diffusion restriction within the tumor with high signal intensity (arrow) (I) and corresponding low signal intensity (arrow) on the apparent diffusion coefficient map (J). (K) There were also multiple newly developed enhancing nodules in the lateral subependymal lining, left frontal lobe, and right temporal lobe (arrow).

sized” in 12 cases and “pleomorphic or medium-to-large” in 13 cases. Of the nine Korean patients with T-PCNSL reported by Lim *et al.*,³ seven were diagnosed with PTCL, while two were diagnosed with T-lineage lymphoma with no further specification.

Menon *et al.*'s series⁴ (n = 18) of T-PCNSL comprised 15 cases of PTCL not otherwise specified (NOS) with small (n = 2), small-medium (n = 6), medium (n = 3), and medium-large or large (n = 4) tumor cells; one case was anaplastic lymphoma kinase (ALK)

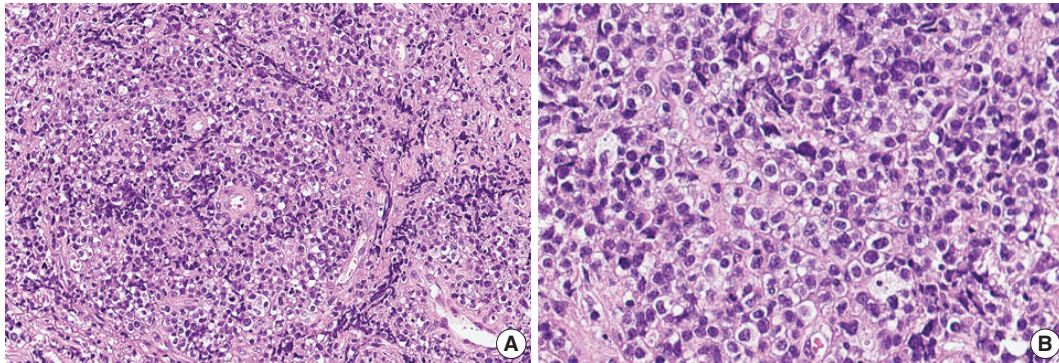


Fig. 2. Histologic features of $\gamma\delta$ T-cell lymphoma involving the spinal cord. (A) Monomorphic medium-to-large atypical lymphoid cells diffusely infiltrating the spinal cord parenchyma with occasional perivascular arrangement. (B) Atypical lymphoid cells showed clear to eosinophilic cytoplasm with distinct cell borders and hyperchromatic nuclei with small indistinct nucleoli.

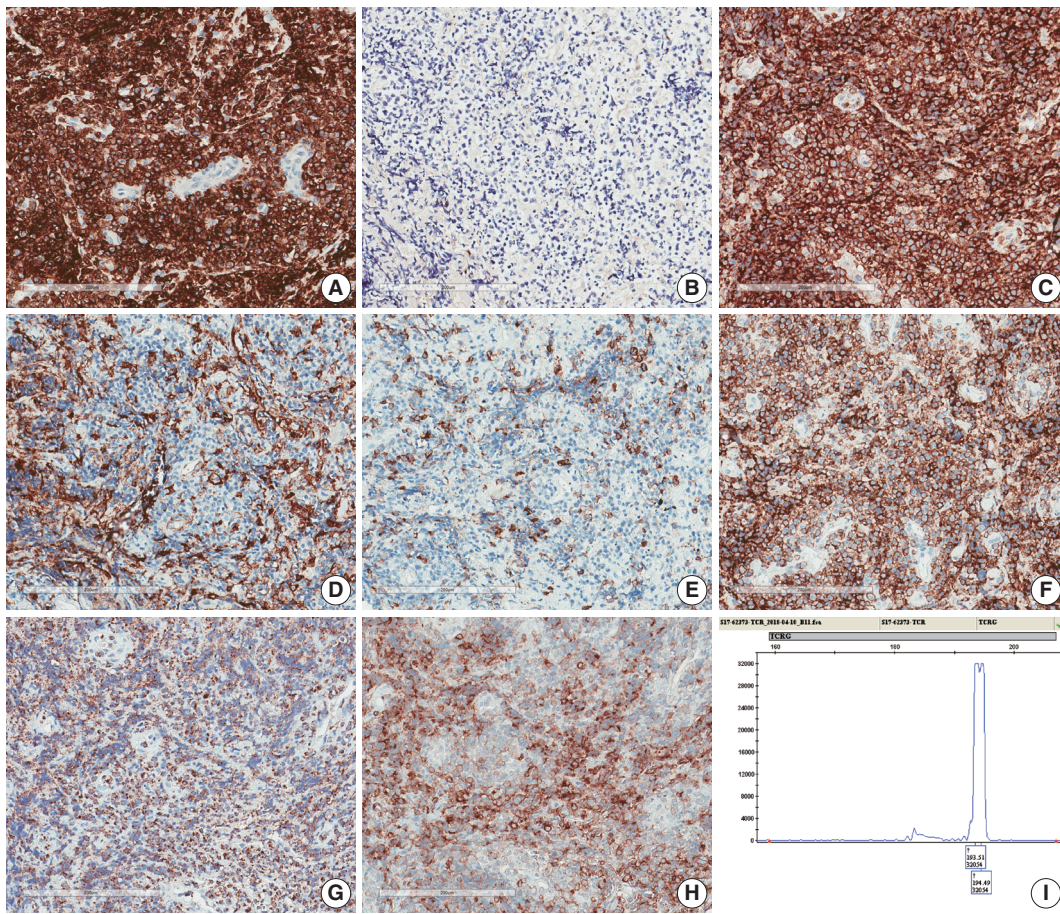


Fig. 3. Immunohistochemical and genetic features of $\gamma\delta$ T-cell lymphoma involving the spinal cord. Tumor cells were CD3(+) (A), TCR β 1(-) (B), TCR γ (+) (C), CD4(-) (D), CD8(-) (E), CD56(+) (F), TIA1(+) (G), and CD103(+) (H). (I) Monoclonal peak was observed in TCR γ gene rearrangement study.

(+) ALCL and two cases were ALK(-) ALCLs. Of note, two of the 15 PTCL NOS cases expressed TCR γ , suggestive of $\gamma\delta$ T-cell derivation. One of the patients with $\gamma\delta$ T-PCNSL was a 31-year-old male with bilateral temporal lobe involvement. The other was a 56-year-old female with a solitary frontal mass. The tumors of both patients were composed of small-medium cells with CD4(-)CD8(+) phenotype.⁴ Recently, Mooney *et al.*¹⁰ reported another case of $\gamma\delta$ T-PCNSL involving the cerebellum in a 26-year-old Korean female. To the best of our knowledge, our patient is the fourth case of $\gamma\delta$ T-PCNSL and the first case of $\gamma\delta$ T-PCNSL involving the spinal cord presenting with myelopathy.

The clinical features and outcomes of patients with T-PCNSL remain unclear. Based on previous reports, T-PCNSL predominantly involves older patients, but with a wide age range from 3 to 84 years, and the male to female ratio is 1.8:1. In prior reports, involvement of deep brain structures and presentation with multifocal lesions were observed in about 34% and 43% patients, respectively.²⁻⁴ The disease-specific survival of patients with T-PCNSL was 25 months (95% confidence interval, 11 to 38 months).² Although the prognosis of T-PCNSL is controversial, Shenkier *et al.*² and Lim *et al.*³ demonstrated that the clinical outcome of patients with T-PCNSL was comparable to that of patients with B-PCNSL, and performance status and high-dose methotrexate-based therapy were associated with patient prognosis. Of the four reported cases with $\gamma\delta$ T-PCNSL including our case, detailed treatment modality and outcome are available in only one patient.¹⁰ A 26-year-old female with cerebellar $\gamma\delta$ T-PCNSL underwent subtotal mass resection followed by high-dose methotrexate and cytarabine therapy, and she remained alive at 3 months.¹⁰ Although our patient was lost to follow-up after surgery, lesions involving the spinal cord and brain had rapidly progressed before surgery.

The current revised 2016 World Health Organization (WHO) classification recognizes three entities of $\gamma\delta$ T-cell lymphoma ($\gamma\delta$ TCL) including hepatosplenic $\gamma\delta$ TCL, primary cutaneous $\gamma\delta$ TCL, and monomorphic epitheliotropic intestinal TCL.¹ However, $\gamma\delta$ TCLs involving other extranodal sites were reported including the lung, orbit, and tongue.¹¹⁻¹³ Morphologic features of $\gamma\delta$ TCL cells vary, but these cells often share the following immunophenotype: CD2(+), CD3(+), CD4(-), CD5(-), CD7(+/-), CD8(-/+), CD56(+/-), TIA1(+), granzyme B(+/-), perforin(+/-), TCR β F1(-), and TCR γ (+).⁹ In general, $\gamma\delta$ TCL aggravates rapidly and responds poorly to standard chemotherapy.⁹ Recently, recurrent genetic alterations involving the JAK/STAT pathway and epigenetic pathway were demonstrated in $\gamma\delta$ TCLs.^{14,15} Thus, it is necessary to gather clinical data of $\gamma\delta$ TCLs and discover new

therapeutics.

In summary, we report a unique case of $\gamma\delta$ T-PCNSL involving the intramedullary spinal cord that presented with myelopathy. This case will intrigue and stimulate clinicians and pathologists to engage in the study of $\gamma\delta$ TCL and T-PCNSL to discover effective therapeutic strategies and new targets for therapy.

ORCID

Jeemin Yim: <https://orcid.org/0000-0002-8571-7486>

Seung Geun Song: <https://orcid.org/0000-0002-1605-2708>

Sehui Kim: <https://orcid.org/0000-0002-6640-3051>

Jae Won Choi: <https://orcid.org/0000-0002-5937-7238>

Kyu-Chong Lee: <https://orcid.org/0000-0002-4518-8567>

Jeong Mo Bae: <https://orcid.org/0000-0003-0462-3072>

Yoon Kyung Jeon: <https://orcid.org/0000-0001-8466-9681>

Conflicts of Interest

The authors declare that they have no potential conflicts of interest.

Acknowledgments

This work was supported by the Basic Science Research Program (grant No.: NRF-2016R1D1A1B01015964) through the National Research Foundation (NRF) funded by the Ministry of Education, Science, and Technology (MEST), Republic of Korea.

REFERENCES

1. Swerdlow SH, Campo E, Harris NL, *et al.* WHO classification of tumours of haematopoietic and lymphoid tissues. Revised 4th ed. Lyon: International Agency for Research on Cancer, 2017.
2. Shenkier TN, Blay JY, O'Neill BP, *et al.* Primary CNS lymphoma of T-cell origin: a descriptive analysis from the international primary CNS lymphoma collaborative group. *J Clin Oncol* 2005; 23: 2233-9.
3. Lim T, Kim SJ, Kim K, *et al.* Primary CNS lymphoma other than DLBCL: a descriptive analysis of clinical features and treatment outcomes. *Ann Hematol* 2011; 90: 1391-8.
4. Menon MP, Nicolae A, Meeker H, *et al.* Primary CNS T-cell Lymphomas: a clinical, morphologic, immunophenotypic, and molecular analysis. *Am J Surg Pathol* 2015; 39: 1719-29.
5. Nael A, Walavalkar V, Wu W, *et al.* CD4-positive T-cell primary central nervous system lymphoma in an HIV positive patient. *Am J Clin Pathol* 2016; 145: 258-65.
6. Guzzetta M, Drexler S, Buonocore B, Donovan V. Primary CNS T-cell lymphoma of the spinal cord: case report and literature review.

- Lab Med 2015; 46: 159-63.
7. Flanagan EP, O'Neill BP, Porter AB, Lanzino G, Haberman TM, Keegan BM. Primary intramedullary spinal cord lymphoma. *Neurology* 2011; 77: 784-91.
 8. Yang W, Garzon-Muvdi T, Braileanu M, *et al.* Primary intramedullary spinal cord lymphoma: a population-based study. *Neuro Oncol* 2017; 19: 414-21.
 9. Tripodo C, Iannitto E, Florena AM, *et al.* Gamma-delta T-cell lymphomas. *Nat Rev Clin Oncol* 2009; 6: 707-17.
 10. Mooney KL, Choy W, Woodard J, *et al.* Primary central nervous system gamma delta cytotoxic T-cell lymphoma. *J Clin Neurosci* 2016; 26: 138-40.
 11. Arnulf B, Copie-Bergman C, Delfau-Larue MH, *et al.* Nonhepatosplenic gammadelta T-cell lymphoma: a subset of cytotoxic lymphomas with mucosal or skin localization. *Blood* 1998; 91: 1723-31.
 12. Garcia-Herrera A, Song JY, Chuang SS, *et al.* Nonhepatosplenic gammadelta T-cell lymphomas represent a spectrum of aggressive cytotoxic T-cell lymphomas with a mainly extranodal presentation. *Am J Surg Pathol* 2011; 35: 1214-25.
 13. Choe JY, Bisig B, de Leval L, Jeon YK. Primary gammadelta T cell lymphoma of the lung: report of a case with features suggesting derivation from intraepithelial gammadelta T lymphocytes. *Virchows Arch* 2014; 465: 731-6.
 14. Küçük C, Jiang B, Hu X, *et al.* Activating mutations of STAT5B and STAT3 in lymphomas derived from gammadelta-T or NK cells. *Nat Commun* 2015; 6: 6025.
 15. Roberti A, Dobay MP, Bisig B, *et al.* Type II enteropathy-associated T-cell lymphoma features a unique genomic profile with highly recurrent SETD2 alterations. *Nat Commun* 2016; 7: 12602.

TFE3-Expressing Perivascular Epithelioid Cell Tumor of the Breast

Hyunjin Kim · Jimin Kim
Se Kyung Lee¹ · Eun Yoon Cho
Soo Youn Cho

Department of Pathology and Translational Genomics, ¹Division of Breast Surgery, Department of Surgery, Samsung Medical Center, Sungkyunkwan University School of Medicine, Seoul, Korea

Received: June 29, 2018
Revised: August 17, 2018
Accepted: August 30, 2018

Corresponding Author

Soo Youn Cho, MD, PhD
Department of Pathology and Translational Genomics, Samsung Medical Center, Sungkyunkwan University School of Medicine, 81 Irwon-ro, Gangnam-gu, Seoul 06351, Korea
Tel: +82-2-3410-2817
Fax: +82-2-3410-0025
E-mail: sooyoun.cho@samsung.com

Perivascular epithelioid cell tumor (PEComa) is a very rare mesenchymal tumor with a distinctive morphology and immunophenotype. PEComas usually harbor *TSC2* alterations, although *TFE3* translocations, which occur in MiT family translocation renal cell carcinoma and alveolar soft part sarcoma, are also possible. We recently experienced a case of PEComa with *TFE3* expression arising in the breast. An 18-year-old female patient presented with a right breast mass. Histologically, the tumor consisted of epithelioid cells with alveolar structure and showed a diffuse strong expression of HMB45 and *TFE3*. *TSC2* was preserved. Melan A and smooth muscle actin were negative. To our knowledge, this is the first Korean case of PEComa of the breast that intriguingly presented with *TFE3* expression.

Key Words: Perivascular epithelioid cell neoplasms; *TFE3*; Breast

Perivascular epithelioid cell (PEC) tumor (PEComa) is a mesenchymal tumor characterized by distinctive histological and immunohistochemical features. PEComas are composed of perivascular epithelioid and spindle cells that are immunoreactive to melanocytic and myogenic markers. These tumors are much more common in females than in males and involve gynecologic as well as other abdominopelvic organs.¹ PEComas are mostly benign, although some show aggressive behavior.² Not much is known about PEComas mainly due to their rarity, but several recent studies have revealed that a subset of PEComa has *TFE3* alterations rather than the more common *TSC2/TSC1* abnormalities.³⁻⁵ We recently encountered a case of PEComa arising in the breast that was *TFE3*-immunoreactive and predominantly epithelioid in nature. To our knowledge, only one case of breast PEComa has been reported in the English literature,⁴ and the present case is the first to be reported in Korea. Moreover, PEComas with *TFE3* gene translocation have been noted in other organs,⁶ but this is the first case involving the breast.

CASE REPORT

An 18-year-old female presented with a palpable mass in the upper outer quadrant of the right breast. She had no relevant past medical or family history. Ultrasonographic examination revealed that the mass had increased in size from 1.5×1.3 cm to 3.4×2.7 cm within a seven-month period. The patient visited Samsung Medical Center in Seoul, Korea, following a biopsy in another hospital, where she was diagnosed with PEComa. Wide excision was performed.

The gross examination showed a well-encapsulated, 4×3.2-cm-sized mass, and the cut surface was homogeneously solid and brown. Microscopic findings revealed a thick fibrous capsule wherein epithelioid cells were arranged in a nested architecture surrounded by branching thin-walled vessels (Fig. 1A). The individual epithelioid cells had clear to granular cytoplasm (Fig. 1B). Spindle cells were not observed. The nuclei of the tumor cells were uniform and round, and showed mild atypia. Occasional melanin pigments were noted in the cytoplasm of the tumor cells (Fig. 1C). Necrosis was not identified, and mitoses were counted at

up to 3 per 10 high-power fields (HPFs). The tumor showed diffuse strong positivity to HMB45 (1:80, mouse clone HMB45, Dako Corporation, Carpinteria, CA, USA) (Fig. 2A) and TFE3 (1:20, rabbit clone MRQ-37, Cell Marque, Rocklin, CA, USA) (Fig. 2B). TSC2 (1:200, rabbit clone D93F12, Cell Signaling Technology, Danvers, MA, USA) was also positive. Melan A (1:80, mouse clone A103, Dako Corporation), smooth muscle actin (1:100, mouse clone 1A4, Dako Corporation), S100 protein (1:2,000, rabbit polyclonal, Dako Corporation), and cytokeratin (1:500, mouse clone AE1/AE3, Dako Corporation) were not expressed. Moreover, progesterone receptor (PR; 1:800, mouse clone 16, Novocastra Laboratories Ltd., Newcastle upon Tyne, UK) was positive (Fig. 2C), while estrogen receptor (ER; 1:400, mouse clone 6F11, Novocastra Laboratories Ltd.) was negative.

The histologic and immunohistochemical findings were most consistent with PEComa with TFE3 expression.

Ten months after resection, the patient remained healthy with no evidence of recurrence or other unusual findings. This study was approved by the Institutional Review Board of Samsung Medical Center, and the need for informed consent was waived (2018-06-045).

DISCUSSION

PEComa is a tumor composed of PECs. PECs were first described by Apitz in 1943, who recognized unusual “abnormal myoblasts” in an angiomyolipoma, clear cell sugar tumor (CCST), and lymphangioliomyomatosis.⁷ Later, these cells were revealed to be immunoreactive for HMB45. The World Health Organization defines PEComa as a “mesenchymal tumor composed of histologically and immunohistochemically distinctive perivascular epithelioid cells.”¹

The most common sites of PEComas are the retroperitoneum, abdominopelvic region, uterus, and gastrointestinal tract.¹ The typical histologic findings demonstrate a nested architecture of epithelioid and spindle cells with abundant granular eosinophilic or clear cytoplasm. The epithelioid component of these tumors characteristically expresses melanocytic markers, while the spindle cell component occasionally expresses myogenic markers. PEComas occur more commonly in young and middle-aged patients, and the female to male ratio is greater than 6:1.

In the current report, we present a very rare case of PEComa in the breast. The single known previously reported case was that of an extrapulmonary CCST in the breast of a 16-year-old female,

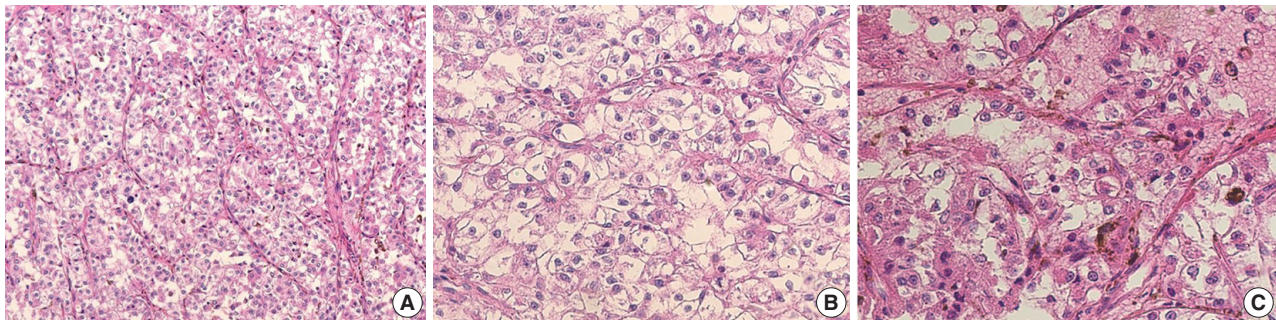


Fig. 1. Microscopic findings of the TFE3-expressing breast perivascular epithelioid cell tumor. (A) Epithelioid cells were arranged in a nested architecture with surrounding branching thin-walled vessels. (B) The individual epithelioid cells show clear to granular cytoplasm. (C) Occasional melanin pigments are noted.

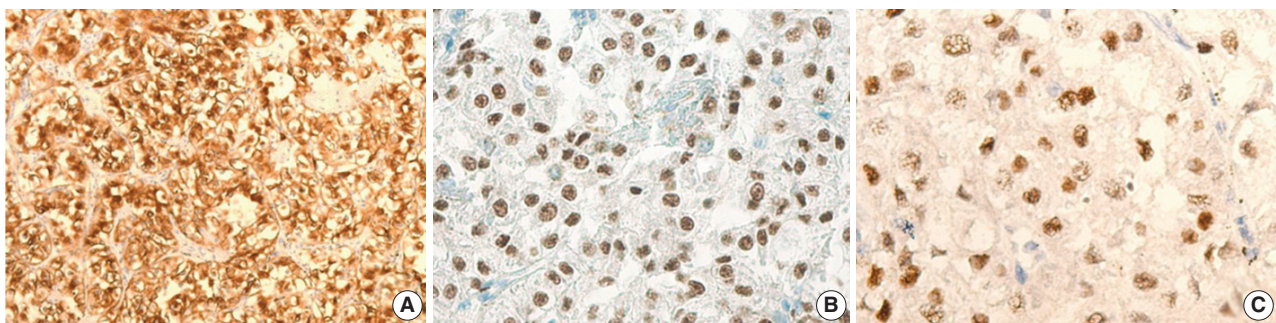


Fig. 2. The immunohistochemical findings of the TFE3-expressing breast perivascular epithelioid cell tumor. The tumor is diffusely positive for human melanoma black 45 (A) and shows nuclear positivity for TFE3 (B) and progesterone receptor (C).

which showed strong immunohistochemical reactivity to HMB45, melan A, and PR.⁴

In our case, the tumor was positive for HMB45 and PR (Fig. 2A, C) and negative for melan A. Interestingly, this case showed diffuse strong expression of TFE3 (Fig. 2B) with preserved TSC2 staining. The strong positivity of TFE3 was notable. Conventional PEComas, both sporadic and syndromic, frequently shows inactivation of *TSC2* or *TSC1* and loss of expression in immunohistochemistry.⁸ Recently, Argani *et al.*⁵ suggested that there may be a “distinct subset of PEComa” that harbors *TFE3* gene fusions. They concluded that such cases tend to present in a “young age group [and] have no association with tuberous sclerosis, with predominant alveolar architecture and epithelioid cytology [and] minimal immunoreactivity for muscle markers,”³ a description that conforms to our case. Schoolmeester *et al.*⁶ also reported the distinct morphology and immunohistochemical features of *TFE3*-rearranged PEComas in the gynecologic tract. *TFE3*-rearranged PEComas do not share the *TSC2/TSC1* genetic abnormalities of conventional PEComas, and retain their protein expressions on immunohistochemistry.⁷ Our case showed strong TFE3 expression and the preservation of TSC2 expression. These two sets of genes (*TFE3*, and *TSC2/TSC1*) have been suggested to be mutually exclusive and crucial in the pathogenesis of PEComas.⁵

The *TFE3* gene is located on the short arm of the X chromosome and normally encodes a transcription factor that binds one of the E-box sequences (present in the immunoglobulin enhancer) in the promoter sequences.⁹ Downstream of transforming growth factor beta signaling, *TFE3* is promoted by encoded transcription factors. Xp11-associated renal cell carcinoma (now reclassified as the MiT family translocation renal cell carcinoma) and alveolar soft part sarcoma (ASPS) are associated with this translocation. *TFE3* translocations may play regulatory roles in the epithelioid morphology of tumors arising from different origins.⁶

PR immunoreactivity in PEComa has also been described in a previous study.² It has been suggested that female hormones play a role in the development of these tumors, considering their female predominance and the frequent involvement of gynecological organs. PEComa of the uterus described by Armah and Parwani² showed strong positivity to PR and stronger positivity to ER. However, our case demonstrated PR positivity coupled with ER negativity. The significance of this finding has yet to be determined.

The malignancy criteria of PEComas have not been established because only extremely rare cases have metastasized or recurred. In one study of 26 PEComas, Folpe *et al.*¹⁰ suggested

that tumor size greater than 8 cm, more than one mitosis per 50 HPFs, and presence of necrosis were strongly associated with malignant behavior. In another, Schoolmeester *et al.*¹¹ suggested malignancy criteria intended only for gynecologic organs including tumor size greater than 5 cm, high-grade nuclear features, necrosis, vascular invasion, and a mitotic rate greater than 1/50 HPFs.

Although PEComas show a distinct morphology, other entities in the breast presenting an alveolar architecture of epithelioid cells should be considered in determining the identity. The differential diagnosis should include metastatic renal clear cell carcinoma, clear cell glycogen rich carcinoma, and ASPS as per histologic findings. Pancytokeratin negativity excludes the two carcinomas. While epithelioid nested architecture and TFE3 positivity are common histologic features of ASPS, HMB45 positivity excludes this diagnosis.

When pathologists encounter an unusual epithelioid tumor of the breast, PEComa should be considered in the differential diagnosis. In addition to HMB45, other immunohistochemical data such as those of TFE3 and TSC2/TSC1 may be informative.

The accumulation of more data for PEComa and rigorous studies on relevant topics including genetic background may be helpful for determining the origin, prognosis, and treatment options for the rare cases of PEComa.

ORCID

Hyunjin Kim: <https://orcid.org/0000-0001-8336-881X>

Jimin Kim: <https://orcid.org/0000-0002-3846-8093>

Se Kyung Lee: <https://orcid.org/0000-0003-1630-1783>

Eun Yoon Cho: <https://orcid.org/0000-0001-5849-3600>

Soo Youn Cho: <https://orcid.org/0000-0001-9714-7575>

Conflicts of Interest

The authors declare that they have no potential conflicts of interest.

REFERENCES

1. Fletcher CD, Unni KK, Epstein J, Mertens F. World Health Organization classification of tumours: pathology and genetics of tumours of soft tissue and bone. Lyon: IARC Press, 2002; 221-2.
2. Armah HB, Parwani AV. Malignant perivascular epithelioid cell tumor (PEComa) of the uterus with late renal and pulmonary metastases: a case report with review of the literature. *Diagn Pathol* 2007; 2: 45.

3. Argani P, Aulmann S, Illei PB, *et al.* A distinctive subset of PEComas harbors *TFE3* gene fusions. *Am J Surg Pathol* 2010; 34: 1395-406.
4. Govender D, Sabaratnam RM, Essa AS. Clear cell 'sugar' tumor of the breast: another extrapulmonary site and review of the literature. *Am J Surg Pathol* 2002; 26: 670-5.
5. Malinowska I, Kwiatkowski DJ, Weiss S, Martignoni G, Netto G, Argani P. Perivascular epithelioid cell tumors (PEComas) harboring *TFE3* gene rearrangements lack the *TSC2* alterations characteristic of conventional PEComas: further evidence for a biological distinction. *Am J Surg Pathol* 2012; 36: 783-4.
6. Schoolmeester JK, Dao LN, Sukov WR, *et al.* *TFE3* translocation-associated perivascular epithelioid cell neoplasm (PEComa) of the gynecologic tract: morphology, immunophenotype, differential diagnosis. *Am J Surg Pathol* 2015; 39: 394-404.
7. Martignoni G, Pea M, Reghellin D, Zamboni G, Bonetti F. PEComas: the past, the present and the future. *Virchows Arch* 2008; 452: 119-32.
8. Agaram NP, Sung YS, Zhang L, *et al.* Dichotomy of genetic abnormalities in PEComas with therapeutic implications. *Am J Surg Pathol* 2015; 39: 813-25.
9. NCBI. *TFE3* transcription factor binding to IGHM enhancer 3 [Homo sapiens (human)] [Internet]. Bethesda: National Center for Biotechnology Information, 2018 [cited 2018 Aug 30]. Available from: <https://www.ncbi.nlm.nih.gov/gene?Db=gene&Cmd=DetailsSearch&Term=7030>.
10. Folpe AL, Mentzel T, Lehr HA, Fisher C, Balzer BL, Weiss SW. Perivascular epithelioid cell neoplasms of soft tissue and gynecologic origin: a clinicopathologic study of 26 cases and review of the literature. *Am J Surg Pathol* 2005; 29: 1558-75.
11. Schoolmeester JK, Howitt BE, Hirsch MS, Dal Cin P, Quade BJ, Nucci MR. Perivascular epithelioid cell neoplasm (PEComa) of the gynecologic tract: clinicopathologic and immunohistochemical characterization of 16 cases. *Am J Surg Pathol* 2014; 38: 176-88.

Rare Manifestations of Churg-Strauss Syndrome with Mediastinal and Hilar Lymphadenopathies: Report of an Autopsy Case

Woo Cheal Cho · Bharat Ramlal · Mary Fiel-Gan · Xianyuan Song

Department of Pathology and Laboratory Medicine, Hartford Hospital, Hartford, CT, USA

Churg-Strauss syndrome (CSS) is a rare systemic disorder that is classically characterized by asthma, tissue and blood eosinophilia, and necrotizing vasculitis along with a granulomatous response to eosinophilic necrosis in its full-blown form. It has a predilection for small- and medium-sized vessels of the lungs, but can virtually affect any organ system, including the heart, skin, gastrointestinal tract, and nervous system. Involvement of the lymph node in CSS, however, is still rare with only a few cases reported in the English literature.¹⁻⁶ Furthermore, the classic histologic features of CSS, particularly necrotizing vasculitis, are infrequently captured in the modern biopsy or autopsy specimens due to the widespread use of steroids.⁷ Here, we report the autopsy findings of a 69-year-old man with CSS involving mediastinal and hilar lymph nodes and discuss the histologic features of partially treated CSS.

Formal written informed consent was not required with a waiver by the appropriate institutional review board and/or national research ethics committee (FWA00021932).

CASE REPORT

A 69-year-old man presented to the Emergency Department after a witnessed cardiac arrest and subsequently died shortly thereafter. On autopsy, ruptured abdominal aortic aneurysm (7.0 cm in greatest diameter) with a 2.0-cm linear tear, moder-

ate-severe atherosclerosis of abdominal aorta, cardiomegaly (500 g) with biventricular hypertrophy, congestive hepatomegaly (2,050 g), and multiple bilateral pulmonary nodules (measuring up to 1.5 cm) with significant mediastinal and hilar lymphadenopathies (Fig. 1A) were grossly identified. Histologically, the lung nodules showed multifocal necrotizing granulomas with surrounding tissues infiltrated by lymphocytes and rare scattered eosinophils (Fig. 1B). Extravascular eosinophilic infiltration with associated granulomatous inflammation (Fig. 1C) but without overt necrotizing vasculitis, as well as foci of mild-moderate peribronchial eosinophilic infiltration, was also noted. A few small-sized arteries showed prominent necrotizing granulomatous inflammation focally involving the vessel wall (Fig. 2A, B). Occasionally, rare eosinophils with partially degenerated nuclei were found within the center of the necrosis (Fig. 2C). Most vessels involved by granulomatous inflammation did not reveal an overt necrotizing vasculitis, and viable eosinophils with intact nuclei were more readily identified within these granulomas (Fig. 2D, E). The mediastinal and hilar lymph nodes showed prominent necrotizing granulomas diffusely involving the nodal parenchyma; the center of the necrotizing granulomas displayed numerous necrotic or degenerated cells with acidophilic granules (Fig. 3A-C). In contrast, viable eosinophils with intact nuclei were more readily identified at the periphery or outside the necrotic zone (Fig. 3D). Special stains for acid-fast bacilli and fungal microorganisms were negative in sections of the lung nodules as well as the lymph nodes. The abdominal aorta, including the area of rupture, was extensively sectioned but revealed no evidence of vasculitis, granulomatous disease, or tissue eosinophilia. Additional clinical information obtained following the autopsy revealed that the patient had chronic asthma, sinus abnormalities, peripheral hyper eosinophilia, and perinuclear

Corresponding Author

Woo Cheal Cho, MD
Department of Pathology and Laboratory Medicine, Hartford Hospital, 80 Seymour Street, Hartford, CT 06102-5037, USA
Tel: +1-860-972-2488, Fax: +1-860-545-2204
E-mail: woocheal.cho@hhchealth.org

Received: September 6, 2017 Revised: December 13, 2017

Accepted: December 13, 2017

anti-neutrophil cytoplasmic antibody on serology, confirming the diagnosis of CSS. Further review of the patient's history also revealed use of corticosteroids, which had recently been tapered and were switched to rituximab.

DISCUSSION

CSS is a rare systemic disorder with a reported annual incidence of 1–2 cases per million persons in the general population.⁸ It was first described by Churg and Strauss⁹ in 1951 on 13 patients as “allergic granulomatosis, allergic angiitis, and periarteritis nodosa.” The original cases described by Churg and Strauss⁹ shared a spectrum of many similar clinicopathologic features such as asthma, blood and tissue eosinophilia, necrotizing vascu-

litic, and granulomatous response to eosinophilic necrosis. Recent studies, however, have suggested that this definition may indeed be too narrow, leading to the exclusion of certain cases that may not have such “classic” findings.⁷ The original 13 cases predated the use of exogenous steroids, thereby representing this entity in its untreated or full-blown form. In contrast, currently, steroids are widely used not only for asthmatics but also for the patients with suspected CSS. The widespread use of steroids in the modern era often leads to a confusing situation where the definitive or “classic” features of CSS, particularly eosinophilic necrotizing vasculitis, are absent. In addition, CSS has an early, “pre-vasculitic” or “prodromal” phase characterized by tissue infiltration of eosinophils without overt vasculitis, as well as postvasculitic phase (if successfully treated) in which dense organizing thrombi

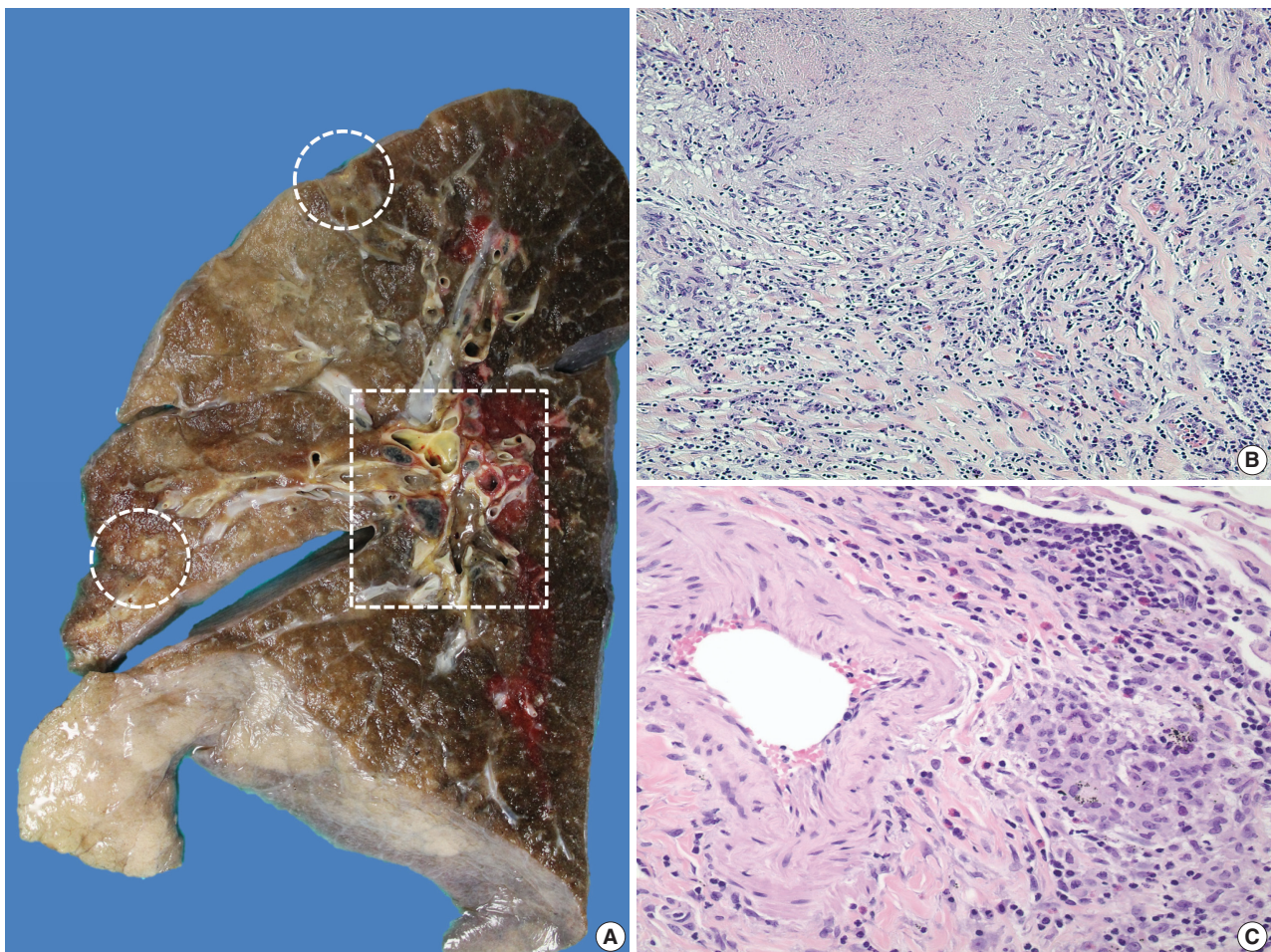


Fig. 1. Gross and histologic findings of pulmonary nodules. (A) The right lung (570 g) grossly displays multiple peripherally located palpable nodules (dashed circles), measuring up to 1.5 cm in greatest dimension. The nodules are tan, firm, and relatively well-circumscribed with an irregular border. Also noted are significant subcarinal (not shown) and hilar (dashed rectangle) lymphadenopathies with a mild-moderate anthracotic pigment deposition. (B) Histologically, the lung nodules display prominent necrotizing granulomatous inflammation with surrounding tissues infiltrated by lymphocytes and rare scattered eosinophils. (C) Extravascular eosinophilic infiltration with associated granulomatous inflammation without forming an overt necrotizing vasculitis is also noted.

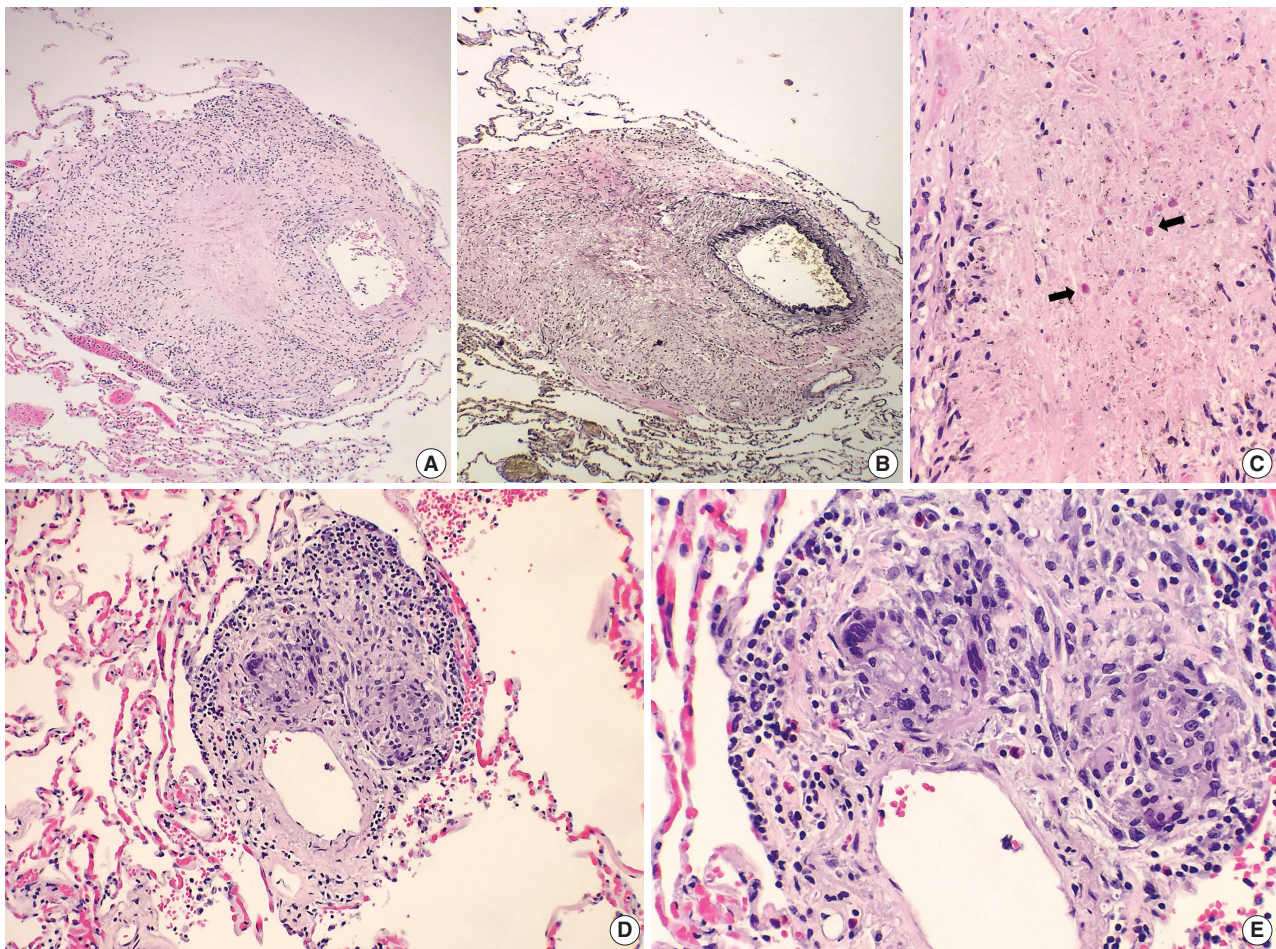


Fig. 2. Histologic spectrum of perivascular eosinophilic granulomatous inflammation. (A–C) A few small-sized arteries reveal a prominent necrotizing granulomatous inflammation focally involving the vessel wall (B, elastin stain). Occasionally, the center of the necrosis shows rare eosinophils with partially degenerated nuclei (arrows). (D, E) The majority of vessels involved by granulomatous inflammation do not reveal an overt necrotizing vasculitis. Viable eosinophils are more readily identified within these granulomas.

are seen within the vascular lumen in the absence of active vasculitis or eosinophils.⁷ Thus, the absence of eosinophilic necrotizing vasculitis should not preclude the diagnosis.

Currently, the diagnostic criteria proposed by the American College of Rheumatology (ACR)¹⁰ is widely used with the broadest definition of CSS: (1) asthma, (2) paranasal sinus abnormalities, (3) eosinophilia greater than 10% on differential white blood cell count, (4) neuropathy (mono or poly), (5) pulmonary infiltrates, and (6) biopsy containing a blood vessel with extravascular eosinophils. The ACR criteria do not require pathologic evidence of vasculitis, and the presence of four or more of these six criteria have yielded a sensitivity of 85% and a specificity of 99.7%.¹⁰ In this present case, our patient fulfilled at least five out of six diagnostic criteria, and we believe our case represents a partially treated CSS.

In conclusion, our case illustrates rare manifestations of CSS

and adds to the growing pool of case reports of CSS with lymphadenopathy; a finding which can raise the differential diagnosis that includes lymphoma and infection. Histologic descriptions of CSS involving lymph nodes is in the literature showing necrotizing granulomas and eosinophilic necrosis are scarce. Furthermore, an awareness of the histologic features of treated CSS is important, as strict adherence to the original diagnostic criteria may erroneously lead to an under- or misdiagnosis.

ORCID

Woo Cheal Cho: <https://orcid.org/0000-0001-5867-1403>

Conflicts of Interest

The authors declare that they have no potential conflicts of interest.

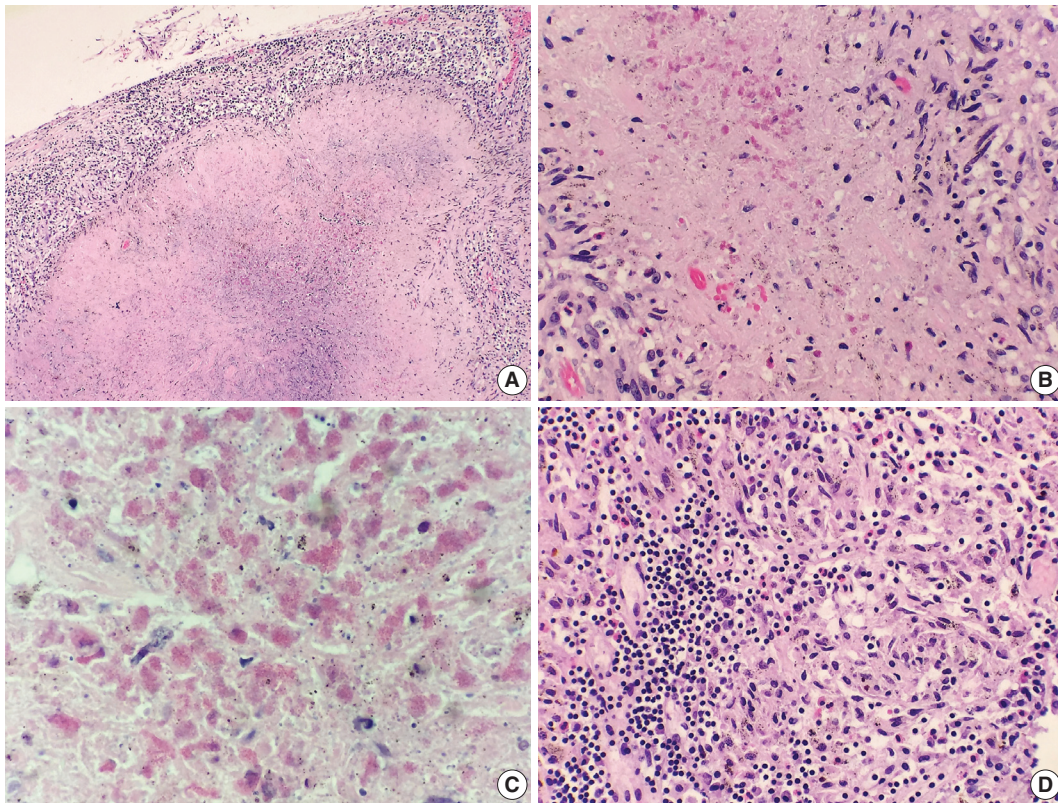


Fig. 3. Histologic findings of lymph nodes. (A–D) The mediastinal and hilar lymph nodes display prominent necrotizing granulomas. Within the center of the necrosis are numerous necrotic or degenerating eosinophils without intact nuclei but predominantly with acidophilic granules (A–C). In contrast, the periphery of or outside the necrotic zone show more readily identifiable eosinophilic infiltrates (D).

REFERENCES

- Casey M, Radel E, Ratch H. Lymph node manifestations of limited Churg-Strauss syndrome. *J Pediatr Hematol Oncol* 2000; 22: 468-71.
- Choi JY, Kim JE, Choi IY, *et al.* Churg-Strauss syndrome that presented with mediastinal lymphadenopathy and calculous cholecystitis. *Korean J Intern Med* 2016; 31: 179-83.
- Choi YH, Im JG, Han BK, Kim JH, Lee KY, Myoung NH. Thoracic manifestation of Churg-Strauss syndrome: radiologic and clinical findings. *Chest* 2000; 117: 117-24.
- Churg A, Brallas M, Cronin SR, Churg J. Formes frustes of Churg-Strauss syndrome. *Chest* 1995; 108: 320-3.
- Cualing H, Schroder L, Perme C. Allergic granulomatosis secondary to a limited form of Churg-Strauss syndrome. *Arch Pathol Lab Med* 2001; 125: 954-7.
- Lesens O, Hansmann Y, Nerson J, *et al.* Severe Churg-Strauss syndrome with mediastinal lymphadenopathy treated with interferon therapy. *Eur J Intern Med* 2002; 13: 458.
- Churg A. Recent advances in the diagnosis of Churg-Strauss syndrome. *Mod Pathol* 2001; 14: 1284-93.
- Watts RA, Carruthers DM, Scott DG. Epidemiology of systemic vasculitis: changing incidence or definition? *Semin Arthritis Rheum* 1995; 25: 28-34.
- Churg J, Strauss L. Allergic granulomatosis, allergic angiitis, and periarteritis nodosa. *Am J Pathol* 1951; 27: 277-301.
- Masi AT, Hunder GG, Lie JT, *et al.* The American College of Rheumatology 1990 criteria for the classification of Churg-Strauss syndrome (allergic granulomatosis and angiitis). *Arthritis Rheum* 1990; 33: 1094-100.

Cytopathologic Features of Secretory Carcinoma of Salivary Gland: Report of Two Cases

Young Ah Kim · Jae Won Joung
Sun-Jae Lee · Hoon-Kyu Oh
Chang Ho Cho · Woo Jung Sung

Department of Pathology, Catholic University of
Daegu School of Medicine, Daegu, Korea

Received: October 31, 2018
Revised: November 8, 2018
Accepted: November 9, 2018

Corresponding Author

Woo Jung Sung, MD, PhD
Department of Pathology, Catholic University of
Daegu School of Medicine, 33 Duryugongwon-ro
17-gil, Nam-gu, Daegu 42472, Korea
Tel: +82-53-650-4159
Fax: +82-53-650-3456
E-mail: wjsung@cu.ac.kr

Secretory carcinoma of the salivary gland (SC) is a newly introduced rare salivary gland tumor that shares histological, immunohistochemical, and genetic characteristics with secretory carcinoma of the breast. Here, we report the cytologic features of two cases of SC confirmed by surgical resection. In these two cases, SC was incidentally detected in a 64-year-old female and a 56-year-old male. Fine needle aspiration cytology revealed nests of tumor cells with a papillary or glandular structure floating in mucinous secretions. The tumor cells demonstrated uniform, round, smooth nuclear contours and distinct nucleoli. Multiple characteristic cytoplasmic vacuoles were revealed. Singly scattered tumor cells frequently showed variable sized cytoplasmic vacuoles. The cytopathologic diagnosis of SC should be considered when characteristic cytological findings are revealed. Further immunohistochemistry and gene analyses are helpful to diagnose SC.

Key Words: Secretory carcinoma; Mammary analogue secretory carcinoma; Salivary gland; Cytology

Secretory carcinoma of salivary gland (SC) is a distinctive low-grade tumor recently described in the 2017 WHO classification of head and neck tumors. SC shares histological, immunohistochemical, and genetic features with secretory carcinoma of the breast.¹ Histologically, secretory carcinomas of both the salivary gland and breast are composed of uniform cells with characteristic eosinophilic granular or vacuolated cytoplasm arranged in microcystic, solid, tubular, and follicular growth patterns. Akin to that in a secretory breast cancer, SC expresses S100 protein, mammaglobin, and vimentin, and has a t(12;15) (p13;q25) translocation, which leads to the formation of the ETV6-NTRK3 fusion product.²

SC is usually a painless, slow-growing mass that ranges in size from 1 to 4 cm.³ SC usually involves the parotid gland (about 70%),⁴ followed by the submandibular gland (about 7%). It rarely affects other sites, including the minor salivary glands of the oral cavity.⁵ The mean age of SC patients is 46.5 years (age range, 10 to 86 years).⁶ SC shows indolent behavior, but local recurrence was reported in 25% of cases, lymph node metastasis was reported in 20% of cases, and metastasis was reported in 5% of cases.^{6,7} The rate of lymph node metastasis was slightly

greater than that of ACC.^{8,9} SC with high-grade transformation has been described in the literature.¹⁰⁻¹²

Fine needle aspiration (FNA) cytology is a widely used efficient first line diagnostic tool for salivary gland lesions. The reports of cytologic findings of SC are limited and describe a wide range of cytomorphologic characteristics. In this study, we report the cytopathologic findings of two cases of SC confirmed in surgical specimens by histological and genetic analysis.

This study was approved by the Institutional Review Board of Catholic University of Daegu Medical Center (IRB No. CR-18-155), and informed consent was waived.

CASE REPORT

Case 1

A 64-year-old female without any medical history incidentally found an asymptomatic mass on her left mandible angle. On physical examination, an approximately 0.5×0.5-cm-sized movable firm mass was detected. Ultrasonography revealed an approximately 1.0×0.7-cm-sized hypoechoic mass at the anterior portion of the parotid gland.

FNA cytology revealed a cellular aspirate composed of papillary nests or follicular architecture with individually dispersed cells (Fig. 1A). The background showed abundant mucinous material with a small population of scattered lymphocytes (Fig. 1B). The tumor cells showed large, relatively uniform round nuclei with smooth nuclear contours, fine chromatin, and distinct eosinophilic nucleoli (Fig. 1C). The cytoplasm of individual tumor cells was granular, pale, or vacuolated. Cytoplasmic vacuoles showed variable sizes and were usually small, although some cells showed macrovacuoles reminiscent of signet ring cells (Fig. 1D, E). Individual cells with binucleated and eccentric nuclei were easily identified (Fig. 1F). FNA cytology was diagnosed as acinic cell carcinoma (ACC).

After FNA, left parotidectomy was performed. On gross exami-

nation of the surgical specimen, a well-demarcated tan to yellowish mass was identified. Microscopically, a well-encapsulated mass with a focally infiltrative margin was noted. The tumor was composed of microcystic, follicular, and focal papillary architecture with homogeneous eosinophilic colloid-like luminal secretions (Fig. 1G). The tumor cells had granular or vacuolated cytoplasm, and vacuolated tumor cells were frequently identified at the papillary growing area. There was no necrosis, mitotic figures, lymphovascular invasion, or neural invasion. Immunohistochemical stains showed diffuse strong positive reactivity for S100 protein (Fig. 1H), mammaglobin, gross cystic disease fluid protein 15 (GCDFP-15), cytokeratin 7 (CK7), epithelial membrane antigen (EMA), and focal weak positive reactivity for DOG1. No reactivity was noted for smooth muscle actin (SMA) and

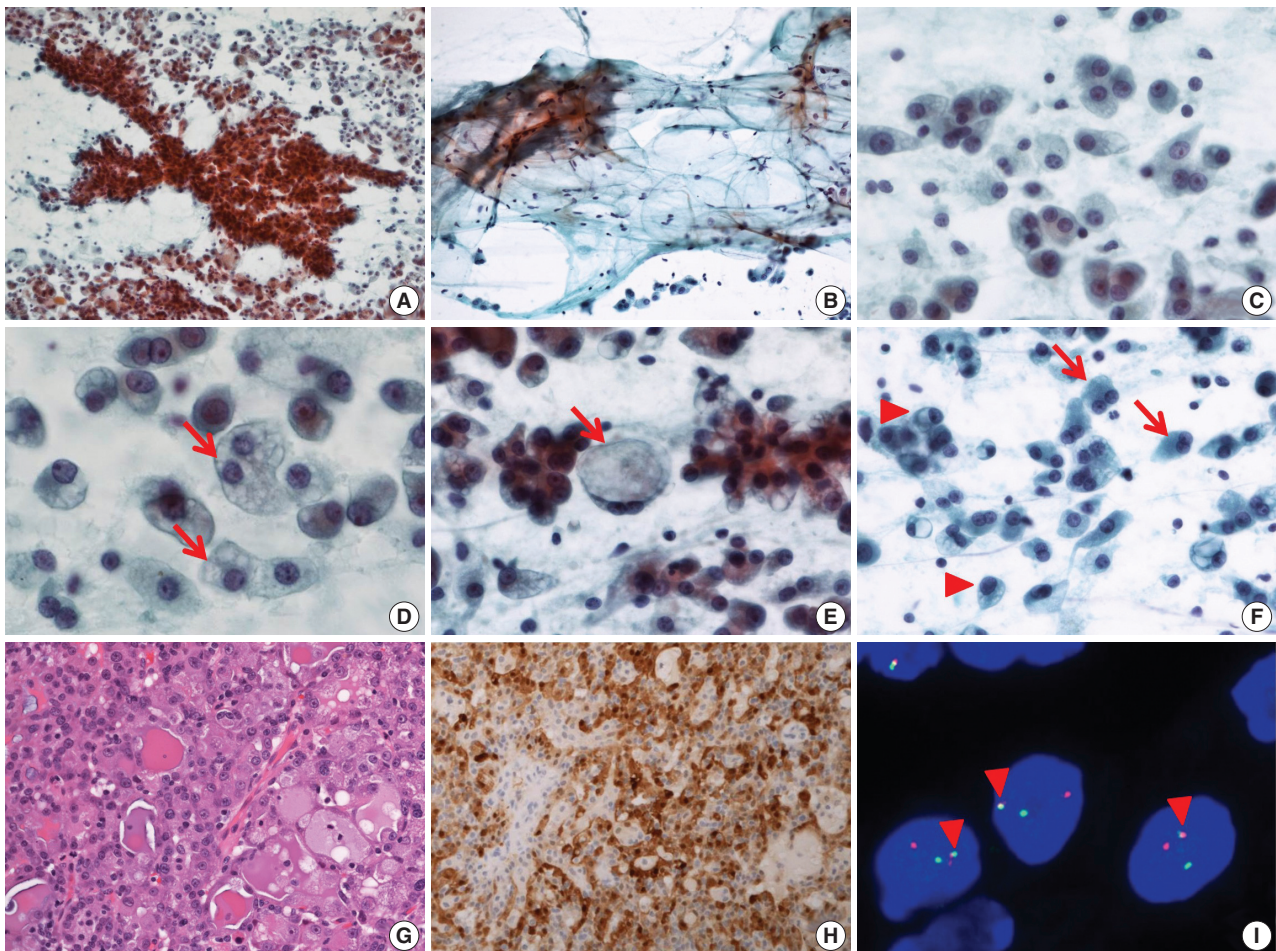


Fig. 1. Cytopathologic features of case 1. (A) The specimen has high cellularity and nest with papillary structure. (B) Mucinous background is easily recognized with scattered lymphocytes and individual tumor cells. (C) Tumor cells have uniform, round nuclei and distinct nucleoli. (D) Various sized cytoplasmic vacuoles (arrows) are noted. (E) Some macrovacuoles (arrow), similar to signet ring cells, may be seen. (F) Some tumor cells show binucleation (arrows) or eccentric nuclei (arrowheads). (G) The tumors consist of microcystic or follicular structures with eosinophilic secretions. (H) Strong diffuse immunoreactivity to S100 protein. (I) ETV6 fluorescence *in situ* hybridization showing one fused (arrowheads) and one split (red and green) signal indicative of ETV6 translocation.

p63. *ETV6* gene translocation was confirmed by fluorescence *in situ* hybridization (FISH) using a dual-color break-apart *ETV6* probe (Abbott Molecular, Des Plaines, IL, USA) (Fig. 1I). The patient showed no evidence of recurrence or metastasis at 1-year-follow up.

Case 2

A 56-year-old male without any past history found an asymptomatic mass on the left parotid area. On physical examination, an approximately 2.5 × 2.0-cm-sized hard movable mass was detected. Ultrasonography revealed a 2.6 × 1.8-cm-sized well demarcated isoechoic mass in the left parotid gland.

On FNA cytology, cellularity was relatively low (Fig. 2A). The aspirate material consisted of cohesive epithelial cells and loose trabecular nests with hemosiderin-laden macrophages

(Fig. 2B). Tumor cell nuclei had minimal anisonucleosis and were centrally located (Fig. 2C). The tumor cells showed a moderate amount of eosinophilic fine granular or clear cytoplasm (Fig. 2D). Vacuolated cells were relatively rare (Fig. 2E, F). The aspirate was diagnosed as benign because it had low cellularity and the vacuolated cells were recognized as macrophages.

The patient underwent a partial left parotidectomy. On gross examination, a well-circumscribed cystic mass with an intracystic solid portion was identified, measuring 2.5 × 1.8 cm in dimension. Microscopically, the tumor was lobulated by fibrous septa and exhibited cyst formation. The centrally located solid area was composed of microcystic and follicular architecture (Fig. 2G). The tumor cells showed eosinophilic granular and occasionally vacuolated cytoplasm. On immunohistochemistry, the tumor cells were reactive for S100 protein, mammaglobin (Fig.

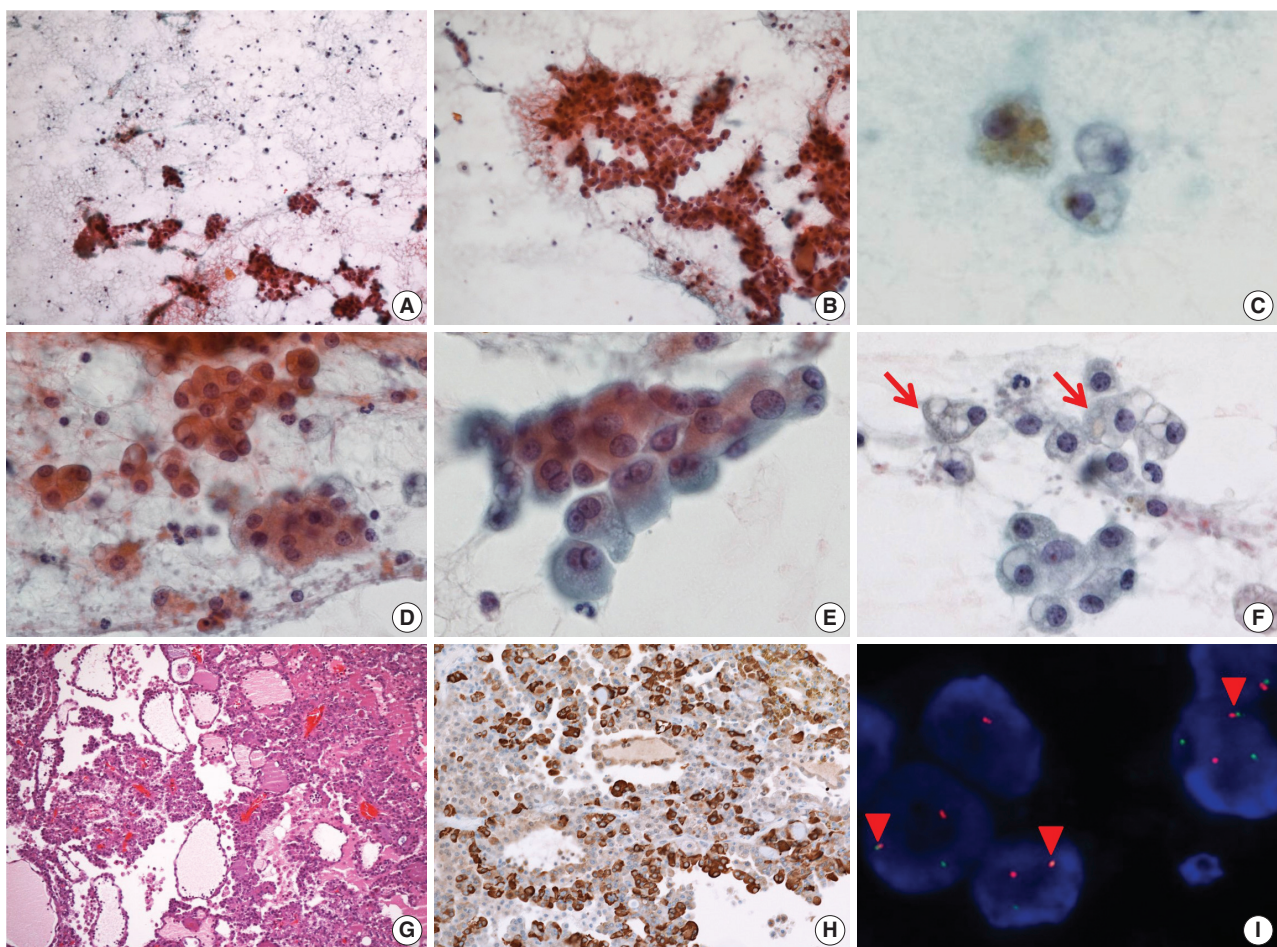


Fig. 2. Cytopathologic features of case 2. (A) The specimen has low cellularity compared with case 1. (B) Loose trabecular nests of tumor cells are noted. (C) Hemosiderin laden macrophages are found. (D) Tumor cells have uniform, centrally located nuclei. (E) Tumor cells show eosinophilic and fine granular cytoplasm. (F) Sometimes, vacuolated cells (arrows) are encountered. (G) Tumor cells show microcystic, follicular architecture with eosinophilic secretions. (H) Strong immunoreactivity to mammaglobin is noted. (I) *ETV6* fluorescence *in situ* hybridization showing one fused (arrowheads) and one split (red and green) signal indicative of *ETV6* translocation.

2H), CK7, and EMA, and no reactivity was noted for GCD-FP-15, SMA, and p63. As in case 1, weak and focal positive immunoreaction for DOG1 stain was identified. Fusion of *ETV6* and *NTRK* gene was revealed by FISH (Fig. 2I). At first, the mass was diagnosed as papillary cystic variant ACC. In the retrospective review of previous cases of SC, the present case was confirmed as SC. No local recurrence or distant metastasis has been noted in the patient for the past 9 years.

DISCUSSION

The cytologic findings on FNA of SC have been reported as cellular smears composed of cohesive cell groups of papillary, solid, or discohesive architecture. Tumor cells have round nuclei with vacuolated or granular cytoplasm. The most easily recognized cytologic finding of SC is cells with cytoplasmic vacuoles. However, vacuolated tumor cells can be found in ACC or in mucoepidermoid carcinoma (MEC) as well as in SC. The tumor cells of classic ACC have a variable amount of cytoplasmic zymogen granules, which are periodic acid-Schiff–positive and diastase resistant. Zymogen granule poor ACC shows considerable morphologic overlap with SC.² However, ACC demonstrates cytologic and structural diversity, whereas SC is structurally homogeneous and uniformly composed of microcystic and glandular spaces with luminal secretory material.¹ The tumor cells of SC exhibit small nuclei and smooth nuclear membrane contours on FNA compared to cells of ACC. SC frequently shows vacuolated cytoplasm and a singly scattered pattern. MEC is also a major differential diagnosis. FNA of MEC seldom shows isolated cells, whereas SC usually presents with abundant isolated single cells.¹²

We initially reported the FNA of case 2 as a benign lesion because vacuolated tumor cells were recognized as macrophages with cystic change. However, in a retrospective review, the nuclei of the vacuolated tumor cells were relatively uniform in size with smooth nuclear contours. The tumor cells formed small clusters, whereas macrophages tend to be singly dispersed. FNA specimens of low-grade tumors with cystic change usually have low cellularity, and macrophages are frequently identified. Therefore, it is difficult to distinguish vacuolated tumor cells from macrophages.

In summary, the cytologic characteristics of SC included papillary or other cellular nests and individual tumor cells with abundant and granular to vacuolated cytoplasm. The tumor cells showed uniform and round nuclei with distinct nucleoli. The background mucinous material is helpful for diagnosis. However, the cytologic features overlap with those of other salivary

gland neoplasms, such as ACC and MEC, and benign cystic lesions. A definite diagnosis of SC by FNA is difficult, but cytopathologists should suggest the possibility of SC when presented with characteristic cytologic findings on FNA. Immunohistochemistry and verification of *ETV6-NTRK3* fusion gene are useful to differentiate SC from other salivary gland tumors.

ORCID

Young Ah Kim: <https://orcid.org/0000-0001-7850-5509>

Jae Won Joung: <https://orcid.org/0000-0001-9466-3240>

Sun-Jae Lee: <https://orcid.org/0000-0002-8552-6049>

Hoon-Kyu Oh: <https://orcid.org/0000-0001-8793-1948>

Chang Ho Cho: <https://orcid.org/0000-0003-2708-6011>

Woo Jung Sung: <https://orcid.org/0000-0001-9510-3763>

Conflicts of Interest

The authors declare that they have no potential conflicts of interest.

REFERENCES

- Skalova A, Vanecek T, Sima R, *et al*. Mammary analogue secretory carcinoma of salivary glands, containing the *ETV6-NTRK3* fusion gene: a hitherto undescribed salivary gland tumor entity. *Am J Surg Pathol* 2010; 34: 599-608.
- Skalova A. Mammary analogue secretory carcinoma of salivary gland origin: an update and expanded morphologic and immunohistochemical spectrum of recently described entity. *Head Neck Pathol* 2013; 7 Suppl 1: S30-6.
- Parekh V, Stevens TM. Mammary analogue secretory carcinoma. *Arch Pathol Lab Med* 2016; 140: 997-1001.
- Boon E, Valstar MH, van der Graaf WT, *et al*. Clinicopathological characteristics and outcome of 31 patients with *ETV6-NTRK3* fusion gene confirmed (mammary analogue) secretory carcinoma of salivary glands. *Oral Oncol* 2018; 82: 29-33.
- Sethi R, Kozin E, Remenschneider A, *et al*. Mammary analogue secretory carcinoma: update on a new diagnosis of salivary gland malignancy. *Laryngoscope* 2014; 124: 188-95.
- El-Naggar AK, Chan JK, Grandis JR, Takata T, Slootweg PJ. WHO classification of head and neck tumours. Lyon: International Agency for Research on Cancer, 2017.
- Bishop JA, Yonescu R, Batista DA, Westra WH, Ali SZ. Cytopathologic features of mammary analogue secretory carcinoma. *Cancer Cytopathol* 2013; 121: 228-33.
- Seethala RR, Stenman G. Update from the 4th edition of the World

- Health Organization classification of head and neck tumours: tumors of the salivary gland. *Head Neck Pathol* 2017; 11: 55-67.
9. Chiosea SI, Griffith C, Assaad A, Seethala RR. Clinicopathological characterization of mammary analogue secretory carcinoma of salivary glands. *Histopathology* 2012; 61: 387-94.
 10. Skálová A, Vanecek T, Majewska H, *et al.* Mammary analogue secretory carcinoma of salivary glands with high-grade transformation: report of 3 cases with the *ETV6-NTRK3* gene fusion and analysis of *TP53*, beta-catenin, *EGFR*, and *CCND1* genes. *Am J Surg Pathol* 2014; 38: 23-33.
 11. Luo W, Lindley SW, Lindley PH, Krempf GA, Seethala RR, Fung KM. Mammary analog secretory carcinoma of salivary gland with high-grade histology arising in hard palate, report of a case and review of literature. *Int J Clin Exp Pathol* 2014; 7: 9008-22.
 12. Jung MJ, Kim SY, Nam SY, *et al.* Aspiration cytology of mammary analogue secretory carcinoma of the salivary gland. *Diagn Cytopathol* 2015; 43: 287-93.

